Developing Techniques to Assess the Habitability Potential of Ancient Mars and Beyond

by

Amanda V. Steckel

B.S., Cornell University, 2014

M.E., Cornell University, 2015

A thesis submitted to the

Faculty of the Graduate School of the

University of Colorado in partial fulfillment

of the requirements for the degree of

Doctor of Philosophy

Department of Geological Sciences

2024

Committee Members:

Professor Kristy Tiampo, Chair

Professor Brian Hynek

Dr. Amanda Hendrix

Professor Steve Schmidt

Professor Carolyn Crow

Steckel, Amanda V. (Ph.D., Geological Sciences)

Developing Techniques to Assess the Habitability Potential of Ancient Mars and Beyond

Thesis directed by Professor Brian Hynek

Abstract

The search for life beyond Earth is one of humanity's most profound scientific endeavors. This thesis explores innovative approaches to planetary surface exploration with three interconnected projects motivated by a desire to understand the potential habitability of other worlds. The first project develops landscape evolution models to investigate the presence of water on ancient Mars. The second project tests innovative exploration strategies to optimize geologic field mapping in a planetary analog environment. The third project improves on remote sensing techniques for mineral identification through challenging spectral ranges in Earth's atmosphere which are typically blocked by water vapor. Throughout these studies, we demonstrate the value of integrating orbital and in situ data despite the challenges posed from interpreting geologic features at different spatial resolutions. This research contributes to the development of a new paradigm in planetary exploration where advanced remote sensing, autonomous systems, and targeted in situ investigations work in concert to unravel the complex geologic histories of planetary surfaces in our solar system.

Dedication

To Kyle, Zen, Io, and Kuiper, who made this dream a reality.

Acknowledgements

Thank you to my committee members and advisers at CU Boulder, and to the NSF graduate research fellowship program and Benson fellowships.

I'd especially like to thank Amanda Hendrix, who replied to a cold email and ended up becoming an amazing co-adviser and mentor.

Thank you to my parents, for instilling a passion for engineering and science, and the drive to follow both. Also thank you to Kyle Thompson for encouraging me to quit my really fun engineering job building satellites. Without your boundless enthusiasm for science and endless support, I would never have taken this leap.

Contents

Chapter

Tables

Table

Figures

Figure

Chapter 1

Introduction: How to Study Planetary Surfaces

This chapter consists of several subsections which will introduce the topics covered in this thesis. Three projects are presented in this thesis which used remote sensing data to interpret the geologic context of a planetary surface, but address unique scientific questions. Chapter 2 uses remote sensing datasets to assess if the origin of valley networks on ancient Mars is from glacial meltwater or precipitation and surface runoff. Chapter 3 investigates if spectral information of surface rocks that is typically obscured by Earth's atmosphere can be measured with a drone mountable remote spectrometer and used for mineral identification. Chapter 4 deploys new remote sensing techniques in a planetary analog mission to interpret the local stratigraphy and see if these tools improve on existing geologic mapping strategies for planetary surfaces.

1.1 A Short History of Mapping Planetary Surfaces

Throughout history, maps have been essential tools used by explorers and scientists to understand our planet and surrounding solar system. A map is a visual representation of an area depicting the relative locations of geologic features to scale. Humans have been creating maps of important geologic resources, coastlines, and topography since at least 1150 B.C.E., with the first known geologic map illustrating locations of valuable minerals of Wadi Hammamat in Egypt (Harrell and Brown, 1992). Mapping the coastlines of Earth's continents was a priority for several nations during the Age of Discovery in the 15th and 16th centuries. On land, geologists and surveyors began to create detailed maps of the Earth's surface, documenting the distribution of rock

types, mineral resources, and geomorphological features. These geological maps were crucial for the development of mining and agricultural industries, and they laid the foundation for modern Earth science. In the 20th and 21st centuries, advances in technology have revolutionized the field of mapping. Aerial photography, satellite imagery, and remote sensing techniques have enabled scientists to create incredibly detailed maps of the Earth's surface, revealing features that were previously unknown or difficult to access. In addition, the integration of digital mapping technologies with GPS and geographic information systems (GIS) have made it easier than ever for people to navigate and study the world around them.

Our exploration of the solar system has paralleled our exploration of Earth. The first known map of the stars is from 7th century China (Bonnet-Bidaud et al., 2009). Later, William Gillbert mapped the surface of the moon in 1603, before the invention of the telescope. Thomas Harriott, Galileo Galilei, G. C. LaGalla, and P. Christoph Scheiner used groundbreaking telescope technology to update these maps (Kopal, 1969). In 1977, the launch of the Voyager missions represented another leap in technical mapping ability, by sending robotic cameras out into the solar system to survey bodies as they flew by, beaming the data back to Earth. As a result, today detailed maps exist for most planetary surfaces in our solar system, many subsequently updated with new telescope and satellite data.

When exploring a planetary surface via satellite, observations from different instruments during the mission are often combined into various forms of geologic maps, geodetic coordinate reference frames, topography, and orthoimages. These data products provide a foundation for planetary scientists to build scientific interpretations(Naß et al., 2017; Laura and Beyer, 2021). In 2019, the United States Geological Survey (USGS) conducted a survey of planetary geoscience map makers and users and found these products to be critical to the planetary science community (Jr et al., 2019). These maps are used to formulate and answer science questions, such as: was there ever abundant water on the surface of Mars? Was Mars ever habitable, and did it ever develop life?

1.2 Climate Studies of Mars: New Models derived from Topographic Maps

The desire to understand Mars has captivated the interest of the public, resulting in an effort to globally map its surface and billions of dollars of sustained investment. According to a 2017 report from NASA's Office of the Inspector General (OIG), NASA had spent more than $21 billion exploring Mars since 1964 (OIG, 2017). The recent Planetary Science and Astrobiology Decadal Survey: Origins, Worlds, and Life recommends continuing this investment with the Mars Sample Return (MSR) mission as the community's top scientific priority for NASA's robotic exploration program (NASEM, 2022). The science goal of MSR and NASA's most recent mission, Mars 2020, is to assess the ancient habitability potential of Mars and search for biosignatures (evidence of ancient life).

When evaluating the potential habitability of a planet, McKay (2014) developed a generalized checklist of essential features that should be present. On ancient Mars it is plausible that many, if not all, of these requirements were satisfied, making it a compelling target for habitability studies and the search for extraterrestrial life. Perhaps the most contentious aspect of Martian habitability is the availability of liquid water (McKay, 2014). Proving the existence of water on Mars is crucial not only for determining if Mars was suitable to host life as we know it, but also for understanding the planet's dramatic climate change as the current Martian atmosphere cannot sustain temperatures warm enough for water. Abundant geological evidence suggests a global presence of water during the Noachian epoch, $\sim 4.1 - 3.7Ga$ (Hartmann and Neukum, 2001). Surface features in these units appear to require an abundance of water during their formation, indicating a warm, wet climate with flowing surface water. However, some scientists argue that Mars likely maintained an icy cold climate, with surface temperatures below water's freezing point and periodic localized melting due to events such as impacts or volcanic eruptions. These low temperatures are estimated by climate models, with factors such as the the large distance from the Sun ($\sim 1.5\times$ farther than Earth), and the faint young (emitting 75% of the radiative intensity compared to the present-day sun) (Feulner, 2012).

Chapter 2 evaluates part of the geological evidence for past water on Mars, specifically examining the distribution and number of valley heads which required surface water during their formation. Simulations were performed to predict valley head distribution scenarios when water is sourced from an icy cold versus a warm wet ancient Mars. Building on previous work mapping valley networks by Hynek et al. (2010), data from Noachian aged units on Mars was also evaluated. Elevations of valley heads were extracted from the digital elevation model (DEM) produced from Mars Orbiter Laser Altimeter (MOLA) data (Smith et al., 2001). The normalized distribution of valley heads is compared with simulation results to gain insight on Mars' ancient climate and surface water. This demonstrates the enormous scientific value of maps derived from remote sensing measurements.

1.3 Orbital Remote Sensing Techniques

Remote sensing is a technique that allows scientists to observe and study the properties of a target without making physical contact with it. This is particularly useful for planetary exploration, where sending instruments to make measurements directly on the surface of another planet is complex, expensive, and risky. Instead, planetary scientists rely primarily on remote sensing data collected by satellites in orbit, supplemented with limited samples (meteorites that have hit Earth) and surface-based measurements. This makes understanding the principles of remote sensing essential to interpreting theories of how our universe works.

An everyday example of remote sensing is our eyes. When we look at something, we collect light in the visible spectrum that has been reflected or emitted by those objects. This process happens passivley and allows us to determine properties about what we are looking at, such as color, shape, and texture, to deduce information about the environment. For example, we can see white clouds in the sky due to the uniform scattering of visible light off of much larger water molecules (i.e. Mie scattering). However, visible light makes up a small portion of the electromagnetic (EM) spectrum, and may not provide a complete picture. For instance, you might have noticed that mornings after cloudy nights are generally warmer than mornings after clear nights. Clear skies

look blue due to the strong Rayleigh scattering of blue light off of similarly sized air molecules ($0.4 - 0.5\mu m$). Based only on the information from the visible spectrum, you might expect the cause to be reflection of light from the clouds back to the ground warming the air. However, if we expand our measurement spectrum to longer wavelengths past what our eyes can see, we will observe that clouds are black in the infrared (IR) due to water absorbing energy in this wavelength. This heat is then re-emitted by the clouds back down to the surface, which is the actual cause for warmer mornings (Bohren and Clothiaux, 2006). Thus information from the visible to IR range is required to fully understand this physical phenomenon.

In the context of planetary exploration, a suite of remote sensing instruments on orbiting spacecraft is often designed to collect data over a wide range of the EM spectrum. Each instrument intercepts EM waves that have interacted with their target on a planet, and uses the resulting change in phase, amplitude, and/or polarization to infer the properties of the target such as composition, temperature, and size. Remote sensing instruments can be classified as either active or passive. Active instruments generate their own EM radiation that they beam at the target, and then measure the radiation that is reflected or scattered back. An active instrument was used to build the DEM used in chapter 2. MOLA transmits light and measures the time of flight of the reflected signal to determine the range between the spacecraft and the surface. This data was used to construct a precise topographic map of the surface (Smith et al., 2001). Passive instruments detect natural radiation that is reflected or emitted by the target, such as sunlight that has reflected off the surface of a planet. Reflectance spectroscopy, which involves delineating the reflected EM waves by wavelength, is the passive remote sensing technique used in this work.

Hyperspectral imagers are often reflectance spectrometers. Hyperspectral imaging (HSI) refers to a process where spectral information is collected for each pixel in the image of a scene. The pixel's spectral information is collected in wavelength bands with a width defined at half of the maximum spectral intensity. This provides a wavelength resolution measure for the spectrometer referred to as the full width half max (FWHM). Generally, 'hyperspectral' imagers have hundreds to thousands of bands with a FWHM of $\approx$1-20 nm makes them, and 'multispectral' imagers have

10s of bands with a FWHM of ≈0.5-10 μm. This spectral information is used to identify materials, objects, or processes. When EM waves interact with a mineral, various absorption processes occur which give rise to diagnostic spectral features that act like fingerprints which can be used for identification.

The shape, position, and depth of these feature vary based on the mineral's unique crystalline structure. VNIR features in the range of $0.35 - 1\mu m$ are usually caused by electronic transitions between elements (such as iron, titanium, and oxygen) with an anion (Bishop et al., 2019). Types of electronic transitions include crystal field transitions, metal charge transfer, and inter-valence charge transfer. Crystal field transitions occur when one of the d orbital electrons transitions to different energy states under the influence of VNIR light. This process is usually temperature sensitive which must be taken into consideration when interpreting the spectra. Another common absorption process is oxygen to metal charge transfer, which is particularly useful for identifying iron. Oxygen to Fe^{3+} absorbs in the blue/violet end of the visible spectrum, which is why minerals like hematite and goethite often appear rusty red/orange in color (Bishop et al., 2019). Inter-valence charge transfer occurs when a pair of metal ions, such as $Fe^{2+} - Fe^{3+}$ or $Fe^{2+} - Ti^{4+}$ are close together in a structure and transfer an electron, temporarily changing their oxidation states. This is typically observed in micas, pyroxenes, amphiboles, and tourmalines (Bishop et al., 2019).

Absorption features caused by vibrational processes are particularly important to identify hydrated and hydroxylated minerals with VNIR light. Vibration can be caused by stretching (ν), bending (δ) and/or a combination ($\nu + \delta$) within minerals. The mass and charge of the atoms, electron density of atoms or molecules in the structure, and physical properties of the crystal will affect the vibration of groups of atoms in the molecule. Typically, atoms with shorter bonds will vibrate at high frequencies, and heavy atoms will vibrate at low frequencies. In NIR, these absorptions are observed in minerals containing OH, H_2O, OH^-, NO_3^-, ClO_4^-, CO_3^{2-}, SO_4^{2-}, and PO_4^{3-} (Bishop et al., 2019). For instance, clay minerals exhibit distinct absorption features in the 2.2–2.5μm region due to OH combination bands. The exact position and shape of these features can be used to distinguish between different clay mineral groups, such as kaolinite, smectite, illite,

and chlorite (Bishop et al., 2008). However, confounding variables such as grain size, roughness, temperature, and viewing angle can also impact VNIR light, and may obscure small differences in absorption features.

The complex nature of light interaction with minerals makes it impractical to model the reflectance spectra of every possible rock and mineral assemblage. Instead, we rely on empirical measurements from naturally occurring pure and mixed minerals for spectral references. Since there are thousands of minerals, it is sometimes convenient to group them into a subset based on the wavelength range of their absorption features. For instance, since hematite has an absorption feature from $\sim 0.75\mu m - 1.2\mu m$ (shown in Fig. 1.1), in this work it is in mineral group 1. Since calcite has a feature between $\sim 1.75\mu m - 2.5\mu m$ (shown in Fig. 1.1), in this work it is mineral group 2. Muscovite has features around both 1.4 and 2 μm (shown in Fig. 1.1), and could be included in both groups. The selection of minerals and groups in this work matches the mineral groups developed by Clark et al. (2003).

The Compact Reconnaissance Imaging Spectrometer for Mars (CRISM) is a HSI on the Mars Reconnisance Orbiter (MRO) satellite (Seelos et al., 2023). The CRISM team has several types of data products, including maps of mineral deposits (Kamps et al., 2020). Parente et al. (2019) used CRISM's spectral data to identify Mg-carbonate and Mg-smectites, and the spatial distribution of that data to produce mineral maps at the Jezero Crater landing site for the Mars 2020 science team. These minerals were mapped in and around the delta, identifying possible contacts that are important areas to study in situ to understand the lacustrine stratigraphy sequence (Parente et al., 2019). If these units are not mapped from orbit, the rover could drive right by the contact without stopping to collect data, missing important details that may explain some of the chronology of the ancient climate in that region. The detailed geologic mapping of Jezero Crater, supported by CRISM data, has enabled scientists to pinpoint scientifically valuable targets for the rover, enhancing the mission's ability to search for signs of ancient life and study the planet's geologic history.

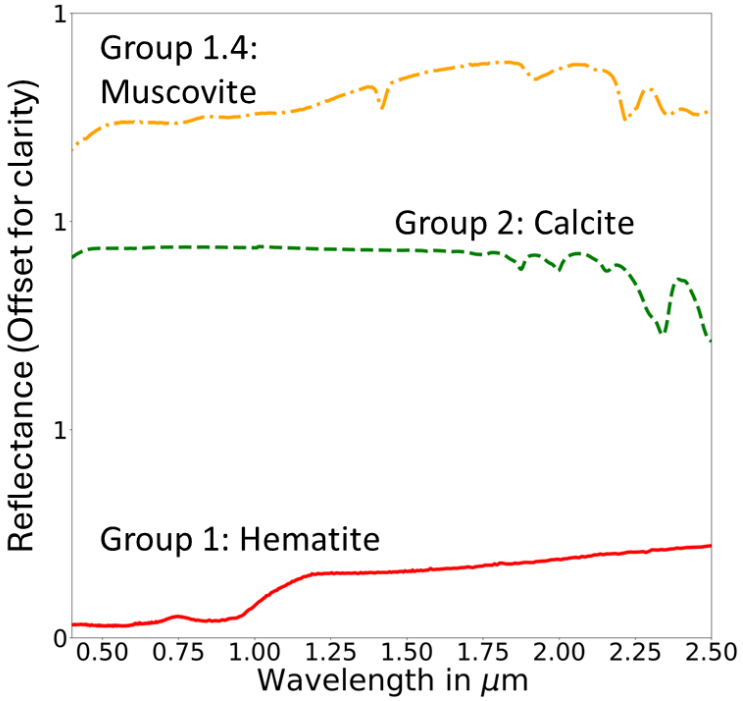

Figure 1.1: Sample visible-near infrared spectra of minerals. Hematite (solid red line) is an example of a 'group 1' mineral because it has an absorption feature around $1\mu m$. Calcite (green dashed line) is an example of a 'group 2' mineral because it has absorption features around $2\mu m$. Muscovite (orange dot dashed line) has features near 1.4 μm and 2 μm, so could be included in both the 1.4 and 2 μm groups.

1.4 Acquiring Geologic Context with Planetary Aerial Vehicles

Geologic context is a broad understanding of regional geology including spatial and temporal relationships between different rock units and geologic features. HSIs are able to rapidly retrieve spatially-resolved spectral data over a wide area, making them ideal for geologic context acquisition. Reflectance HSIs use the sun as an illumination source and can often be designed without moving parts, making them well-suited for integration with spacecraft where size, weight, and power (SWAP) considerations are paramount. HSIs enable the identification of compositional variations in the scene that may not be apparent in visible imagery alone, aiding scientists when distinguishing geologic units. Mounting this payload on a mobile platform such as a planetary aerial vehicle is an ideal way to acquire quick, broad scans of the surroundings. Drone mounted HSIs have been popular on Earth for the last decade, being commercially developed primarily for the agriculture and forestry industries (Adão et al., 2017; Matese et al., 2024).

The number of scientific journal papers and mission proposals for aerial vehicles on Mars have increased over the past 30 years (Saez et al., 2021). The first helicopter flown outside of Earth is Ingenuity, which was sent to Mars as a technical demonstration with no other science goals. Once Ingenuity met (and surpassed) its engineering goals, the team repurposed it to scout Martian terrain for the Perseverance rover, since its cameras, although lower in spatial resolution than the rover mounted cameras, provided much higher resolution of the rover's planned traverse path when compared with satellite data, as seen in Figure 6 of Tzanetos et al. (2022). This use of Ingenuity improved rover operations by identifying obstacles, enabling operators to adjust trajectory ahead of the scheduled rover traverse (Tzanetos et al., 2022; Anderson et al., 2023). The operational and technical advantages that Ingenuity successfully demonstrated have inspired many new mission concepts to utilize the planetary aerial vehicle platform. Sample Recovery Helicopters have been proposed to replace rovers for the Mars sample return (MSR) (Mier-Hicks et al., 2023), and the Mars Science Helicopter is proposed to carry kilograms of instrument science payloads and make traverses up to 10 km (Bapst et al., 2021; Brockers et al., 2022). Engineers are studying different

variations of the aerial platform including hexacopters (Sopegno et al., 2024) and octocopters (Zhu et al., 2023).

Planetary aerial vehicles are also being proposed to explore moons. For Earth's moon, there are several types of airless aerial vehicle concepts that take advantage of the low gravity environment to travel by hopping across the surface. Several are in development for the Artemis lunar exploration program, for instance to collect data in permanently shadowed regions (PSRs) of craters, which are exciting scientific targets that may retain water ice (Moon et al., 2021; Schörghofer and Rufu, 2023). These PSRs bring the added challenge of non ideal lighting conditions for spectroscopists, and instruments may benefit from a unique viewing angle achieved with an airless aerial vehicle (Kloos et al., 2021; Tonasso et al., 2024). Similarly, the Dragonfly mission team is developing a helicopter to visit Titan, a moon of Saturn. Titan has a very dense and optically thick atmosphere that can sustain many kilograms of mass in flight (Lorenz et al., 2018). Because Titan's atmosphere is nearly opaque in the visible wavelengths, reducing the the distance from sensor to the target (therefore reducing the amount of atmosphere to penetrate) with a mobile surface platform will improve the scientific return when compared to an orbital platform(Barnes et al., 2021).

1.5 Limitations of Earth-based Planetary Analog Testing: a Wet Atmosphere

Water vapor, despite making up only $0-4\%$ of Earth's atmosphere, is one of the most important gases for remote sensing due to its strong absorption features in the NIR, particularly around $1.4\mu m$ (see Fig. 1 in Barducci et al. (2004)). This feature will complicate the observation of the surface by significantly attenuating signals from space, air, and ground based instruments. VNIR spectrometers such as the Airborne Visible / Infrared Imaging Spectrometer (AVIRIS) typically delete these channels, since their signal level drops below the noise floor of the instrument. Conversely, the atmosphere of Mars is predominantly made up of CO_2, with no significant amount of water vapor. The wavelengths around $1.4\mu m$ are available for spectroscopy and are often used to identify clays by the octahedral metal - OH bond. A similar diagnostic feature is shown in the muscovite spectra from Fig. 1.1. This feature is typically not available to sensors detecting through

Earth's atmosphere.

Chapter 3 evaluates if a spectrometer can get closer to its target to acquire data through this water absorption band, and if the data in that band can be used for mineral identification. A tripod-mounted remote spectrometer in the near infrared ($0.9 - 1.7\mu m$) measured a sample rock through a thin (one meter) atmosphere. A novel method was developed to identify minerals from the 1.4μm feature which are compared with minerals identified by measurements from contact spectrometers with no atmospheric attenuation. Additionally, minerals with absorption features around 1.4μm are evaluated to see if they are diverse enough to be used for unique identification.

1.6 The Resolution Gap between Orbital and In Situ Measurements

Prior to Ingenuity, surface operations exclusively consisted of landers, rovers, and occasionally astronauts. These teams relied on orbital datasets for context and guidance. Planetary science operations will become increasingly challenging as we explore surfaces farther into the outer solar system, as larger distances from Earth-based mission operations causes additional communication delays, reduced opportunities to send additional supplies and/or updated technology from Earth, and higher mission costs. Robots and astronauts collect measurements and physical surface samples which become valuable opportunities to ground truth remote sensing datasets. This ground truthing often compares datasets collected at the scale of tens of meters or kilometers to measurements collected at the centimeter or micron scale, often with little data bridging these spatial scales.

Over the course of surface operations, building a detailed understanding of the local stratigraphy requires synthesis of orbital data with surface measurements obtained through direct contact with rocks. This introduces three primary problems: (1) Scale discrepancies: Some features will be missed when observing an area at a 1 km spatial scale compared to the same area at a 1 cm scale. (2) Incomplete sampling: Rovers do not evenly sample the field site and may drive past important rock boundaries without detecting them. (3) Mineral mixtures: Rocks are often composed of several minerals, complicating their identification and characterization.

During our exploration of Mars, there have been several examples where in situ micro-scale

results seemingly did not align with the large-scale orbital context. Before the Mars Science Laboratory (i.e. Curiosity) rover landed in Gale Crater in 2012, scientists conducted a thorough remote sensing campaign dedicated to characterizing this landing site. This effort determined that basalt most likely dominated the Noachian aged units. Upon arrival however, they were surprised to find evidence of felsic rocks in the crater wall. In this case, feldspar is difficult to identify in the near infrared, making orbital identification challenging (Sautter et al., 2016). Similarly, the first drilled samples of the mission found phyllosilicates in 18-22 wt% of crystalline material measured from mudstones in the Yellowknife Bay formation (Vaniman et al., 2014). However, mineral mapping from orbit with CRISM found no phyllosilicates in orbital data, likely due to dust cover (Sheppard et al., 2021). Generally, after evaluating the orbital and in situ mineral identifications at Gale Crater in later stages of the mission, identification of Fe-oxides and phyllosilicates follows a similar trend. Both were found where expected from orbit, but Curiosity also found they were much more widespread (Sheppard et al., 2021). After decades of studying Mars with state of the art remote sensing from orbit, these surprises demonstrate continued need for in situ measurements.

Interpreting in situ Martian datasets from Earth is also a challenging task. For instance, the Mars Pathfinder mission team took 88 days to determine the geologic history of its landing site when many geologists believe they could have made the same progress using only a rock hammer and hand lens in a few days (Anderson et al., 2021). To minimize the impact of this latency, scientists and engineers work hard to optimize the science operations schedule. This has historically required operators to live on Mars time, which requires 2.75% longer days, forcing schedules to fall out of sync with the rest of family and society living on Earth. This is now only required during the early years of a mission to drive the rover(s), interpret data, and make science decisions in real time (Squyres, 2005; Eppler et al., 2013; Yingst et al., 2013). However, studies in Earth analogs have shown that this structure creates a high-pressure environment which is not ideal to interpret geologic contexts of new field sites (Yingst et al., 2017). This format was a necessary step to get science payoff from the limited design lifetime of hardware in the early days of Mars exploration and was enabled by the short communications delay of 5-20 minutes between Earth and Mars.

In chapter 4, I will integrate in-situ hyperspectral imaging with a larger science team and contrast contextual clues produced by arial imaging, rover based micro-scale measurements, and mesoscale hyperspectral imaging. In this work I will once again use the mid-scale resolution remote sensing spectrometer (PikaIR). Integration of datasets from instruments operating at different spatial scales is essential for improving the accuracy, autonomy, and speed of establishing geologic and contextual interpretations. Without the access to vast computing power at remote locations to enable high quality global measurements of small-scale features. A mixture of broad-scale aerial imaging, mid-scale hyperspectral imaging, and rover-based micro-scale measurements can both provide valuable contextual data and resolve finer details, such as mineralogical variations or biosignature distributions, that may not be apparent at larger scales. Studies like those by Flahaut et al. (2017) and Warren-Rhodes et al. (2023) reinforce this multi-scale approach. Warren-Rhodes et al. (2023) demonstrated that combining broad-scale VNIR spectroscopy, mid-scale Raman spectroscopy, and precise XRD analyses yields complementary datasets that enhance mineralogical interpretations, particularly for complex or heterogeneous samples. Similarly, Warren-Rhodes et al. (2023) showed how macrohabitat and microhabitat scales contribute differently to biosignature detection, with fine-scale features like alabaster surfaces strongly correlating with microbial colonization. These findings highlight the need to integrate multi-scale datasets to fully understand both geological and biological contexts in Martian exploration.

1.7 Summary: Developing New Techniques to Study Planetary Surfaces

The search for life on planetary surfaces is my primary science objective and will require a multifaceted approach. This chapter links together three remote sensing projects developing new techniques towards this goal, and introduces the main concepts of this thesis. In chapter 2, Martian data is used alongside novel modeling techniques to gain insight on whether there was water on the surface of Mars during the Noachian epoch. Understanding the history of water on Mars is an important factor when assessing its ancient habitability. The habitability potential of ancient Mars has been studied for decades by teams all over the globe, and is the primary science goal of

the Mars 2020 mission. This team chose to sacrifice some of their available size, weight, and power (SWaP) to include Ingenuity, a technology demonstration of the first PAV on another planet. This thesis considers how adding a VNIR hyperspectral imager to Ingenuity could contribute to the study of Martian habitability by mapping hydrated minerals. The innovative mobility of a PAV introduces new advantages and challenges for spectral analysis. In chapter 3, the broad range of possible distances to the target, and corresponding varying atmospheric attenuation in the signal, is discussed. This is first considered for an Earth environment to develop novel mineral identification techniques around the 1.4 μm water absorption band, which is useful for capturing additional spectral features that are common in clays that are typical in these lacustrine and deltaic settings. Chapter 4 investigates how these technologies can be used to improve planetary surface exploration addressing the challenge of identifying minerals with data from different spatial scales (in orbit vs. at the surface). I used VNIR spectral data from orbital and in situ instruments with spatial and spectral resolutions similar to instruments available at Mars. I tested a middle resolution drone mountable platform in a simulation of planetary surface operations to see how this additional data could improve the assessessment of the geologic context of the field site. The field site has little vegetation and laminar stratigraphic layers of lacustrine origin, and containes mudstones with small grains that are thought to be ideal for preserving biomarkers and with some similarities to the Jezero crater river delta on Mars being explored by the Mars 2020 mission, although with differences in mineral diversity. Each of these techniques can also be extended for use on other bodies beyond Earth and Mars.

Chapter 2

Landscape Evolution Models of Incision on Mars: Implications for the Ancient Climate

This chapter was submitted to JGR: Planets on 7/14/24 and is currently under review.

Abstract

Large dendritic valley networks observed on Mars present a paleoclimate paradox. Geologic observations of Noachian units on Mars reveal a global extent of valley networks, which are believed to have been formed through incision by flowing water. However, most climate models predict global surface temperatures too far below the freezing point of water to support an active hydrological system. The conflicting observations and models have led to disparate theories for the climate of early Mars. In this work, we surveyed a large region of the cratered southern highlands to identify the location, elevation, and distribution of observed valley heads. These valley head locations were compared to landscape evolution simulations in which the spatial distribution of runoff was varied. The measured valley head distributions were compared to predictions from landscape evolution models for two end-member hypotheses: 1) a warm wet climate that supported spatially distributed precipitation, and 2) surface runoff from ice cap margins, as envisioned by the Late Noachian Icy Highland model (LNIH). The observed elevation distribution in valley heads is consistent with the prediction of precipitation-fed models, and inconsistent with models in which runoff derives exclusively from high-elevation ice-melt sources. The results support the view that it is unlikely

for ice caps to be the sole source of water and are consistent with the hypothesis that precipitation significantly contributed to valley network formation on ancient Mars.

2.1 Introduction

The geologic record from the Noachian epoch, $\sim 4.1-3.7Ga$ (Hartmann and Neukum, 2001), reveals extensive dendritic valley networks that span most of the southern highlands (Carr, 1995; Luo and Stepinski, 2009; Hynek et al., 2010; Alemanno et al., 2018; Kite et al., 2019), which indicates the presence of sustained liquid water on the planet's surface. Craddock and Howard (2002) and Hynek et al. (2002, 2010) identified surface characteristics consistent with the occurrence of precipitation and runoff, while Morgan et al. (2022) found evidence of water-emplaced fans, which suggest a period of millions of years with a stable hydrosphere. These characteristics are indicative of sustained liquid water and provide geologic evidence for a warm wet climate (Ramirez and Craddock, 2018). Hoke et al. (2011) used a variety of sediment transport models to determine that the larger valley networks required up to 10^7 years of continuous geomorphic activity to form. Numerous authors have identified additional features suggestive of a warm and wet climate. For instance, fan deltas are globally observed across Mars (Malin and Edgett, 2003; Irwin III et al., 2005; Di Achille et al., 2009; Di Achille and Hynek, 2010) and were likely formed by flowing rivers depositing sediment as they drained into large bodies of water, although alternative models exist (Vaz et al., 2020). Similarly, paleolakes (Fassett and Head III, 2008; Goudge et al., 2016) provide examples of features on Mars that required at least brief episodes of warm wet conditions to form. Further, networks of sinuous ridges, which were interpreted to be inverted channels, have also been observed (Burr et al., 2009, 2010; Lefort et al., 2012). Collectively, this varied set of features in the geologic record require significant time to form, indicating sustained and long-lived hydrologic activity (Gulick and Baker, 1989).

Beyond the geomorphic evidence, geochemical and mineralogical observations from spectral measurements provide evidence of previous surface water. Evidence for aqueous alteration of minerals was identified by the CRISIM and OMEGA imaging spectrometers. These deposits are a

result of water-rock interactions with the Martian crust and primarily consist of phyllosilicates, hydrated silica, sulfates, and chlorides (Arvidson et al., 2005; Murchie et al., 2007, 2009; Hynek et al., 2010; Osterloo et al., 2010; Carter et al., 2013; Ehlmann and Edwards, 2014). Recently, a global map of these mineral deposits has been published that shows more widespread evidence of ancient aqueous alteration than previously identified (Carter et al., 2023).

In-situ observations from the surface corroborate the remote sensing detections. For instance, the Opportunity rover found sedimentary rocks with abundant sulfate salts containing cross-laminations and chemical and siliciclastic sediments, and at one locale contained evidence for deposition in shallow flowing water (Squyres et al., 2004). Further, pebbly conglomerates were discovered with data from the Curiosity rover (Williams et al., 2013) in addition to evidence for a long-lived lake (Grotzinger et al., 2014; Hurowitz et al., 2017; Heydari et al., 2023). The Perseverance rover is currently exploring a delta, which likely formed from a river that once flowed into an ancient lake in Jezero Crater, and has confirmed some of the orbiter spectroscopic observations of aqueously altered minerals (Farley et al., 2022). The climate conditions that caused the creation of the altered minerals across the Noachian landscape must have involved significant water: a condition quite different from the current cold and hyper-arid environment.

The geologic and geochemical evidence for a warm and wet ancient Mars is difficult to reconcile with most climate models for the Noachian era. These models predict a past climate that was colder and less hospitable to surface water than Mars is today. During this earlier era, the faint young sun only emitted 75% of the radiative intensity compared to the present-day sun (Feulner, 2012). Without a strong greenhouse warming effect, the reduced sunlight from the 'faint young sun' would produce a relatively lower mean surface temperature compared to the present. To counteract the effects of a lower incident radiation, models have been developed that predict that a significantly denser CO_2 atmosphere would increase the intensity of the greenhouse effect and warm the surface. However, when modeled on a global scale, this atmosphere is shown to be unstable and tends to condense to dry ice at the poles (Wordsworth et al., 2015). In the models, as the CO2 condenses, it initiates an atmospheric collapse and an inevitable return to, or an exacerbation of,

the current sub-freezing surface temperatures (Pollack et al., 1987; Kasting, 1991; Forget et al., 2013; Soto et al., 2015). Some progress has been made at modeling new mechanisms to maintain a Noachian climate with the necessary surface temperatures and the stable barometric pressures needed to support the observed surface features and not collapse (Wordsworth et al., 2017; Kamada et al., 2020; Ramirez et al., 2020). In these recent alternative greenhouse theories, pathways for higher temperatures require more complex gas compositions, such as $CO_2 - CH_4$ or $CO_2 - H_2$ (Wordsworth et al., 2017; Kamada et al., 2020; Ramirez et al., 2020), to produce the required stability and greenhouse warming conditions. However, in these theories, the sources of these gas combinations and their ability to self-sustain to produce the required partial pressure in early Mars are not well understood.

Geologic evidence for an icy cold past Mars includes observations of extensive non-polar ice deposits from the Amazonian age (Fastook and Head, 2015), Amazonian and Hesperian outflow channels, and post-Noachian fluvial and lacustrine features (Gallagher and Bahia, 2021). These traits indicate that a dry climate has persisted for the past few billion years with repeated outflow channel formation, leading to transient seas or oceans (e.g., Ivanov and Head (2001)) and potentially catastrophic melting of any ice caps (Head and Marchant, 2008; Fastook and Head, 2015). Further, global circulation models imply a cold and relatively dry Mars climate, similar to the Antarctic Dry Valleys, and have been applied to glacier growth (Fastook et al., 2012). While many models point to the challenges of maintaining surface water on Mars, there are still observed valley networks and other features interpreted to have formed from flowing water. To account for fluvial features seen on Mars, a global climate model was proposed by Wordsworth et al. (2013) to provide a mechanism for global water transport from lower elevations to higher ones. This Late Noachian Icy Highlands model supposes that highland ice accumulation does not require a typical hydrological cycle, and that a nominally dry environment can be maintained at lower elevations and still produce the observed features. The model places an atmospheric pressure constraint of greater than a couple 10s of mbar, which is larger than today. Higher pressures are required to produce temperature variations that are dominated by elevation and not latitude, which enables ice caps to form above a

semi-global ice stability line independent of the latitude. Here, the landscape can remain nominally arid and still be eroded by water from seasonal (Palumbo et al., 2018), catastrophic, or intermittent (Palumbo and Head, 2020) melting events, where large water reserves at high elevations are released. These events (e.g. volcanoes, major impacts, etc.) would cause a dramatic heating of the surface or enough lasting atmospheric change to warm Mars and produce substantial surface water (Segura et al., 2002) for long enough to create valley networks. During this time, water would melt out of the ice caps and flow onto the surface of Mars. Models of this nature, in which insufficient greenhouse gases exist to support sustained water, are a sub-set of icy cold mars paleoclimate models. Broadly speaking, this class of model consists of a nominal thin atmosphere producing a mean surface temperature well below the freezing point of water which leads to large regional ice caps that only melt under specific circumstances.

Note that in the icy cold scenario explored in this work, water for valley formation is generated from top-down melting of a cold-locked ice cap, providing runoff along the lower elevation edge of the ice (i.e., Fastook and Head (2015)). In this work, subglacial flow is not addressed because a kilometer or more thick ice sheet would be required for basal melting and the LNIH ice cap likely averaged ¡300 m thick (Fastook and Head, 2015). Here, we chose to use Martian valley networks and landscape evolution models (LEMs) to investigate the competing climatological end members discussed above for ancient Mars. The elevation distribution of Noachian-aged low- to mid-latitude valley heads—the uppermost reaches of valley networks—was compared to the distributions that would be expected from models representing either high-elevation ice cap melt (icy-cold case) or from runoff sourced from spatially widespread precipitation (warm-wet case).

2.2 Methods

2.2.1 Data Analysis

Figure 2.1 shows a map of the selected region of interest (ROI), which encompasses a large number of valley networks contained within the cratered highlands ranging from 20^0S to 20^0N and

from 30^0W to 180^0E. We chose this ROI where the ice cap is expected to form in the Wordsworth et al. climate models, staying at low latitude minimizes any periglacial or glacial effects, and the broad longitude band incapsulates the vast majority of VNs in this latitude band. The topographic data from the ROI were extracted from a Mars Digital Elevation Model (DEM) from the Mars Orbiter Laser Altimeter data (Smith et al., 2001). These data were then processed in ArcGIS to extract the hypsometry data. The large valley networks shown in the sub-figure, were identified by Hoke and Hynek (2009) and isolated from the ROI using a convex hull method. These valley networks were selected for their lower elevations (ranging from $\sim -2000m$ to $\sim 1000m$ above the planetary datum), relatively long length (from about 200 km to 700 km), and dendritic morphology with few disconnected segments. Disconnected segments are associated with post-network impact craters and are intentionally avoided during selection. In general, network relief ranges from 1,000m to 1,500m, where the relief is defined as the absolute difference in elevation between the highest and lowest parts of the network. The first order valley head elevations were identified and catalogued for further analysis. The networks are representative of typical large valley networks on Mars from the Noachian era (Tanaka and Kolb, 2001).

The topographic data were further used to generate a base geometry for the simulations. The hypsometry, or the distribution of elevation in an area, of each of the valley networks was plotted and classified into two representative sigmoidal shapes, as shown in Fig. 2.2. These curves were created by averaging the elevation data perpendicular to the direction of the terrain's slope. For each network, a best fit sigmoid is overlayed atop the averaged valley network hypsometry to create two classes of generalized elevation curves and shown in Fig. 2.2. This method allowed for a simpler and generalized comparison between 'typical' valley networks and the measured surface.

2.2.2 Model Analysis

Model analysis has two parts: first, numerical modeling of a 'generalized' surface with icy cold and warm wet input conditions and second, comparing the results to observed valley network head distributions. To illustrate the relationship between runoff and valley network morphology,

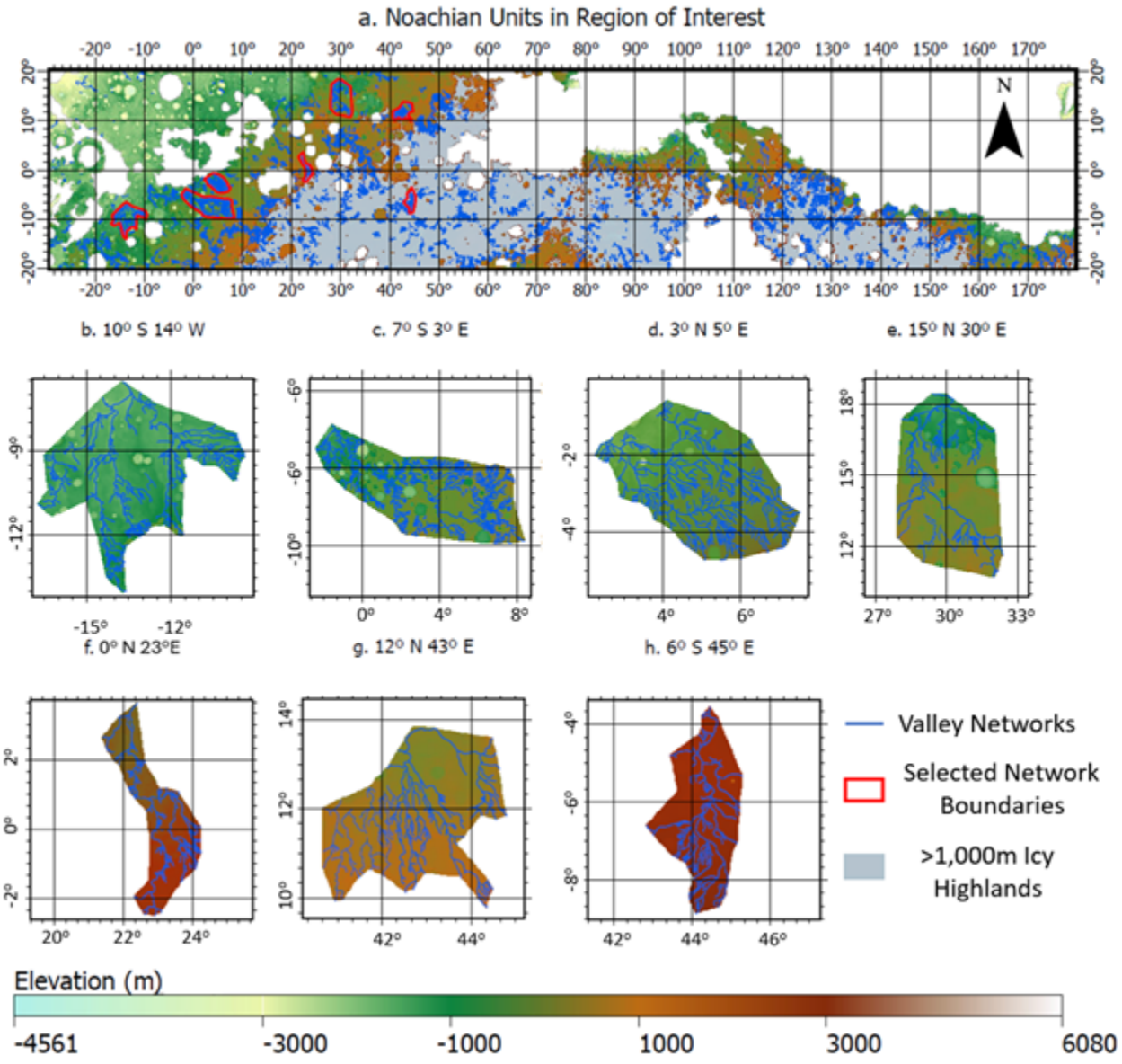

Figure 2.1: Digital elevation model of Noachian units in the region of interest (ROI). Noachian units from Tanaka and Kolb (2001). Elevations above 1000m (the ice stability line) are shaded grey to identify the location of the hypothesized ice cap. The major valleys are identified with red outlines around dark blue lines representing the valleys. b-h: Major valley networks identified in (a) are individually shown, selected from Hoke et al. (2011).

we conducted experiments using a simplified landscape evolution model. The model was configured to address the question how does the elevation distribution of runoff influence the morphology of an evolving valley network on a Mars-like topography. In particular, how does the water source area influence the elevation distribution of valley heads across the landscape? The experiments were configured to represent either a water source derived exclusively from melting of high elevation ice caps, or alternatively, uniform precipitation over the entire landscape. Second, we analyzed a database of mapped valley networks at low latitudes to avoid any glacial and/or periglacial contributions from higher latitudes. From this database, we identified first-order branches of the dendritic networks. The branch number is defined by the number of branches above it in the network (e.g. start of network = order 1, at node where this branch joins another it is order 2, etc.) (Strahler, 1957). Finally, the elevation distribution of the valley heads was compared to the modeling scenarios of widespread water distribution (i.e. precipitation) versus ones from water sources restricted to high elevations (i.e. icy highlands).

2.2.3 Landscape Evolution Modeling

To examine the relationship between water origin and valley network formation, we ran landscape evolution models for two end member climate scenarios; precipitation and melting of high elevation ice caps. The precipitation end member describes a planetary surface that is exposed to precipitation and, in the model, this is manifested by injecting an even distribution of water across the entire watershed. For the high elevation ice cap end member, water is input to the watershed only from the edge of the simulated ice cap. For this work, the elevation was chosen to be 1000 m and specifically tests the canonical LNIH model put forth by Wordsworth et al. (2013), which has gained a lot of traction in the community (Scanlon et al., 2013; Head et al., 2014; Fastook and Head, 2015; Weiss and Head, 2015; Palumbo et al., 2018; Palumbo and Head, 2020). This elevation for the ISL was an assumption in the Fastook and Head (2015). model where they used it to solve for the equilibrium between sublimation and condensation of ice based on this assumption for several environmental conditions. The model explored scenarios with increased water volumes

(e.g., 2× to 20× the estimated amount of water supply) while keeping the elevation of the ISL relatively stable within a LNIH framework. For the LNIH model used here, we further assume that the surface temperature is horizontally stratified, and dominated by elevation, rather than depending on orbital obliquity or other globally unknown parameters.

While simple, the model is intended to both be archetypal of the Martian watersheds and realistically lead to the formation of the observed incision patterns. In terrestrial applications, arguably the most elementary formulation of a physically based model that reproduces hillslope-valley features is one that combines channel incision mechanisms with downslope gravitational transport. The model we use combines fluvial incision, based on a stream power per unit bed area (Howard, 1994; Whipple and Tucker, 1999), and soil creep, where downslope transport depends linearly on hillslope gradient (Culling, 1963). The governing equation for the rate of change of surface elevation in this model, z, is defined by,

$$\frac{\partial z}{\partial t} = -K_{sp} A^{.05} S + D\nabla^2 z \tag{2.1}$$

where t is time, K_{sp} is an erosion efficiency factor (with dimensions of inverse time), A is the drainage area that contributes water flow to a given point, S is streamwise gradient, and D is a gravitational transport efficiency factor (equivalent to a diffusion-like coefficient, with dimensions of length squared per time). Equation 2.1 was solved numerically on a rectilinear grid atop the representative topology with a standard "D8" flow routing procedure to calculate drainage area at each grid node. The gradient, S, was discretized as the elevation difference between a grid node and its downstream neighbor, divided by the horizontal distance between them. A forward Euler method was used to discretize the time derivative. The code that implemented this numerical solution was written in Python and used Landlab. Landlab is a programming library from Community Surface Dynamics Modeling System which provides built-in code for grid generation and components that perform numerical solutions to the fluvial and gravitational terms in equation 2.1 (Tucker et al., 2015; Hobley et al., 2017; Barnhart et al., 2020). The diffusion coefficient, D,

used in the diffusion equation, $\frac{dz}{dt} = D\frac{d^2z}{dx^2}$, has been estimated to range (Cardenas et al., 2022). Here, we used $0.001m^2/My^{-1}$, to produce incision depths similar to those seen on Mars, with the proviso that at the scale modeled, the process should have relatively little impact on the terrain. Assumptions implicit in the fluvial incision term are that the erosion rate scales with stream power per unit bed area (equal to the product of shear stress and mean velocity), that water discharge scales with drainage area, and that channel width scales with the square root of discharge (Whipple and Tucker, 1999). The erodibility coefficient, K_{sp}, depends on several factors, including runoff rate, lithology, sediment load, and temperature. The input parameters used for model scenarios and the two test geometries are summarized in table 2.1. Note that this model assumes that the rate of gravitational movement of sediment on slopes is proportional to the gradient of the surface. In terrestrial environments, this formulation tends to underpredict sediment flux on steeper slopes (Andrews and Bucknam, 1987; Roering et al., 1999).

Table 2.1: Landscape Evolution Model Inputs

Model Inputs	Warm Wet	Icy Cold
Map Size	Nrows: 972, Ncols: 567, dx: 700 [meters]	Nrows: 972, Ncols: 567, dx: 700 [meters]
Run Time	600,000 [years], Dt: 3000 [years]	600,000 [years], Dt: 3000 [years]
Erodibility Coefficient	$K_{sp} = 0.00025$	$K_{sp} = 0.00025$
Linear Diffusivity	$D = 0.001m^2/yr$	$D = 0.001m^2/yr$
Rain/Melt Rate	$0.0143m/yr$ per pixel	$2m/yr$ per pixel
Total Discharge	$96,576m^3/yr$	$96,480m^3/yr$

2.2.4 Model Inputs

Figure 2.2 shows the shape of the initial topographic profiles used in simulations. A sigmoidal curve was chosen for simplicity while having gradients that generally conform to the large valley networks found on Mars. For this work, two different sigmoidal shapes were used, one that generally matches greater relief and steeper Martian valleys (Sigmoid 1) and a shallower profile that generally

matches the profile of more gradual sloping Martian valley networks (Sigmoid 2). The representative and generic topography were used as a starting point and are broadly consistent with the scale and morphology of the large valley networks identified in Hoke et al. (2011) and located in the equatorial region. They are not designed to be specific to any location or valley network. The lengths of the sigmoids match the length of larger Martian valley networks. On the sigmoid shown in Fig. 2.2, the dashed line represents the elevation of a prototypical ice stability line and represents the edge of the highland ice cap. This location is arbitrary and generalizable to any altitude within the context of the model. However, 1000 m was selected as a typical elevation from Fastook and Head (2015).

The two representative sigmoids were used to develop the initial topographic surface for the models. This simplification was developed to be computationally lightweight, plausible, and generalizable to Martian watersheds. The model is not intended to reproduce any specific valley network on Mars, but rather as an indicator of how differences in the spatial distribution of water sources might be reflected in network patterns, specifically in the elevation distribution of first-order valley heads. To convert the 1-dimensional profiles seen in Fig. 2.2 into 2-dimensional surfaces for modeling, the curves were extended in the orthogonal direction to form a 2-dimensional surface with the same profile as the curve. Atop the surface, a small amount of random noise with an amplitude ranging from 0 to 20 m was added to break symmetry and stimulate network formation. These surfaces were used as the initial condition for model calculations of valley network evolution, and the resulting patterns were compared to the observed valley network structure.

Throughout the simulated timeframe, and for each of the simulations, the water input rate was held constant. For the warm wet simulation, the water represents precipitation and is distributed evenly across the water shed. For the icy cold scenario, the lower extent of the ice cap is simulated by a water injection line at a single elevation. This line represents the runoff from top-down melting of the ice cap and omits effects from the ice cap retreat.

Each end member and topography used the same total water volume throughout the duration of the simulation. The erodibility constant and precipitation rate were chosen to produce incision

depths generally consistent with those measured with Mars Orbiter Laser Altimeter data (Smith et al., 2001). Additionally, there is a difference between the simulated precipitation/melt rate per unit area between the two end member models. This was needed to maintain a constant discharge while having a larger number of pixels covering the entire precipitation area, relative to those that border the simulated ice cap. In both cases, the simulation time scale was 600,000 years. When combined with the other inputs, this timescale resulted in incision depths that matched average of the actual valley networks from Fig. 2.1. In the models, the 600,000-year time assumes a constant runoff rate or top-down melting rate. However, it is often assumed valley-incising storms on Earth and past Mars were occurring only $\sim 5\%$ of the time (Hoke et al., 2011; Wolman and Miller, 1960), making these minimum timescales of fluvial activity. In any case, the generalized behavior of the simulations is insensitive to intermittency. Computational resources limit the total grid size, time step, and simulation time. Within these constraints, the cross-slope grid size (y-direction) was chosen to be broad enough to produce several individual valley network profiles, the flow along the valley path (x-direction) was 400 km to mimic the scale of the valley networks, and the elevation change simulates the vertical relief of the valley networks.

2.3 Results

Within the ROI (Fig. 2.1), the locations of valley heads were extracted from MOLA data to determine the distribution of incision onset and compared to elevation distributions of valley heads from the simulated networks. The valley head locations were compiled into a histogram that shows the number of valley heads at each elevation band, normalized by the total surface area within the band. This analysis was completed for both warm wet and icy cold models.

2.3.1 Landscape Evolution Results from Simulated Topography

The generalized Martian landscapes discussed in section 2.2.1 were generated using a landscape evolution model with the surface parameters listed in table 2.1. The model produced a distribution of incised valleys and valley heads. Figure 2.3 shows the results from the LEMs for

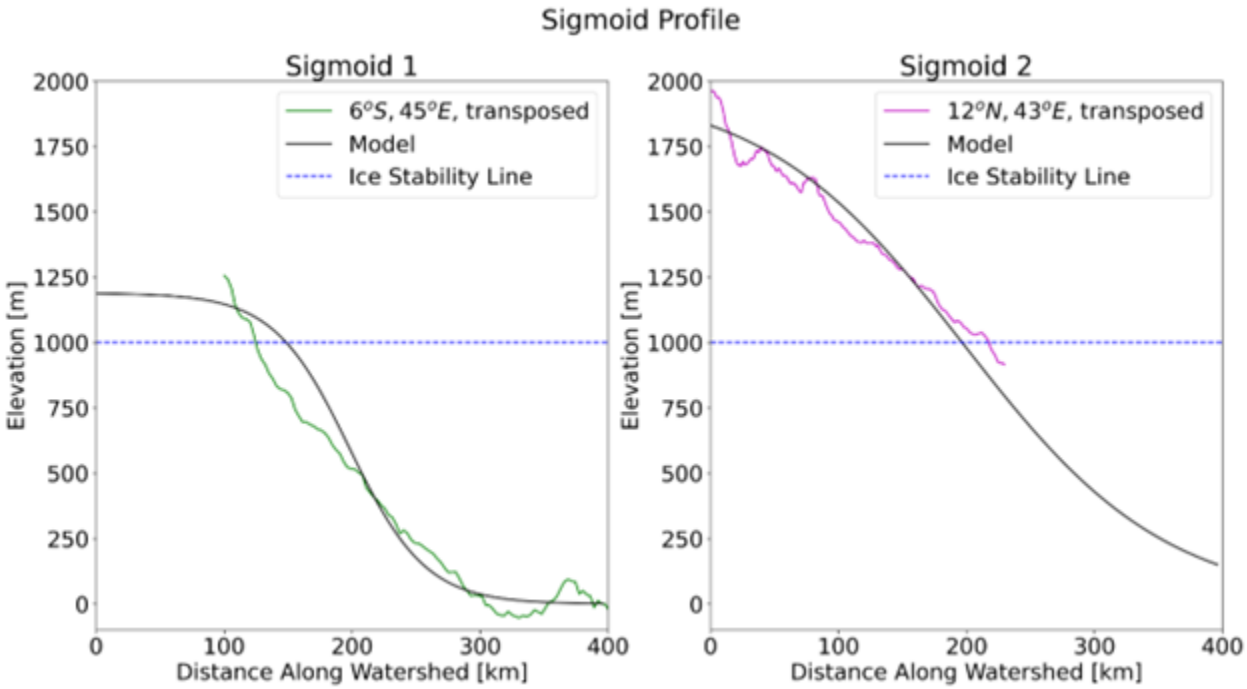

Figure 2.2: Two different sigmoids were selected that are generally representative of topography of large valley networks on Mars. Data from the valley network is plotted in color and the sigmoid selected to represent that shape is plotted in black. The ice stability line representing 1,000m in elevation in plotted as a blue dashed line.

both estimated member water inputs and both sets of input topography. Valley networks were distinguished from the background using a threshold discharge rate of $3,000,000 m^3/yr$. This cut off was chosen to easily identify the major stream locations. Both icy cold and warm wet valley simulations show a complex and branching structure. However, in the case of the icy cold scenario, the lower-order network branches are restricted to higher elevations, close to the source of meltwater running off the hypothesized ice cap, and there is a distinct absence of valley networks at altitudes higher than the ice stability line. The sharpness of this cutoff is a result of simulation limitations where the ice stability line was held fixed over time. An ice cap retreat from a melting event or glacial retreat would produce additional low order valleys at higher elevation. For the warm wet simulations, the lower-order branches are fully distributed over the entire grid.

2.3.2 Martian Valley Network Results

The MOLA-based elevation of every valley head mapped by Hynek et al. (2010) in the ROI, were extracted. The head elevations were grouped into 280 m wide bins to form a histogram of the number of valley heads at a given elevation. These data are shown Fig. 2.4 for the entire ROI and in Fig. 2.5 for the individual valley networks. Each bin in the histogram was normalized by the total area at that elevation, thereby providing a fair comparison of head elevation densities. The normalization limits the over- and under-representation of valley heads due to sample biasing caused by total land area.

For most of the valley networks in the whole ROI, a relatively flat distribution of normalized valley heads as a function of elevation is observed, (Fig. 2.4). Between elevations of about -1800m to 3500m, which encompass $> 96\%$ of the total valley heads, a nearly uniform density is seen. However, below -1800 m a drop in valley-head density is observed. The lower elevations are in the far northwest of the ROI with a landscape showing very low slope and abundant resurfacing. The resurfacing of the large, low elevation area may have erased or buried older valley heads in the northern plains. Higher valley head density is observed above 3500 m and shows a sharp rise. As can be seen in figure 2.4, at these high elevations, the total number of valley heads falls from well

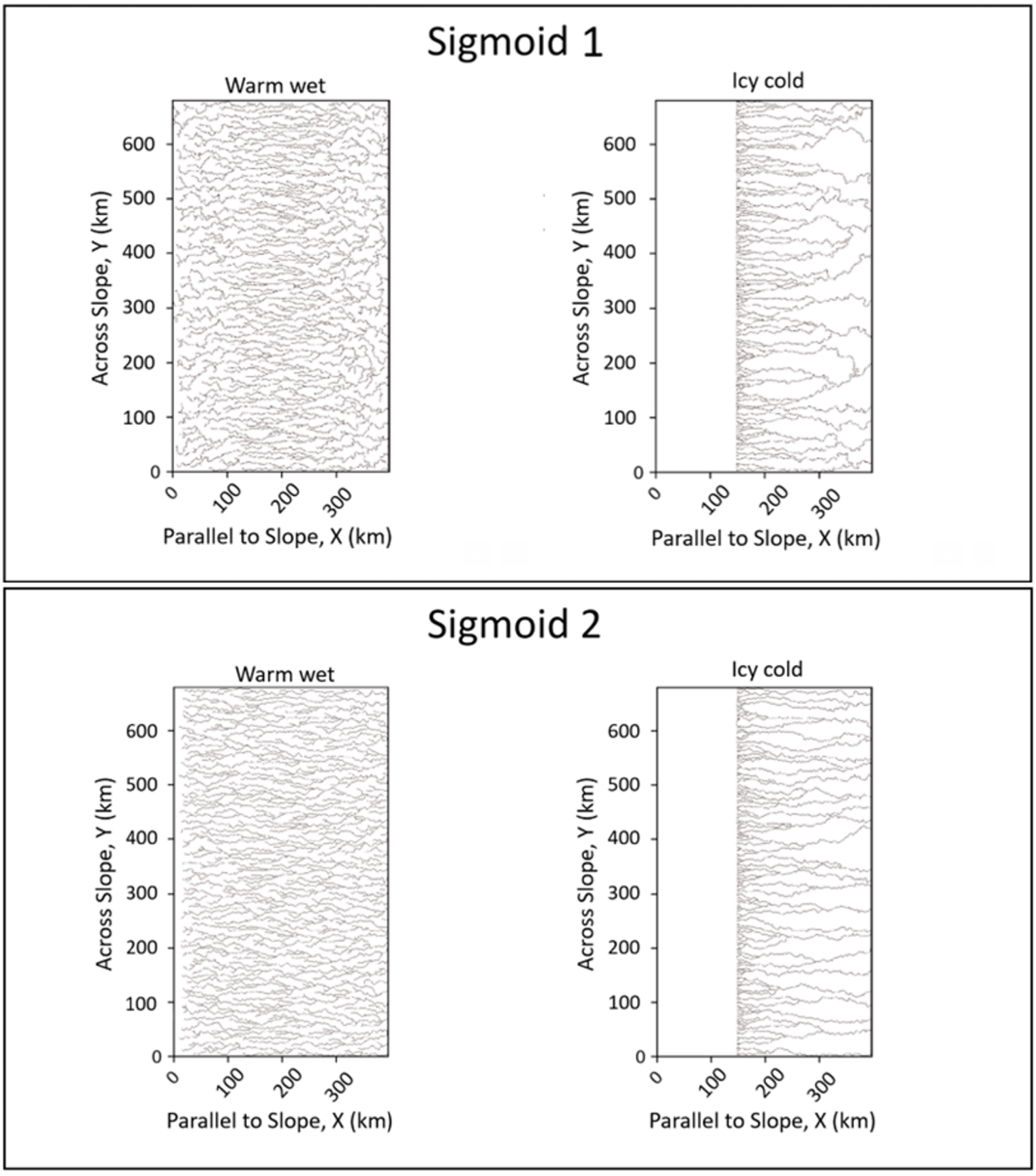

Figure 2.3: Model results: River flow networks were defined using a discharge threshold and represented by black lines. Head elevations were recorded for both initial topography and for both warm wet and icy cold scenarios. Networks from the lower sloped watershed, Sigmoid 1, is shown in the top row, while the steeper watershed, Sigmoid 2, is shown on the bottom row.

over 1,000 to just 50. The drop in the number of valley heads observed is matched by a drop in the total surface area. At these higher elevations both the total number of valley heads and the total area are significantly lower than at lower and midlevel elevations. The smaller numbers for both the highest and lowest valley heads result in greater uncertainty for this area-normalized measurement, making estimated valley-head density sensitive to small changes in boundary selection.

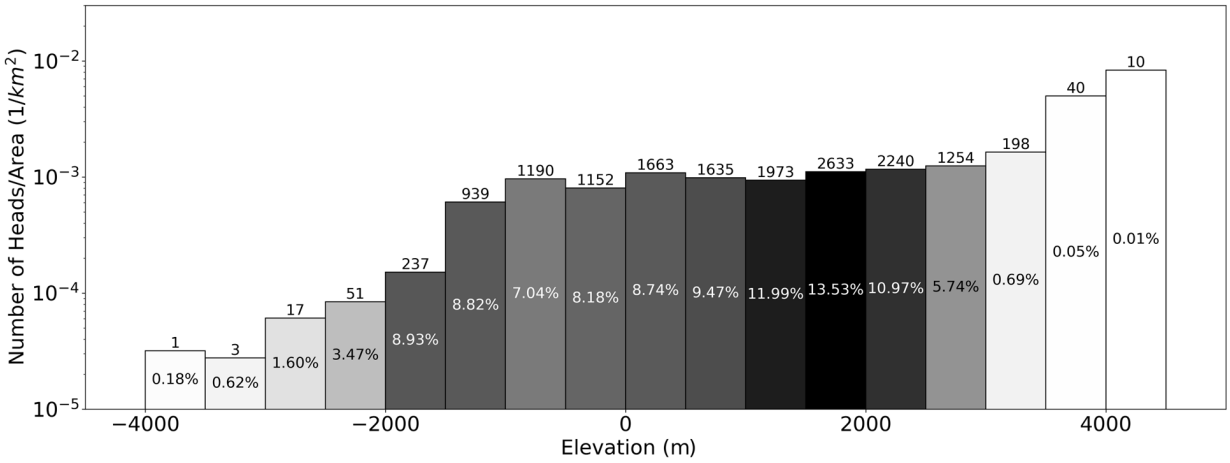

Figure 2.4: Valley head distribution for the ROI. The gray shading indicates the density of valley heads in each elevation bin. The percentage of valley heads in the elevation bin relative to the total is shown inside each bar and the sum of valley heads is written above. The data in this histogram is made available at https://doi.org/10.5281/ZENODO.14029190.

Figure 2.5 expands the figure 2.4 data set to include the seven individual networks studied in the ROI. Valley heads for each watershed are plotted in a different color and overlayed atop the larger dataset. For the individual valley network data, a similar trend is observed where the normalized head distribution is relatively flat with respect elevation and the majority of river heads are located at intermediate elevations. These data show that for both the entirety of the ROI and for individual large valley networks, the location of the valley heads does not appear to have a preferential elevation and are instead more evenly distributed across elevations. There is also no concentration of valley heads at or above 1000 m elevation, which is the hypothesized ice stability line (ice cap edge) of Fastook and Head (2015).

In figure 2.6, the elevation distribution of the valley heads for both simulated Martian to-

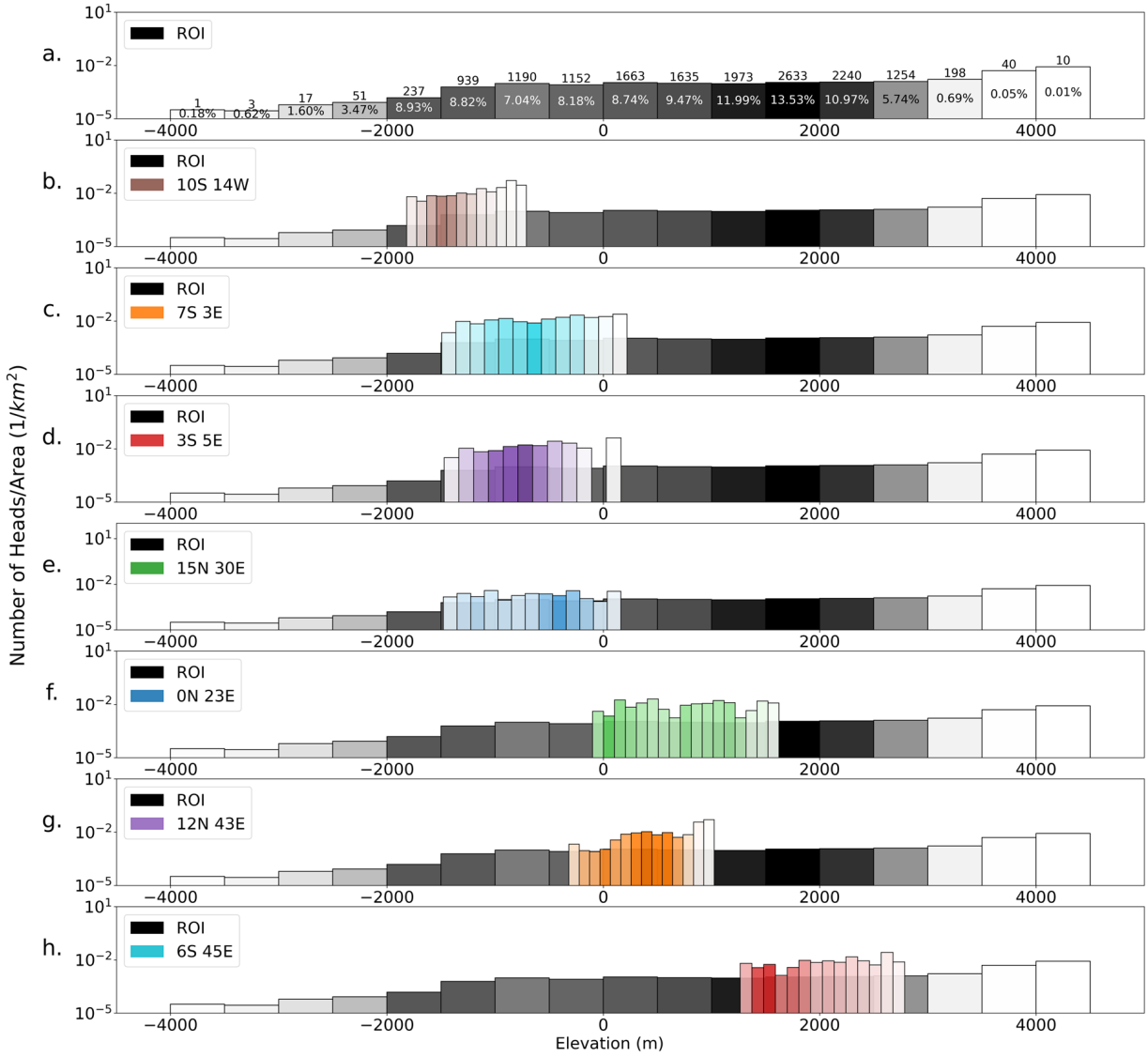

Figure 2.5: Valley head elevation distribution for the entire ROI (grayscale) and individual valley networks from Fig. 2.1 (colors). The shading represents the relative number of valley heads in the bin, with darker bins having more heads and lighter bins having fewer. Lowercase letters reference the valley locations in Fig. 2.1. The data in this histogram is made available at https://doi.org/10.5281/ZENODO.14029190.

pographies (Sigmoid1 and Sigmoid 2) were compared to the distribution from the valley network located at 0^oN and 23^oE. This network was selected for comparison because it crosses the proposed ice stability line, most closely matches the shape of Sigmoid 2, and exhibits relief similar to the simplified simulation topography. The histograms of the warm wet valley head distribution from sigmoid 1 and 2 are shown by opaque grey or pink bars in front of the green 0^oN 23^oE valley network. The icy cold distribution is shown as a dashed blue line. In these simulations, the ice stability line was defined to be immobile and locked to the edge of a stationary ice cap, therefore top-down melting of water from this source results in water entering the simulation at a single elevation and all valley heads to form at that single elevation. This creates an undefined area-normalized valley head distribution at the edge of the ice cap and zero valley heads at other elevations. The subtlety of a receding ice cap during melting events proposed by Head and Marchant (2008); Wordsworth et al. (2013); Head et al. (2014); Fastook and Head (2015); Palumbo et al. (2018) was beyond the scope of this study. However, one can expect that the effect of a retreating glacial edge would result in additional valley heads at higher elevations and a peaked distribution skewed to elevations higher than 1000 m. The variance and skewness of the distribution would depend on the mobility of the glacial edge, the runoff rate, and other unknown factors. As in the existing models, no valley heads would form below the 1000 m ISL. Since this motion was not part of the simulation, the icy cold distribution discontinuity is represented as the single line on the histogram.

The simulation with precipitation reproduces the roughly flat distribution of valley head areal density over the range of elevations investigated. In addition, due to the generality of the modeled landscape it is believed that the ubiquity of valley heads at all elevations is a property of uniform precipitation runoff systems on analogous topographies and is generalizable to the entire ROI. The discontinuous distribution resulting from a cold-locked ice cap is not well represented by the data. However, as the cold-locked ice described by the LNIH model melts from the top down, there is an expectation that the front edge of the ice cap will retreat and produce a distribution of valley heads upslope from the ISL. For a scenario with retreat and growth of the ice cap in the region around the ice stability line, as would be expected for temporary top-down melting from a catastrophic

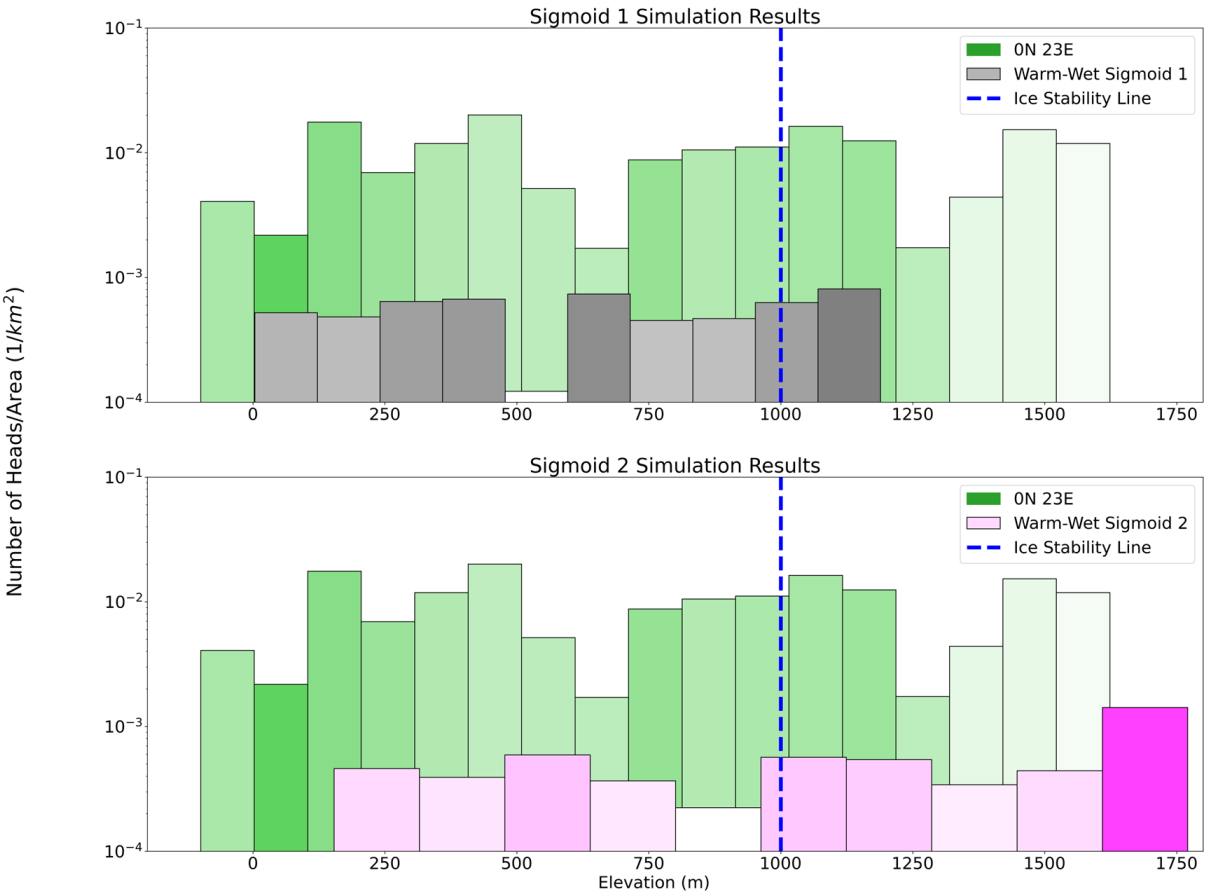

Figure 2.6: Histogram showing the number of valley heads per unit area for the single watershed located at 0^oN and 23^oE and compares it to each of the models. The valley head distribution from the icy cold model is isolated to 1,000m and is shown as a line. If ice cap retreat were modeled, additional valley heads would occur at higher elevations than 1000 m.

event, we would expect to see a band of elevations with many valley heads and relatively few above or below that band. This is not observed in the valley head distribution. Further, if there was a full retreat of the ice cap due to top down melting the data would likely show a strong inflection in the valley head density at elevations above the ISL. This is also not observed.

Despite demonstrating agreement with Mars valley data, e.g., a roughly uniform distribution of valley heads, the simple landscape evolution model has limitations. For instance, the width, length, and simulation time limit the number of branches that develop. These constraints on the simulation area and time, limit the valleys to Strahler stream orders (Strahler, 1957) of 2 or 3, compared to up to 7^{th} order networks found on Mars (Hynek et al., 2010). Finally, the enforced immobility of the ice stability line means that the simulations do not capture the possible effects of a melt source that fluctuates in elevation over time including the retreat of the ice cap during melting events. However, to account for the observed elevation distribution of valley heads, such fluctuations would need to extend well beyond a hypothesized ice-stability line and are not supported by the measurements.

2.4 Conclusions

We modeled two end member climate scenarios for the Late Noachian era on Mars that have been proposed to explain the formation of valley networks. The generalized landscape evolution model results were compared to a survey of valley head elevations extracted from a large equatorial region of Mars to determine which end member climate simulation better described the observations. The scenarios of spatially distributed precipitation in a warm wet climate, and the localized runoff generated from the melt of a high elevation equatorial ice cap were compared. The observed and modeled distribution of valley heads shows similarity to the scenario in which networks formed from spatially distributed precipitation under a warm wet climate. In an environment devoid of precipitation, the model shows that valley head density should peak at the edge of a cold-locked ice cap, which is not well represented by the valley heads in the large region of Mars that was studied. While valley heads do occur at higher elevations in the Martian near-equatorial highlands, there

is little evidence for the concentrations of valley heads at higher elevations that one would expect from a dominantly icy cold environment with no local water sources at lower elevations. These results indicate that the fluvial features on Mars cannot be explained by the cold-locked LNIH model and are better accounted for by widespread, long-lived precipitation and runoff distributed across the drainage basins.

Future work should investigate additional geomorphic indicators, such as branching ratio and sinuosity. Simulation size should also be increased in both spatial dimensions, time, and elevation (relief). Additional provisions should also be incorporated for different Martian surface conditions, water input (melt rate and precipitation), and variable ice stability line. Further, the modeled topography is simplified and generalized and is not built from any single river valley found in the DEM and therefore there are no direct comparisons possible. The results of this study do indicate that the longest and most complex Martian valley networks are more consistent with the warm wet climate scenario.

Acknowledgments

This research was supported by the NASA Mars Data Analysis Program (80NSSC18K1476) and by the National Science Foundation Graduate Research Fellowship under Grant No. (DGE 2040434). Landlab and other CSDMS products are supported by the US National Science Foundation (2148762, 2104102).

Open Research

We also acknowledge MOLA team for providing data from MGS (Smith et al., 2001; 2003) (Global MOLA mosaic data download link:

ftp://pdsimage2.wr.usgs.gov/pub/pigpen/mars/mola/mola128_88Nto88S_Simp_clon0.zip) Steckel (2024) Simple_Model.py (version 1), avsteckel/MVNS: MVN (Version v1.0). Zenodo.

https://doi.org/10.5281/ZENODO.14029190

Chapter 3

Expanding Terrestrial Techniques for Mineral Identification

Abstract

Planetary scientists and engineers must test remote sensing instruments on Earth before they can be trusted for use on other planets. Performing remote spectral analysis in Earth analog environments presents unique challenges due to the varying atmospheric compositions across different celestial bodies. Absorption by water vapor in Earth's atmosphere makes spectral bands around 1.4 μm inaccessible for remote sensing by orbital and aerial vehicles, leaving systems designed for these platforms (such as Tetracorder, an open source software package developed by the United States Geological Survey (USGS) for semi-autonomous mineral identification) underdeveloped in this region (Clark et al., 2003). However, planetary bodies such as the Moon or Mars don't have significant water vapor in their atmospheres, and thus the wavelengths around 1.4 μm become available for spectral diagnostics. This study considers a portable hyperspectral imager that can get significantly closer to the target which requires penetrating much less atmosphere than experienced from an aircraft or spacecraft. There are 99 minerals with absorption features around $1.4\mu m$ identified in the Tetracorder spectral library among three groups: 1.3, 1.4, and 1.5μm. Whether the shape and position of spectral features in these groups is unique enough to be used for mineral identification will be explored in section 3.4. While the current catalog is extensive, it is not exhaustive, and remains a subject of ongoing research. I compare features in the $1.3 - 1.5\mu$m range to the broader USGS library of minerals to determine if there is enough data for a unique mineral identification.

This chapter investigates how different thicknesses of a wet Earth atmosphere affect Tetracorder's mineral identification capabilities. By collecting data at various distances from the source, we attempted to quantify the impact of the water absorption band on the capacity, accuracy, and reliability of mineral identification. This study not only tests the limits of current spectral analysis software in identifying minerals within regions of challenging absorption bands but also explores the potential of high-resolution hyperspectral imaging in enhancing the accuracy of geological surveys on planetary surfaces. While these data were taken from a tripod, this imager could also be mounted to a drone or the rover for future use on a planetary surface. In addition, the lightweight and computationally efficient nature of Tetracorder makes it attractive for resource limited exploration missions. Its ability to operate semi-autonomously onboard rovers, processing spectral data without additional human or computational resources, may pave the way for real-time decision-making onboard spacecraft, planetary aerial vehicles, or rovers on future missions (Thompson et al., 2020b; Candela et al., 2017). Ultimately, this research aims to understand how a tool like Tetracorder could be used as a more versatile and robust tool for planetary exploration and what limitations might exist for this expert system.

3.1 Introduction: Signal Transmission through the Atmosphere

Remote sensing spectrometers that operate in the visible and near infrared (VNIR) wavelength range typically rely on spectral absorption features around 1 μm or 2 μm, with a gap in data around 1.4 μm. This gap comes from the atmospheric water absorption band, which drops signal transmission to 0 as shown in Fig. 3.1. However, many minerals have diagnostic spectral features in this band, as illustrated in Fig. 1.1. Spectra in the near infrared (NIR) range are also useful to the agricultural (Cevoli and Fabbri, 2020; Logan et al., 2020), mining (Chevez et al., 2021), and defense (Bárta et al., 2018) industries, which have inspired development of multispectral and hyperspectral imagers on aerial platforms that get within tens of meters of their target, reducing the amount of atmosphere that the signal has to penetrate, and the attenuation by water around 1.4 μm. This study uses a state of the art drone mountable NIR hyperspectral imager provided by

Resonon, the PikaIR, to see if adjusting the distance from the target can be used to expand mineral identification with spectral features around 1.4 μm. This could be useful on Earth and beyond on other planetary surfaces.

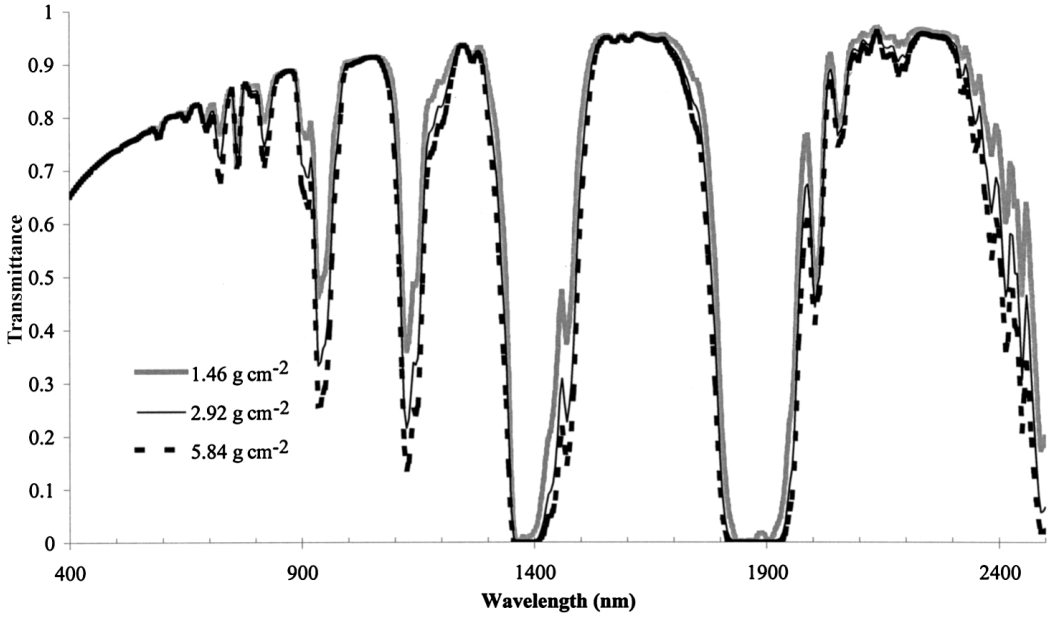

Figure 3.1: Vertical atmospheric transmittance versus wavelength simulated for different water vapor amounts from Fig. 1 of Barducci et al. (2004).

In the NIR (0.9-1.7μm), absorption by water vapor dominates over other processes by the atmosphere such as interaction with other molecules, scattering, or emission (Ptashnik et al., 2015). Thus the amount of light absorbed depends primarily on the amount of water vapor that the signal must penetrate. These assumptions are applied in a simple radiative transport model, illustrated in Fig. 3.2 and by equation 3.1.

$$I = e^{-d\alpha_{wcs}} \tag{3.1}$$

The percent of light transmitted (I) and distance (d) from Fig. 3.2 are related in equation 3.1 by the absorption coefficient, α_{wcs}. α_{wcs} is defined is defined as the inverse of the distance for which the radiation intensity is reduced by $1/e$. This relates to the absorption cross section

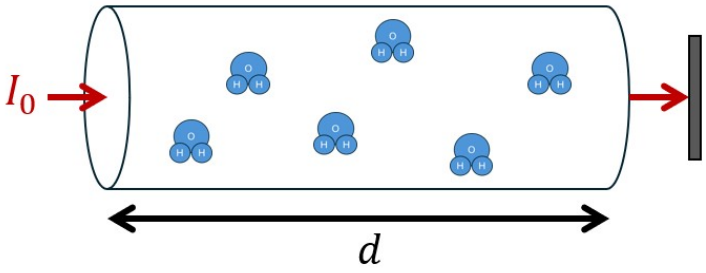

Figure 3.2: Cartoon depiction of light transmission through the atmosphere. I_0 represents the initial light, which will be absorbed by water molecules before it gets to the target and d is the distance the wave travels.

$C_s(\nu, T)$, which is the effective area over which a particle interacts with an incident light beam (not the cross sectional area of the molecule), and is shown in equation 3.2 (Bohren and Clothiaux, 2006; Koroleva et al., 2022). The absorption coefficient is highly sensitive to the number of water molecules in that space, which depends on environmental parameters like the relative humidity (RH), temperature (T), and saturated vapor pressure (v_p) of water (Minkina and Klecha, 2016). These variables can be expressed as the partial pressure of water, $P_{H_2O} = RH \times v_p(T)$. For this study, I will assume that the relative humidity is $\sim 30\%$ and the temperature $\sim 300K$, meaning the $P_{H_2O} = 0.0126ATM$. In equation 3.2, k_B is Boltzmann's constant, $1.380649 \times 10^{-23} J/K$.

$$\alpha_{wcs} = \frac{1}{k_B T} C_s(\nu, T) P_{H_2O}^2 \tag{3.2}$$

The absorption cross section of water vapor, $C_s(\nu, T)$, is provided by Ptashnik et al. (2015) near the 1.4 μm water absorption band as shown in Fig. 3.3. Ptashnik et al. (2015) used the theoretical MT_CKD model developed by Mlawer et al. (2012) which was derived from first-principle molecular interactions and applied perturbative adjustments via a χ-function to ensure agreement with experimental data (Mlawer et al., 2012; Ptashnik et al., 2015). Figure 3.4 shows the estimated fraction of light transmitted versus wavelength at several distances with this model using equations 3.1 and 3.2. Both the width and the depth of the modeled attenuation are affected by the distance between the measurement and the object being measured. Minor effects are observed for 1m distances, which increases to the complete loss of signal at distances over 1km (the estimated

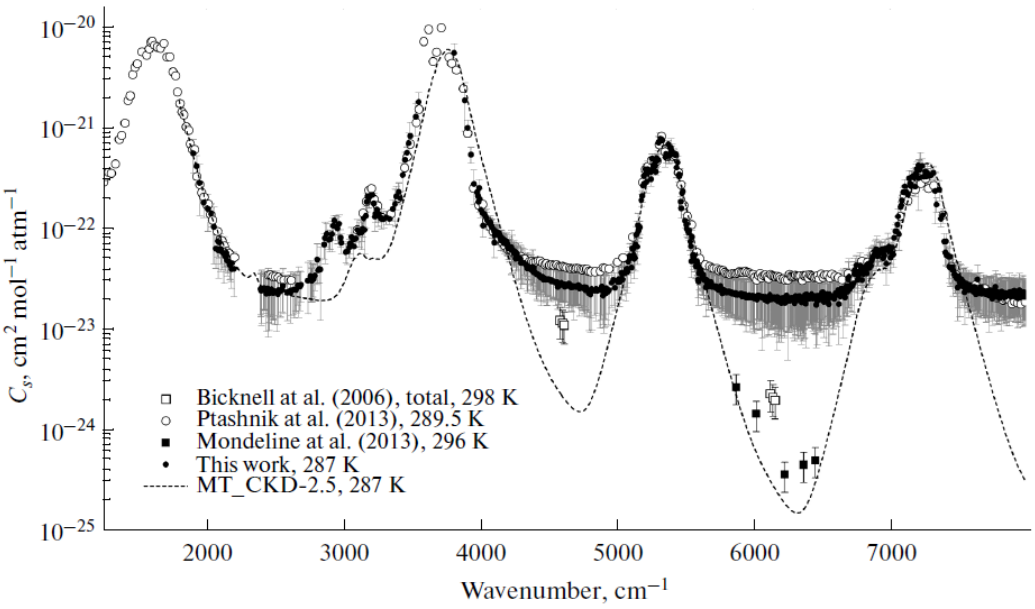

Figure 3.3: Absorption crossection ($C_s(\nu, T)$) as a function of frequency from Fig. 4 of Ptashnik et al. (2015). $C_s(\nu, T)$ is extracted from the Mlawer et al. (2012) semi-emperical MT_CKD model.

minimum and maximum distance of a target). Figure 3.4 shows that at 1.36μm, the transmitted signal drops to just over 2% (at 50m). Between 1.36 and 1.39 μm, the transmitted signal drops below 1% and 1.39μm, the transmitted signal picks up above 1%. Field observations with a spectrometer collecting data at a 50m distance aligned well with the expectations from this preliminary model. Channels between 1.36-1.39 μm were deleted due to low signal levels from the atmospheric attenuation. Data from this field experiment will be discussed further in chapter 4.

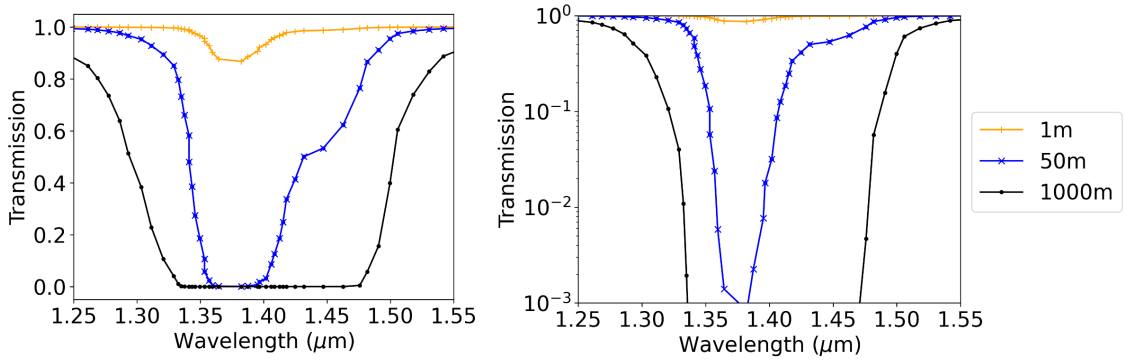

Figure 3.4: Transmission of light through different distances of simulated atmospheres. The atmosphere is assumed to be 30% relative humidity at 300K, which is typical for a day in Utah in October. This is the same plot shown in a linear scale on the left and a log scale on the right to see the details around 1.35-1.40 μm. The yellow line with the '+' symbol indicates a 1m simulated distance, the blue line with a 'x' symbol indicates a 50m simulated distance, and the black line with a '.' symbol indicates a 1000m distance. These are assumed to be approximately the minimum and maximum distances that a hyperspectral imager would target in the field.

These results show that any attempt to collect data in the 1.3-1.5 μm wavelength range will be highly dependent on distance, sensor signal to noise ratio, and environmental conditions. There are many confounding factors not incorporated into this model such as variations in relative humidity, temperature, and atmospheric composition along the light path. Another study by Minkina and Klecha (2016) modeling water absorption in the thermal IR bands showed differences between measured and modeled transmission by up to 10% for distances under a kilometer, and up to 100% for distances over a kilometer, and there may be a similar error in the VNIR bands that has not been quantified.

The complex interaction between EM waves with an atmosphere is an active area of research

(Ptashnik et al., 2015). In an open environment, where the interactions between the target signal and the greater environment are not controlled, measurements at a specific location will be influenced by interference from waves from different directions, as illustrated in Fig. 3.5 (Minkina and Klecha, 2016). Furthermore, diffraction, reflection, absorption, and emission are among the interacting processes which make a closed form (explicit with representative formula) solution for light behavior in this environment elusive. These models do not replicate the exact conditions in the field, which is why using field data collected in a representative environment is so important. Field data will require calibration by a white reference material with a known spectrum which subtracts the wavelength dependent effects of the atmosphere as long as there is signal above the noise threshold of the instrument.

When trying to identify a mineral with VNIR data, spectroscopists first narrow down possible options by focusing on diagnostic absorption features from the spectrum. It is convenient to group these features by wavelength as described by Fig. 1.1. Tetracorder is a spectral feature-based identification algorithm developed by researchers at the United States Geological Survey (USGS) to address the challenges of mineral identification and mapping using hyper- or multi-spectral data (Clark et al., 2003). The algorithm is designed to mimic the approach used by human spectroscopists, focusing on diagnostic absorption features rather than attempting to match the entire spectrum (Bishop et al., 2019). By isolating these key spectral features, Tetracorder can identify materials even when their spectra are partially obscured or mixed with other components (Clark et al., 2003). Tetracorder is a lightweight software designed to run onboard computers with limited performance, such as onboard a drone or rover, and has an expert system which can deliver spatially resolved mineral identification results nearly instantaneously (Steckel et al., 2024a; Noe Dobrea et al., 2023; Steckel et al., 2023; Thompson et al., 2020b; Candela et al., 2017). This expert system was designed for use with the AVIRIS (airborne visible / infrared imaging spectrometer) and EMIT (Earth surface mineral dust source investigation) missions, and is tested in this work for use with a portable spectrometer.

Tetracorder was designed for spectrometers using the full VNIR (0.35-2.5 μm) range, and

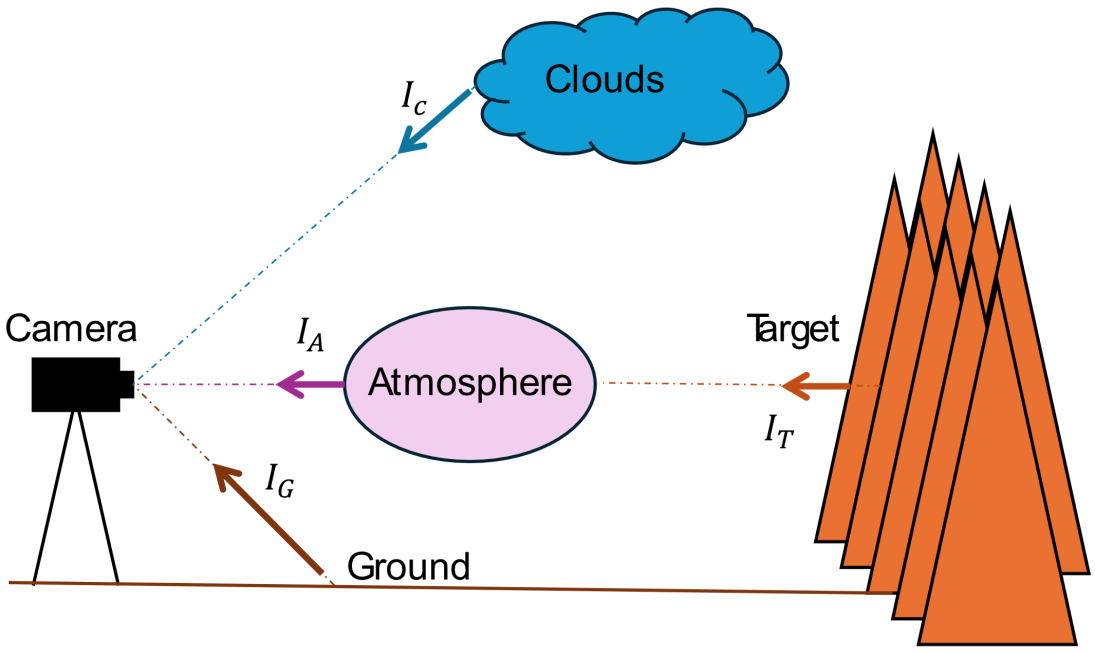

Figure 3.5: Sources of interference from the environment while collecting data of a target. A simplified model is developed to consider the signal from the atmosphere, I_A, in the cartoon and how it will attenuate the signal from the target, I_T from absorption by water vapor molecules in the atmosphere. In reality, many other sources of EM waves exist in the scene, which will also interfere with these signals. A more complex radiative transport model would be required to include these sources to quantitatively predict the attenuation over these wavelengths, as described in Minkina and Klecha (2016).

changes will be required to adapt to the NIR spectral range of the PikaIR (0.9-1.7 μm). Although Fig. 3.4 shows that operating at $\sim$50m should result in some signal transmission between 1.3-1.5 μm, the Tetracorder expert system was not designed to identify features in this range, or work without features around 1μm and 2μm. I upgraded the Tetracorder expert system to account for the new spectral features in this range, and remove features outside the range of the PikaIR. Each mineral identified automatically was then manually compared against library spectra to confirm its identification. This required development of new python software to compare the feature(s) identified by Tetracorder with library reference minerals, which will be described in section 3.2. This chapter uses datacubes from chapter 4 which identified minerals in cliffs 40-60m from the imager to see if new spectral data in the 1.3-1.5 μm band can be used to identify minerals via remote sensing.

3.2 Methods

The first step in the Tetracorder data analysis process is the removal of the background continuum. Spectra collected from the natural environment will have large scale variations that are not due to interactions with the crystalline structure and are instead caused by other properties, such as surface roughness, grain size, temperature, scattering, or instrument noise. The continuum is a piece-wise continuous function that envelopes the measured spectrum. The continuum follows the highest points along the spectrum, creating an envelope using the convex hull method, as shown in the top plot of Fig. 3.6 (Bishop et al., 2019; Clark et al., 2003; Clark and Roush, 1984). The spectrum is divided by the continuum to produce a normalized spectral signal, $L^{Norm}(\lambda)$ as a function of wavelength (λ), shown in the bottom plot of Fig. 3.6. This isolates individual absorption features that will be used for mineral identification.

The same continuum removal process is also performed on each reference spectra, enabling a direct, normalized, comparison of absorption features. Next, the minimum reflectance (R_b) is identified, and that frequency is located. The reflectance value of the continuum curve at the same

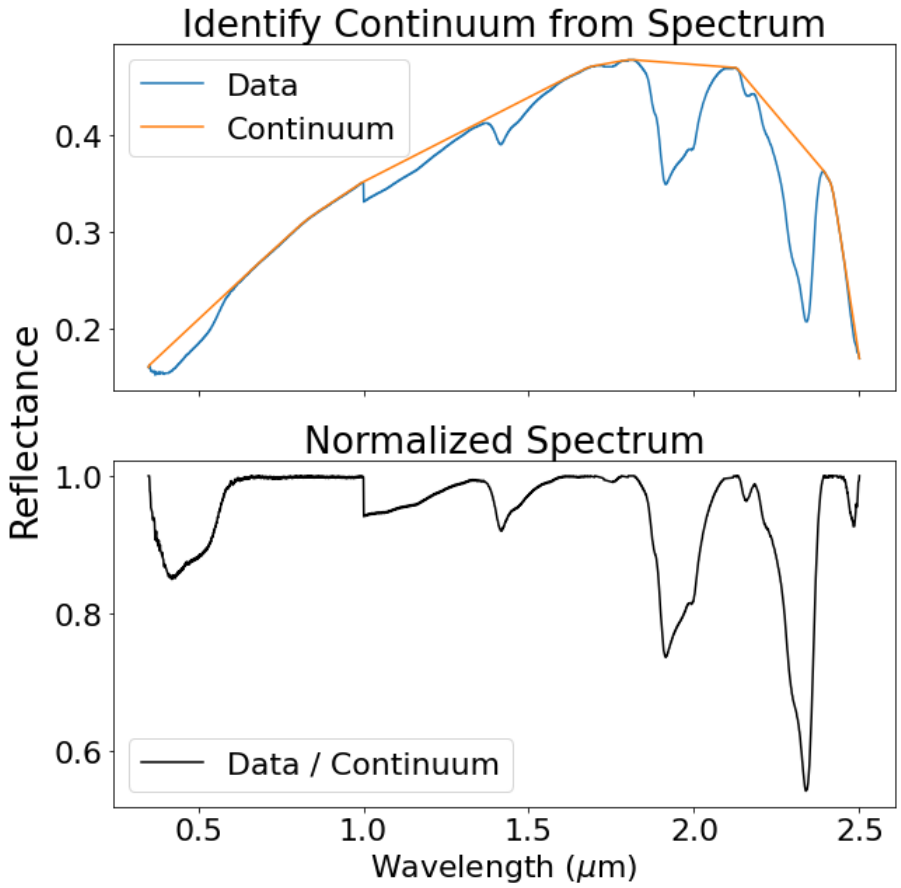

Figure 3.6: Removing the background continuum from an example spectrum. The orange line (continuum) envelopes the maximum points of the spectrum (blue). The spectrum is normalized by the continuum to remove background effects from the environment and isolate the absorption feature (Thompson et al., 2020b; Bishop et al., 2019; Clark et al., 2003; Clark and Roush, 1984). The spectrum was collected from an ASD spectrometer and will be referenced in section 3.3.2 in Fig. 3.10.

frequency (R_c) is also identified to compute the feature depth by the following equation:

$$D = \frac{R_c - R_b}{R_c}, \tag{3.3}$$

where R_c is the continuum depth and R_b is the signal depth (Bishop et al., 2019; Clark et al., 2003; Clark and Roush, 1984). A stronger feature means the depth D is larger. Even after normalization, variations in measurement conditions and changes in lighting will affect the strength of the signal, and require scaling the reference data. If the reflectance as a function of wavelength for the library spectra is $L_{SL}(\lambda)$, the scalar value k is selected to best match the observed spectrum L_{OB}, as shown in equation 3.4 (Bishop et al., 2019; Clark et al., 2003; Clark and Roush, 1984).

$$L_{SL}^{Scaled} = \frac{L_{SL} + k}{1 + k} \tag{3.4}$$

A modified least squares technique is used to select a k value that minimizes the fit parameter r, shown in equation 3.5. Tetracorder conducts a survey of all library spectra and calculates the goodness of fit for the observed feature. Tetracorder's output includes text files and datacubes showing the fit, depth, and fit*depth match of each pixel to a library spectrum (Bishop et al., 2019; Clark et al., 2003; Clark and Roush, 1984).

$$r = \Sigma_\lambda (L_{SC}^{Scaled} - L_{OB})^2 \tag{3.5}$$

3.2.1 Modifications to Tetracorder

Working in the NIR spectral range of the PikaIR instrument (0.9-1.7 μm) requires changes to the Tetracorder expert system which was designed for the full VNIR (0.35-2.5 μm) range. The latest release of Tetracorder (5.27e) incorperated spline fits in addition to existing linear fits for absorption feature identification. These spline features were implemented to improve the accuracy of spectral fits (especially for broad features), but since they require 4 segments of the feature to be available, they do not fit within this reduced spectral range, and with the deleted channels between 1.36-1.39μm (Clark et al., (2024) in press). Therefore, for all of the features in the 1.3,

1.4, and 1.5μm groups, I changed the features from spline to linear and edited them to be within the PikaIR's range of $0.9 - 1.7\mu m$ where possible. I also removed any required features that were outside of that range, for instance the 2.2 and 2.5μm features for muscovite in Fig. 1.1.

3.2.2 Manual Mineral Identification

The PikaIR datacube, $\mathbf{P}$, is an array of matrices representing an image with spectra at each pixel. For example, in $\mathbf{P}$ at 1.06μm, $s_{11} = 0.100$ is the absorption value at $\mathbf{P}(\lambda = \mathbf{1.06}\mu\mathbf{m})$ for the top left most pixel in the image. At this wavelength, the full image is represented by:

$$\mathbf{P}(\lambda = \mathbf{1.06}\mu\mathbf{m}) = \begin{bmatrix} s_{11} & s_{12} & s_{13} & \dots & s_{1c} \\ s_{21} & s_{22} & s_{23} & \dots & s_{2c} \\ \vdots & \vdots & \vdots & \ddots & \vdots \\ s_{r1} & s_{r2} & s_{r3} & \dots & s_{rc} \end{bmatrix} = \begin{bmatrix} 0.100 & 0.098 & 0.106 & \dots & 0.009 \\ 0.097 & 0.095 & 0.102 & \dots & 0.009 \\ \vdots & \vdots & \vdots & \ddots & \vdots \\ 0.034 & 0.034 & 0.064 & \dots & 0.015 \end{bmatrix} \tag{3.6}$$

This datacube is input into Tetracorder. For each mineral checked, Tetracorder outputs 3 datacubes: one for the fit values (a polynomial fit of the feature to the reference spectra, see Clark et al. (2003)), one for the depth values, and one for the fit x depth values for each pixel. Fit x depth values (fd) capture both parameters and are typically the best fit for the mineral. Below is an example matrix $\mathbf{M_{34}}$ which is for mineral number 34 and contains an interger from 0-255 representing the (fd) value for each pixel. Tetracorder also provides .gif files to review this data visually.

$$M_{34}(fd) = \begin{bmatrix} 0 & 0 & 56 & \dots & 0 \\ 0 & 38 & 41 & \dots & 0 \\ \vdots & \vdots & \vdots & \ddots & \vdots \\ 45 & 61 & 124 & \dots & 0 \end{bmatrix} \tag{3.7}$$

$\mathbf{M_{34}}$ is transformed into a new binary matrix $\mathbf{B_{34}}$ using a threshold value, set to 10 in this example. $\mathbf{B_{34}}$ is set to 1 if above the threshold, and 0 for anything below the threshold. However, this threshold value could be increased based on reviewing the results.notzero.cluster file to remove the

lower quality identifications, or decreased if more resolution is needed.

$$B_{34} = \begin{bmatrix} 0 & 0 & 1 & \dots & 0 \\ 0 & 1 & 1 & \dots & 0 \\ \vdots & \vdots & \vdots & \ddots & \vdots \\ 1 & 1 & 1 & \dots & 0 \end{bmatrix} \tag{3.8}$$

$\mathbf{B_{34}}$ is used to collect all spectra for mineral 34 into one matrix, $\mathbf{C_{34}}$. The spectra from all pixels can be averaged to create the average spectra for mineral 34, $\overrightarrow{c_{34}}$.

$$C_{34}(\lambda_{1.06}) = P(\lambda_{1.06}) \times B_{34} = \begin{bmatrix} 0 & 0 & 0.106 & \dots & 0 \\ 0 & 0.095 & 0.102 & \dots & 0 \\ \vdots & \vdots & \vdots & \ddots & \vdots \\ 0.034 & 0.034 & 0.064 & \dots & 0 \end{bmatrix} \overrightarrow{c_{34}(\lambda)} = [\overline{C_{34}(\lambda_{1.06})}, \overline{C_{34}(\lambda_{1.07})}, \dots] = [0.36, 0.23, 0.18$$

(3.9)

Next, we manually remove the background continua, as shown in Fig. 3.6. $c_{34}^{\rightarrow}$ is the data plotted in Fig. 3.6.

The same process is applied to library minerals, which have been interpolated to match the same wavelengths as the PikaIR instrument. The final stage of the analysis is to minimize the least squared error between the spectrum and each library mineral. To assess the quality of the match, the fit parameter r from equation 3.5 was minimized.

3.3 Results

The methods described in section 3.2 were applied to field data from the PikaIR spectrometer. To evaluate the results, Tetracorder puts the minerals into spectral groups based on their diagnostic features. This is a convenient way to manage the review of 1,100+ minerals from the library, and this study will discuss results from the 1μm, 1.3 μm, 1.4 μm, 1.5 μm, and 2μm groups, which are all currently available in Tetracorder. Since this is the first time the 1.3, 1.4, and 1.5 μm groups are being used independantly, the feature diversity of minerals in this range is evaluated.

3.3.1 Mineral Absorption Features around 1.4 μm

Mineral identification in a field environment using exclusivley HSI data from features around the 1.4 μm water absorption band was attempted in this study. Of the 99 minerals considered, the 1.3 μm group has 34, the 1.4 μm group has 49, and the 1.5 μm group has 16 minerals as listed in Table 3.1. Figure 3.7 evaluates the feature diversity of the minerals from these groups in Tetracorder. This shows how features can be differentiated by different central wavelengths or widths. Datapoints that do not overlap have unique spectral features that can be used for identification. Where data points overlap, more information is required. For figure legibility, note that most minerals are grouped together (such as antigorite and chrysotile listed as a serpentine), and some minerals are mixtures. Therefore two data points refer to different phases, compositions, or mixtures of minerals of that type, not two different features in the same spectrum. Some features that have similar central wavelengths and widths, such as the doublet around 1.4 μm in kaolinite, have unique spectral shapes which makes different mineral phases (such as halloysite) or mixtures distinguishable by the polynomial shape fitting algorithum used in Tetracorder (Pineau et al., 2022; Clark et al., 2003). However, some features such as those in the serpentine group (e.g. antigorite vs. chrysotile vs. serpentine) have a single feature with a similar shape and width may not be unique enough for a definitive identification. Adding features from the broader VNIR range would greatly improve the ability to differentiate between these minerals.

Future projects could add minerals to this picture, to ensure all minerals with features at this wavelength were interrogated. Implementing these mineral groups in Tetracorder would require validation of every overlapping point to ensure the shapes can be differentiated, which is outside the scope of this study. Furthermore, skewness or kurtosis could be added to the polynomial fit to improve on the shape matching algorithum. Comparing these methods was discussed in Rencz and Ryerson (1999) and Clark et al. (2003) which found the polynomial fit to generally be more accurate in the VNIR range, but was not addressed for these features in this narrow spectral range.

Table 3.1: Mineral List

1.3 μm	1.4 μm	1.5 μm
phyllo-ksg-chrysotile	phyllo-nacrite, phyllo-cookeite	hydroxide-gibbsite
phyllo-ksg-dickite	nesosil-topaz, tectosil-opal	zeolite-natrolite
amphibole-richterite	mica-paragonite	sulfate-bloedite
phyllo-ksg-nacrite	phyllo-lepidolite	sulfate-jarosite-k
phyllo-chlorite	smectite-sauconite	nesisil-datolite
phyllo-ksg-endellite	kaolgrp-halloysite	sulfate-jarosite-k
amphibole-tremolite	mica-margarite	sulfate-jarosite-na90c
phyllo-ksg-lizardite	mica-muscovite	sulfate-jarosite-na200c
smectite-saponite	phyllo-chrysocolla	phyllo-prehnite
phyllo-serpentine	smectite-montmor-swy	vegetation.dry+green
phyllo-talc	kaolgrp-kaolinite-pxl	vegetation1
phyllo-pyrophyllite	nesosil-hydrogross	water.red.algae
phyllo-ksg-antigorite	smectite-hectorite	water+mont0.5gpl
amphibole-actinolite	mica-roscoelite	water+mont1.67gpl
amphibole-uralite	smectite-montmor-saz	water+mont5.01gpl
mica-phlogopite	phyllo-palygorsk	water+mont16.5gpl
phyllo-kaolinite-wxl	mica_muscovite	
amphibole-smaragdit	zeolite_mordonite	
phyllo-clinochlore	zeolite-clinpt, zeolite-stilbite	
phyllo-chlorgrp-cookeite	zeolite-heuland	
mica-lepidolite	scapolute-meionite	
silica-opal	smectite-nontronite	
mica-paragonite	zeolite-analcime	
mica-lepidolite	scapolite-mizzonite	
kao.5+musc.medhiAl	sulfate-alunite	
phyllo-kaolinite-pxl	sodalite-lazurite	
phyllo-vermiculite	cyclosil-elbaite	
vegetation.dry+green	zeolite-laumontite	
vegetation1	phyllo-vermiculite	
water+mont0.5gpl	tourmaline, sulfate-eugsterite	
water+mont1.67gpl	sulfate-alunite-na	
water+mont16.5gpl	zeolite-scolecite	
water+mont5.01gpl	sulfate-gypsum	
water.red.algae	sulfate-schwertm	
	sulfate-copiapite	
	hydroxide-gibbsite	
	zeolite-natrolite	
	kaolin.5+muscov.medhighAl	
	vegetation.dry+green	
	vegetation1, water.red.algae	
	water+mont0.5gpl	
	water+mont1.67gpl	
	water+mont5.01gpl	
	water+mont16.5gpl	

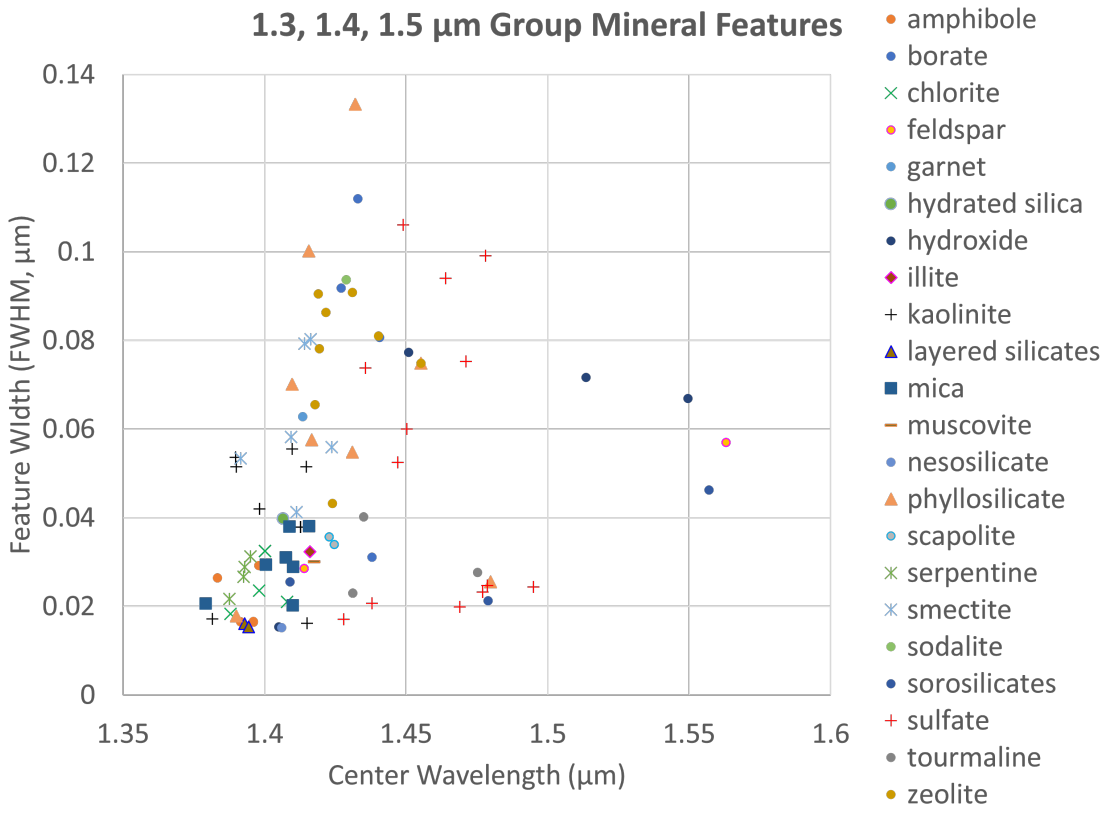

Figure 3.7: Minerals with absorption features around 1.3, 1.4, and 1.5 μm are plotted with their central wavelength on the x-axis and the width of a gaussian fit to their feature at full width half maximum (FWHM) on the y-axis. Locations where points do not overlap are likely useful for unique mineral identifications. Locations with overlapping data points would need to have unique spectral shapes or would rely on additional features from other parts of the spectrum to make a unique mineral identification. Spectra from all minerals comes from the United States Geological Survey (USGS) (Kokaly et al., 2017). Note that multiple data points from the same mineral group represent different compositions.

3.3.2 Comparison with Traditional Mineral Identification Techniques

Data from seperate field work in Yellow Cat, Utah were used to test the techniques described in section 3.2. This location was selected primarily for its lack of vegetation and natural setting (e.g., not on a man-made road, near a mining entrance, or a mining ventilation shaft) as seen from photos of the area in Fig. 3.8. Three spectrometers and two imagers were used to identify minerals in this area including a contact VNIR, contact FTIR, micro imager, mast-mounted VNIR and mast-mounted color camera as described in Noe Dobrea et al. (2023). Fig. 3.9 shows the data collection setup, with the location of mast mounted instruments relative to the sampling location, where contact instruments and the microimager collected data. The micro imager collects color images at 20 μm per pixel of the spot targeted by contact spectrometers. The location measured by the microimager and contact spectrometers in this study is pictured on the right of Fig. 3.8. This area appears to contain a mixture with several minerals of different grain sizes.

The mineral mixture in Fig. 3.8 was measured by a contact VNIR probe which collected data in an approximately 1cm spot. This spectra was automatically processed using Tetracorder and was found to have a mixture of siderite (Fe^{2+} generic carbonate) and calcite as shown in Fig. 3.10 Noe Dobrea et al. (2023). Siderite is another carbonate similar to calcite but with a smaller cell (since Fe^{2+} has a smaller ionic radius then the Ca^{2+} in calcite) found in sedimentary rocks (Deer et al., 2013). The contact VNIR spectra is plotted in Fig. 3.10 alongside both siderite and calcite library minerals. These are calibrated, unprocessed spectra (continua removal and scaling described in section 3.2 has not been added), but the absorption features generally align.

A contact FTIR, pictured in Fig. 3.9 collected data in an approximately 3cm spot in the same area as Fig. 3.8. This spectra was automatically processed using Tetracorder and also found calcite. Measurements from the FTIR are plotted with the library spectrum for calcite in Fig. 3.11. It is clear that this spectra is likely measuring features from other minerals in addition to calcite, but they were not identified by Tetracorder. This is likely due to the relatively smaller library minerals in the mid infrared (MIR), since most of Tetracorder's development focused on smaller

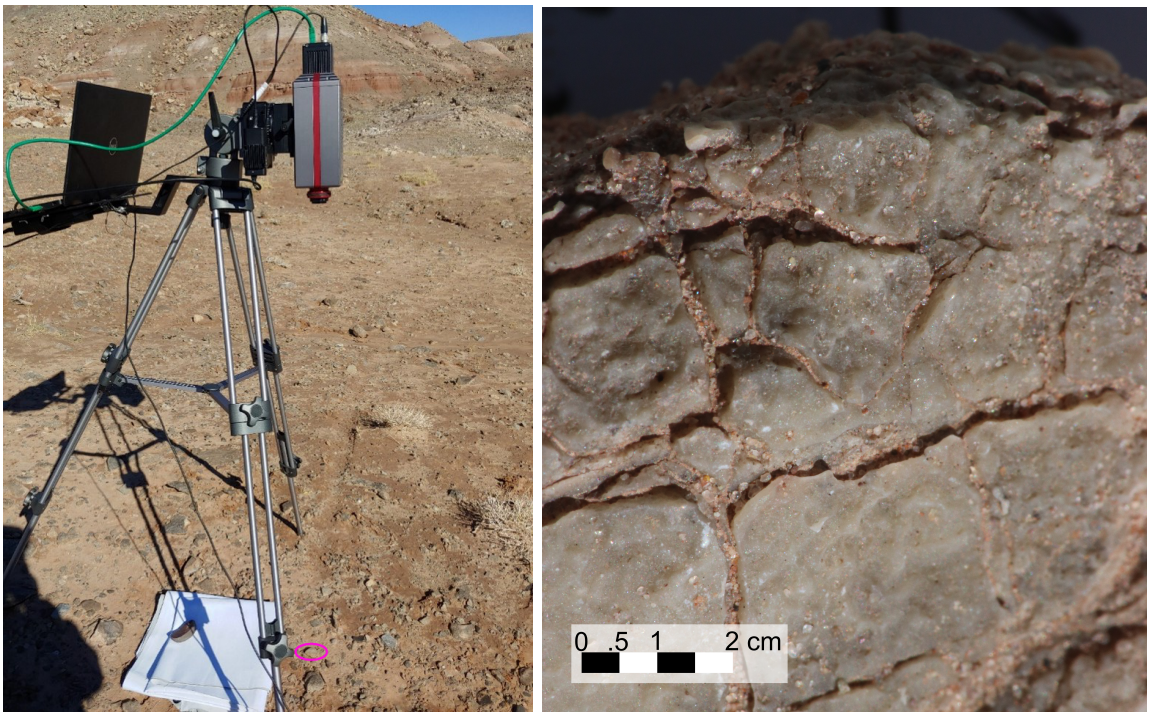

Figure 3.8: Left: PikaIR camera setup with the target rock measured by the VNIR and FTIR contact probes circled in pink. Right: micro imager photo from target rock which shows a mixture of materials of different sizes, colors, textures, and lusters.

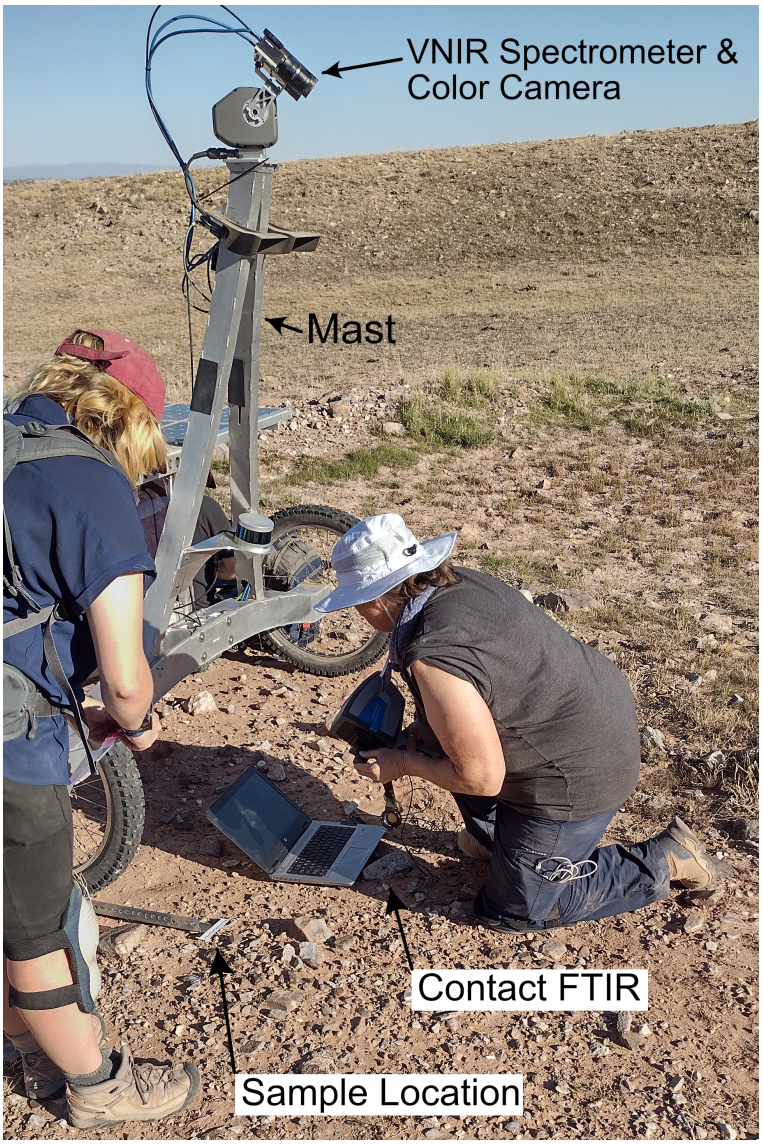

Figure 3.9: Data is collected with both mast mounted and contact instruments as shown in the photo. The mast is approximately 2m from the ground and rotates to collect color images and line spectra in three directions: -30^o (left), 0^o (center), and 30^o (right). The spacer in front of the wheel was used as an indicator to select the area for contact spectral measurements, high resolution micro images, and samples. This was part of a broader field study described in Noe Dobrea et al. (2023). Pictured in photo: Melissa Lane with contact FTIR and Amanda Steckel.

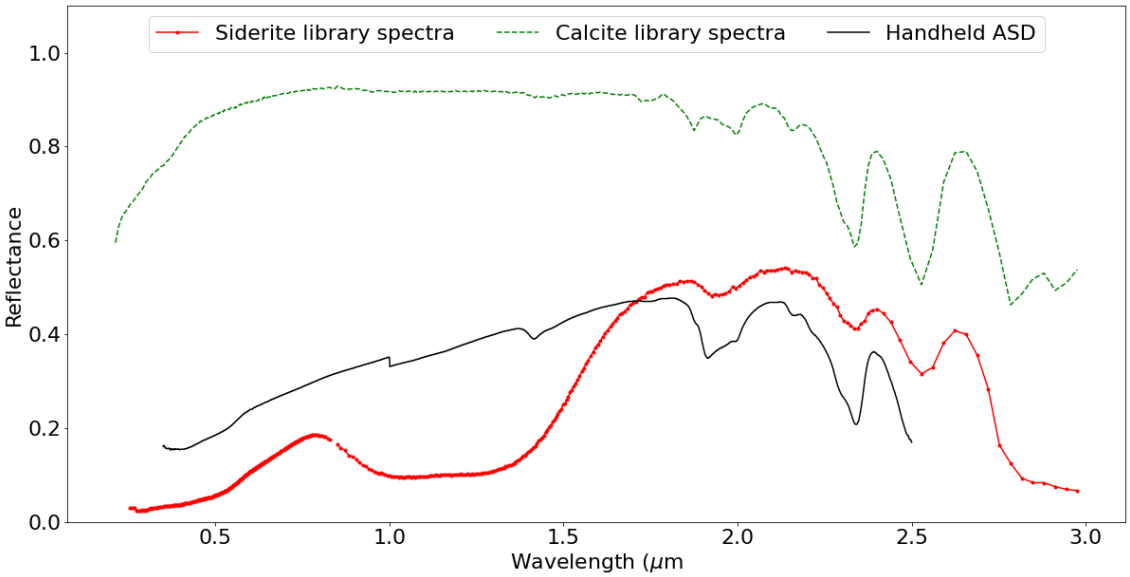

Figure 3.10: The contact VNIR spectrum was collected and analyzed by collaborators in Noe Dobrea et al. (2023). The measurement is shown in black labeled by the instrument, Handheld ASD. A mixture of siderite (red dotted line) and calcite (dashed green line) are from the USGS library and were identified by Tetracorder (Kokaly et al., 2017).

wavelengths in the VNIR. Additional work could be done adding to the number of MIR minerals in the USGS spectral library, or with different measurements of this sample collected in a laboratory such as x-ray diffraction (XRD), to determine the source of those features.

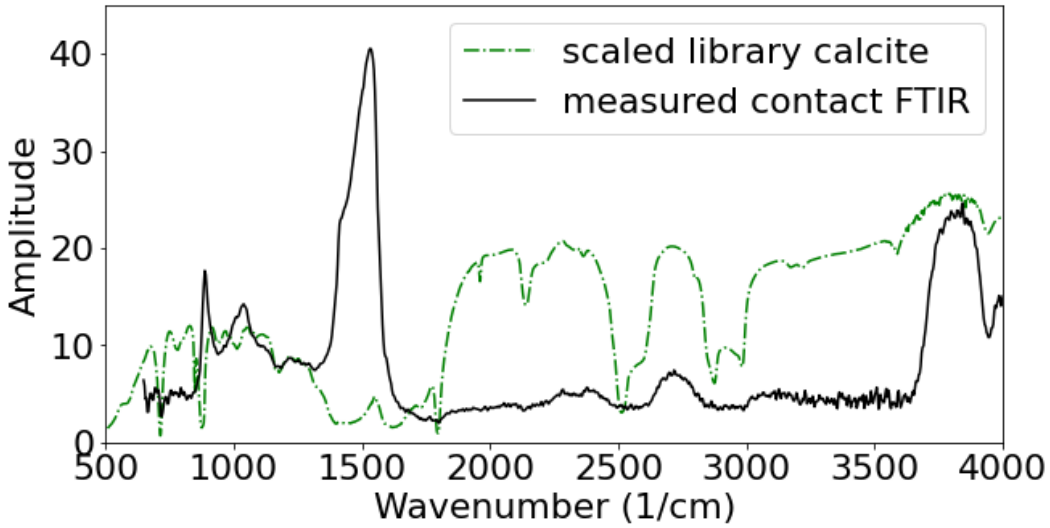

Figure 3.11: Contact FTIR Measurements: data collected and analyzed by collaborators in Noe Dobrea et al. (2023). Spectrum from instrument plotted in black solid line. Instrument was calibrated with white reference before collecting data. Spectrum processed by Tetracorder and identified calcite. Spectrum of calcite (dashed green) from the USGS library was in units of reflectance (0-1) (Kokaly et al., 2017) and has been scaled for visibility on this plot.

Cameras on a 2m mast (shown in Fig. 3.9 were used to measure the area around this rock for context. This mast rotates to collect a line spectra from three directions, and color images were also taken in the same locations for reference and are shown in Fig. 3.14. Spectra are plotted in Fig. 3.12, and were processed by tetracorder to identify minerals. Nano-phase hematite was found in the $1\mu m$ group based on iron absorption features at 0.55μm and 0.88μm. Zooming in on the 0.55μm feature, once the continuum is removed and the rover data are scaled (described in section 3.2), Fig. 3.13 shows how these features align. Hematite is a common alteration product of siderite, and is likely responsible for many of the red hues in this field site such as the red grains in Fig. 3.8. In the 2μm group, a 50% calcite mixed with a 50% Ca – montmorillonite mixture was also found based on the features at 1.91, 2, 2.215, 2.3, and 2.345 μm. Similarly, the contact FTIR also

found calcite. A code snippet from the Tetracorder expert system is provided in appendix D to show which features are used to identify this calcite – montmorillonite mixture.

The PikaIR was setup to collect data approximately one meter from the same target rock as shown in Fig. 3.8, and the white canvas was included in the area of the scan for reference. The datacube collected (represented by $\mathbf{P}$ in equation 3.6) was processed by Tetracorder which creates a matrix of the resulting fit $\times$ depth value for each mineral, $\mathbf{M_{34}}$ from equation 3.7. I converted this into a binary matrix, $\mathbf{B_{34}}$, which is pictured in Fig. 3.15 for the target rock (cropped to the region measured by other contact instruments). Each color in this image represents a different identified mineral (white indicates no mineral identified), with a color image of the target rock shown for reference. Results from the 1.3 and 1.4 μm groups are shown, and no minerals were identified in the 1.5 μm group. The legend shows the mineral identities found by Tetracorder. Spectra from each color are grouped together and averaged into spectra from equation 3.9. That average is then processed in python to manually verify the mineral identification. For example, the red pixels in the 1.4 μm group from Fig. 3.15 were averaged and had continua removed to produce the blue dotted line shown in Fig. 3.16. In this spectrum, Tetracorder identified alunite, which is plotted in Fig. 3.16. This is an example of an incorrect Tetracorder identification, likely due to alunite's doublet between $1.45 - 1.5\mu$m. This relatively wide and deep feature was an easy shape for noisy data to erroneously fit.

Results from section 3.2.2's manual identification process for this same spectra are shown in Fig. 3.15. Opal, chert, and muscovite were found to have the lowest r values (from equation 3.5) with muscovite being the best fit. However, muscovite was not identified by other instruments. There are two possible reasons for this discrepancy: 1) As shown in Fig. 3.8, this rock is made up of many different minerals that include muscovite (perhaps in a fine dust), and was overpowered by other spectral signatures, missed by the contact probes, or deposited by wind after the other spectrometers collected their samples but prior to the PikaIR measurement. 2) Muscovite was not present, and the spectrum was misidentified. If case 2 is correct, it is likely that montmorillonite (measured in the area by the mast-mounted VNIR) was mistaken for muscovite. Montmorillonite

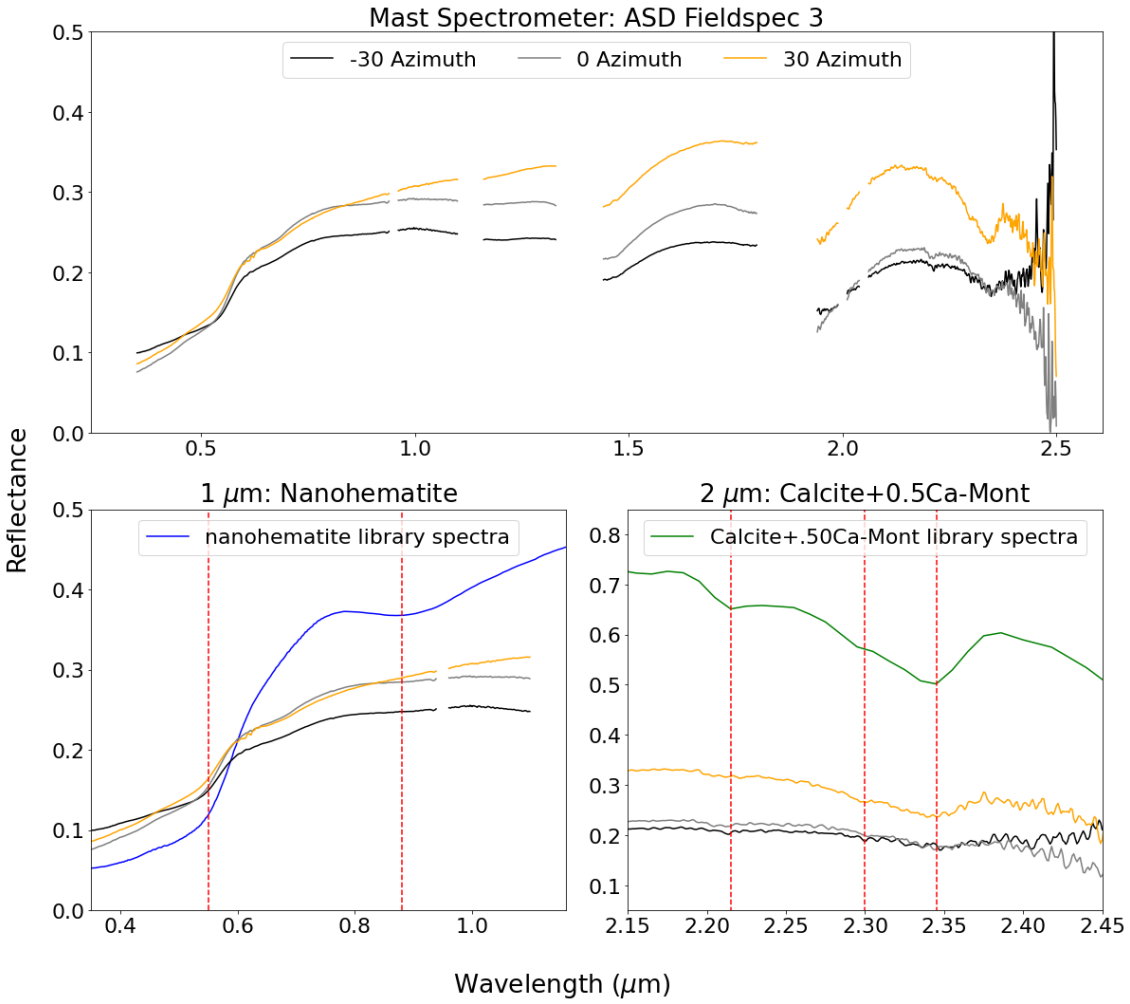

Figure 3.12: Mast-mounted VNIR spectrum collected in three different directions: -30^o (left), 0^o (center), and 30^o (right), as shown in Fig. 3.9. The red dashed lines indicate the center of absorption band features that Tetracorder used for mineral identification. Nanohematite and calcite+.5Ca-Montmorilionite minerals are from the USGS spectral library (Kokaly et al., 2017). Calibrated spectra are unprocessed, meaning continua removal and scaling is not shown here. A detail view of the feature Tetracorder matched at 0.55μm is in Fig. 3.13.

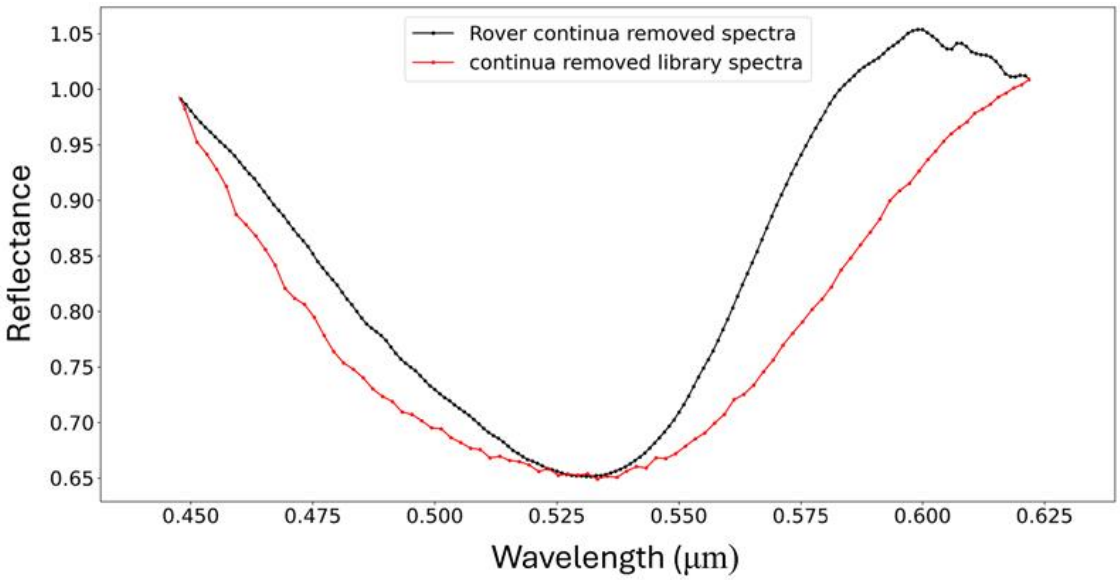

Figure 3.13: Nanohematite Feature: The black spectrum is from the rover's VNIR instrument in the 0^o (center) direction. The red spectrum is from the nanohematite br93 sample in the USGS spectral library (Kokaly et al., 2017). The continuum has already been removed from both spectra. The rover spectra was scaled to match the feature depth of the nanohematite following processes described in section 3.2, which is why some of the data goes above 1.

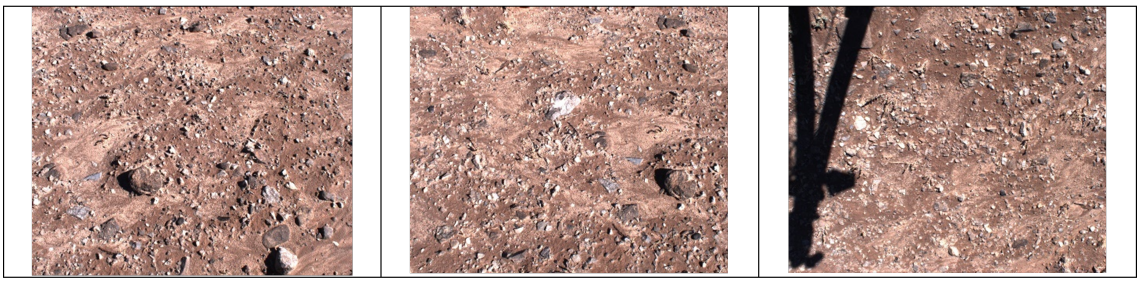

Figure 3.14: Mast-mounted color images collected in three different directions: -30^o (left), 0^o (center), and 30^o (right) azimuth angles, alongside spectrum from Fig. **??**. These are used for context as this spectrometer is measuring a larger spatial footprint consisting of mixed minerals and grain sizes (clay/silt to pebbles).

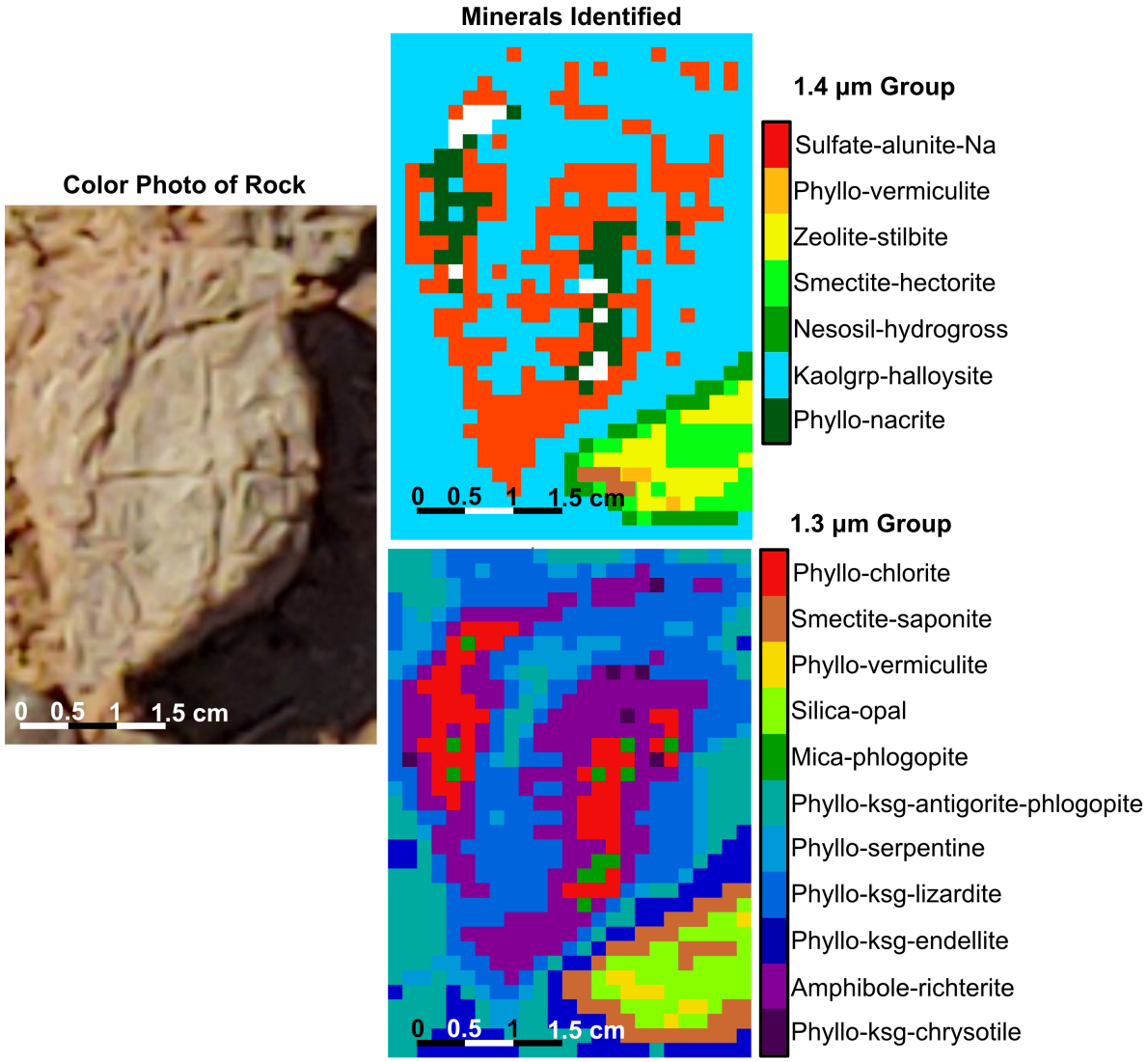

Figure 3.15: Minerals automatically identified by Tetracorder in rock. This is not the final identification and needs to undergo the process in section 3.2.2. White pixels represent no mineral identified at that location. Group 1.3 and 1.4 μm refer to the minerals listed in table 3.1. No minerals were found from the 1.5 μm group. The color photo of the rock is included for reference. The data collection setup and a high resolution micro imager photo from this rock are in Fig. 3.8.

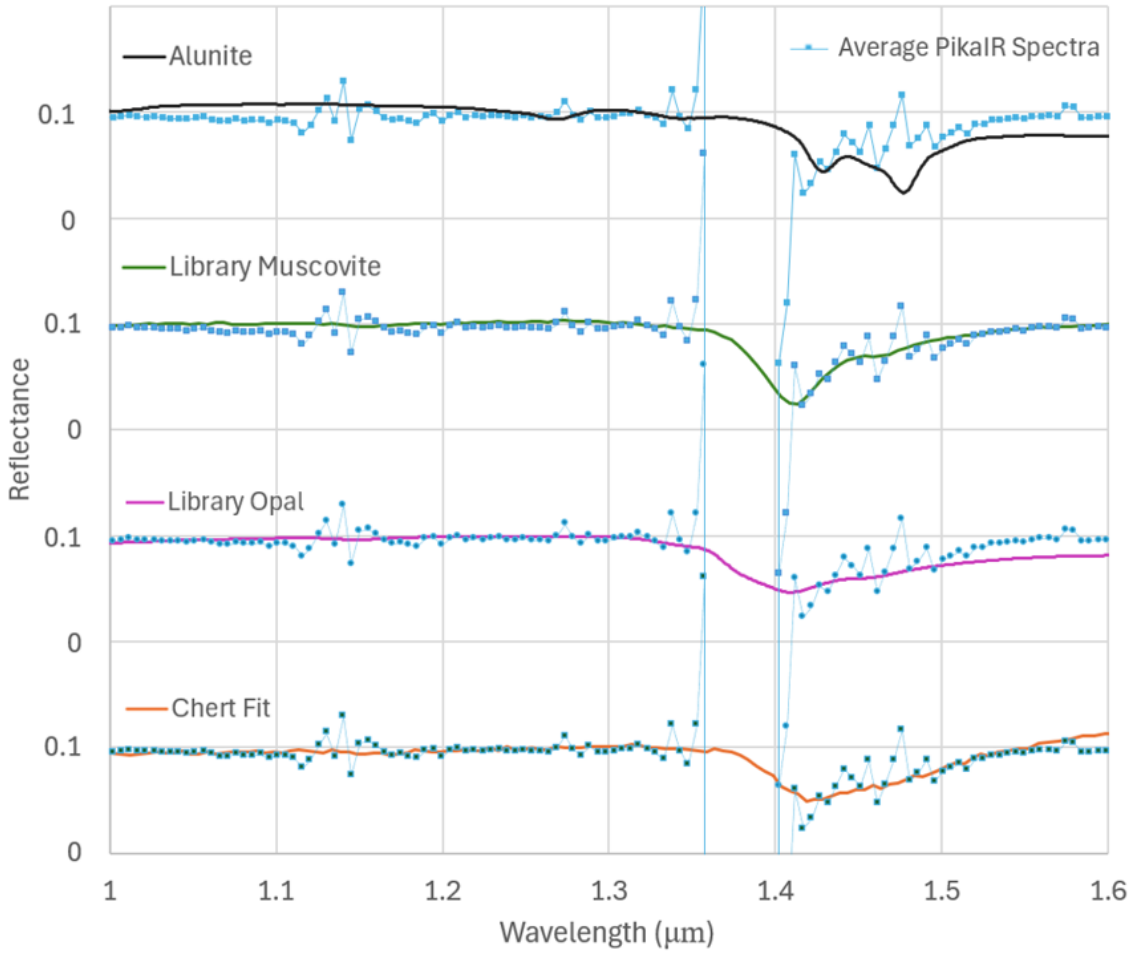

Figure 3.16: Average spectrum from red pixels in the 1.4μm results in Fig. 3.15 is plotted in blue dotted line. Three library minerals are plotted in solid colors and are vertically offset for clarity. The top mineral, muscovite, is the best fit in this example. Tetracorder originally matched this to alunite, likely because of the two absorption features around 1.45 and 1.5 μm, but detailed inspection of the feature shows a better fit to muscovite. Library mineral spectra are from the USGS library in Kokaly et al. (2017).

has a very similar broad, stepped feature between $1.35 - 1.5\mu$m and looks similar to the particular muscovite sample matched from the USGS library spectrum. When this muscovite is mixed with other spectra in the sub pixel scale, the shape of the feature may be too similar to muscovite and impossible for this method to differentiate between. It is important to note that the carbonate and calcite found do not have features in the PikaIR's limited wavelength range, which make them impossible to identify using this method. Regardless, the PikaIR data indicates the likely presence of a clay mineral with this dip from $1.4 - 1.5\mu$m, but more information from another instrument would be required to determine the exact type of clay.

Cross-referencing different instruments on the same sample enables a direct comparison of how the different spectral ranges and spatial resolutions affect mineral identification of the same sample. Table 3.2 is a summary of the identified minerals from each instrument. Hematite, calcite/-carbonates and montmorillionite are all minerals commonly found in sedimentary environments. Sometimes referred to as secondary minerals, they are produced from some kind of alteration process, typically requiring water, increased temperature and/or pressure, which could be valuable insight if part of a broader Earth or planetary study.

Table 3.2: Cross Instrument Mineral Identification Summary: This table summarizes the minerals identified from each instrument. Data from the contact VNIR, mast VNIR, and contact FTIR are provided by Noe Dobrea et al. (2023).

Instrument	Minerals
PikaIR HSI	phyllosilicate group minerals (clays), possibly muscovite
Contact VNIR Probe	siderite, calcite
Mast VNIR	nanohematite, calcite, calcite-montmorillinite mixture
Contact FTIR	calcite

3.4 Conclusion

This work demonstrates the potential for mineral identification using NIR spectral measurements over small distances in an ambient Earth environment. The PikaIR was able to successfully

detect signal through 1m of atmosphere around the 1.4μm water absorption band. Tetracorder, which is currently part of the data processing chain for several NASA missions including AVIRIS, EMIT, and TREX, was used to map minerals from the PikaIR data in Fig. 3.15 (Green et al., 2023; Thompson et al., 2020a; Swayze et al., 2002). These minerals were compared with results from a contact VNIR probe and contact FTIR probe of the same sample. In addition, measurements from a mast mounted line spectrometer of the same area were also taken for comparison.

This project revealed the limitations of using Tetracorder in the NIR, since the minerals in Fig. 3.15 were not consistent with other measurements of the sample, and some (such as zeolite) are not possibly present in this setting. To address this, a novel process was developed in python to identify minerals using the USGS spectral library (Kokaly et al., 2017). The successful detection of a clay mineral from a $1.4 - 1.5\mu$m absorption feature highlights the feasibility of this approach. However, this project exposed several challenges of working exclusively within the NIR. Figure 3.7 shows that many minerals have features with the same spectral width and center frequency, which makes unique identification challenging unless additional features from under 1 μm or over 1.7 μm are added. Similarly, Tetracorder's polynomial fit algorithms require a broader spectral range to automatically identify minerals, as illustrated by the alunite which was incorrectly identified by Tetracorder in Fig. 3.16. The python-based technique was able to identify a clay mineral (possibly muscovite), but additional development is required to confirm the type of clay. These results indicate that future studies should focus on expanding to include a greater number and diversity of minerals and looking to see how larger sampling distances affect mineral identification.

These findings underscore the need for continued development of Tetracorder to expand its utility for both terrestrial and extraterrestrial exploration. By enhancing its capabilities to address challenges posed by atmospheric absorption and other environmental factors, Tetracorder could become an indispensable tool for autonomous mineral exploration—whether on Earth or distant planetary surfaces, where direct human intervention is not feasible. In field environments, atmospheric and environmental factors such as diffraction, absorption, scattering, reflection, and emission significantly influence remote spectral measurements, presenting challenges for accurate

mineral identification. Despite these obstacles, advancements in lightweight hyperspectral imaging and onboard data processing have opened new opportunities for real-time adaptation during remote sensing operations. A compact spectrometer equipped with onboard processing capabilities could intelligently adjust spectral bands and measurement windows based on the sensor's distance from the target and other environmental or contextual information. This flexibility can enhance the quality of spectral data by dynamically tuning instrument settings and/or location to minimize confounding effects and optimize the signal-to-noise ratio for geologically relevant minerals.

The advancements discussed in this chapter lay the groundwork for future research and development aimed at optimizing Tetracorder for a broad range of remote sensing applications. Advanced tools for identifying minerals with limited spectral information are also valuable for various Earth applications. HSIs are currently being developed for use in mining (Chevez et al., 2021), agriculture (Cevoli and Fabbri, 2020; Logan et al., 2020), defense (Bárta et al., 2018), and in geological surveys (Kirsch et al., 2018). On planetary surfaces beyond Mars or the Moon, where direct and continuous communication with Earth is significantly delayed or impossible, a hyperspectral imager capable of autonomously optimizing its spectral collection would offer substantial advantages. The capability for real-time adjustment is particularly valuable in autonomous missions, where observational conditions are unknown beforehand and communication with remote science teams is limited or infeasible.

Chapter 4

Developing a Semi-Autonomous Mineral Mapping Technique

Abstract

When exploring planetary surfaces, scientists traditionally work with measurements collected over many years from orbit and on the surface (in situ), from a lander or rover platform. Synthesizing this data often results in gaps from missed material due to the coarse spatial resolution of orbital data and poor spatial coverage of surface data. Advances in microelectronic and battery technologies have recently made a new class of instrument platforms possible: planetary aerial vehicles (PAVs), demonstrated by the Ingenuity helicopter on the Mars 2020 mission. Operating tens to hundreds of meters above the surface, PAVs have the potential to bridge the gap between orbital and in situ measurements. This study explores the scientific capabilities of PAVs outfitted with a near infrared (NIR) hyperspectral imager (HSI) and mineral identification software, Tetracorder (Clark et al., 2003). A drone mountable PikaIR HSI was deployed during a field campaign by the Toolbox for Research and Exploration (TREX) team in October 2022 in Yellow Cat, Utah. Hyperspectral imaging capability was tested by collecting NIR spectra from geologic layers of interest at a middle spatial resolution between other airborne (representing 'orbital') and in situ spectrometers. In addition, the benefits of enhanced mobility from a PAV were explored by targeting terrain not accessible to the ground team such as steep cliffs. Spectra from each instrument are processed by Tetracorder to autonomously identify minerals in some areas, with additional manual processing in the PikaIR data. Each spectrum is used like a fingerprint to identify materials with similar signatures in an image, revealing the spatial relationships of rocks and sediments outside of the visible

spectrum. The 'orbital', 'ground', and 'drone' data are compared and used to identify geologic characteristics of the field site. These observations are intrepreted to infer the geologic origin of layers where possible. The advantages of collecting data in the spatial resolution gap between an orbital and ground asset is assessed by detailing geologic context of the field site that was gained from the PAV. Looking forward, VNIR hyperspectral imagery could be integrated into PAV payloads for a mid-resolution survey, to aid autonomous or human-directed surface operations and science planning for future missions.

4.1 Introduction

The planetary science community has made significant investment improving the spatial and spectral resolution of orbital and surface spectrometers. However, comparing their data is challenging, sometimes leading to weeks or months of uncertainty interpreting their measurements. To study this problem and test solutions, numerous teams have conducted simulated missions in planetary analogs, which are field sites that the team treats as an unknown planetary surface. During these studies, the science team is typically isolated from the field site directing the actions of a remote field team as if they were on Earth directing the exploration of another planet. Constraints are applied to simulate the limitations of a planetary mission such as limited time, distance, rate of travel, data volume, and/or rate of data transmitted. Measurements from the field team are used to guide the science team's decisions for data collection as they assess the site. These studies noted a common challenge: obtaining geologic context efficiently while isolated on another planet in a data and resource starved environment.

Specifically, early programs like Desert Research and Technology Studies (DRATS) noted a data volume bottleneck in their 2010 operation (Eppler et al., 2013). This was managed by prioritizing certain data sets, often those expected to provide good geologic context rather than the highest resolution measurements. An analogue mission at the Mistastin Lake impact structure in Labrador, Canada found that broad data collection should be prioritized before focusing on the detailed measurements of a scientific target (Antonenko et al., 2013). The GeoHeuristic Operational

Strategies Test (GHOST) in 2016 compared different traverse strategies and found that gaining site context through low-resolution spatial coverage of a small landing site was the most critical factor for making efficient and scientifically robust observation decisions. Lack of context data resulted in selecting sampling locations that lacked breadth and diversity (Yingst et al., 2017, 2020). The CanMars Mars Sample Return analogue mission determined that instruments with remote capabilities (specifically, spectrometers and remote micro-imagers) are ideal additions to rover missions, since they greatly increase the speed of operations and data acquisition. Like the GHOST team, they noted that obtaining context of the rover operations area was an important challenge (Osinski et al., 2019). Analogue missions have consistently shown that acquiring contextual geologic information should be prioritized early in a mission, even at the expense of more detailed, high-resolution data.

The need for geologic context is addressed with an intermediate-scale HSI drone survey. This survey is intended to work in tandem with other surface exploration efforts (such as a rover and astronaut team). The HSI can survey a landing site prior to the surface team's arrival, or alongside an existing team acquiring data from a broader region or inaccessible terrain. Ultimately, this data could be incorperated into the workflow for geologic mapping described in Noe Dobrea et al. (2023), with the goal of improving the synthesis of multi-scale data products for future studies.

TREX, a node of NASA's Solar System Exploration Research Virtual Institute (SSERVI), has been testing the role that science autonomy can play in geologic mapping of planetary analogs. The rapid synthesis of different data sources is taken one step further by processing surface measurements alongside pre-existing airborne datasets with Tetracorder onboard a rover. The rover, Zoë, was provided by Dr. David Wettergreen's team at Carnegie Mellon (Cabrol et al., 2007) and was able to continually update a geologic map autonomously by identifying minerals and using them to infer the stratigraphy and geologic origins of units (Noe Dobrea et al., 2023; Clark et al., 2003).

Seperately, I investigated how a PAV might address the need for geologic context. The PikaIR camera from Resonon is a NIR hyperspectral imager that can be mounted to a drone. The TREX field test in Yellow Cat, Utah provided an ideal opportunity to test how a PAV instrument platform

could work alongside data from satellites, rovers, and astronauts (Noe Dobrea et al., 2023). During this study, an isolated science team was stationed in a nearby hotel (acting as the Earth-based mission control) to remotely command Zoë as it explored approximately 4km from the landing site using different levels of automation. I brought the PikaIR to act as a PAV and collect hyperspectral imagery of the field site at a mid-range resolution alongside the TREX team. To assess how this instrument would aid exploration of a simulated planetary landscape, I processed the data with Tetracorder and created maps of mineral deposits in the region. These observations aided the geologic interpretation of the field site.

4.2 Methods

The site in Yellow Cat, Utah is situated on the Morrison formation (light green in Fig. 4.1), which is a well mapped area containing abundant iron oxides, carbonates and clay minerals. A variety of geologic units in the Ceder mountian formation are exposed in the surrounding cliffs as shown in Fig. 4.1 (Doelling and Kuehne, 2013). This site was selected for its lack of vegetation, geologic diversity (including an old uraninum mine), and exposure of horizontal layering in the Yellow Cat member of the Cedar Mountian formation (brown in Fig. 4.1, also seen in Fig. 4.2), making it an acceptable planetary analog. Fig. 4.2 shows both the diversity of the land surrounding the valley and the difficulty of the steep surrounding terrain for the rover. Z

Coarse HSI of the site was provided by the airborne visible and infrared imaging spectrometer (AVIRIS), which flies at a 20km altitude with a spatial resolution of 18m/pixel over a $0.4\mu m - 2.5\mu m$ wavelength range with 224 channels (Vane et al., 1993; Green et al., 1998). The AVIRIS data product is roughly equivalent to CRISM, the compact reconnaissance imaging spectrometer for Mars (Viviano et al., 2014). In 1995, AVIRIS flew over the Yellow Cat site and collected hyperspectral data as one of the early calibration tests for the instrument (Clark et al., 1998, 2003). Minerology across the site was subsequently mapped and validated in the field with contact VNIR instruments as shown in Fig. 4.3 (Clark et al., 2003). The TREX rover team converted this mineral information alongside higher resolution Google Earth topography data into an initial geologic origins map of

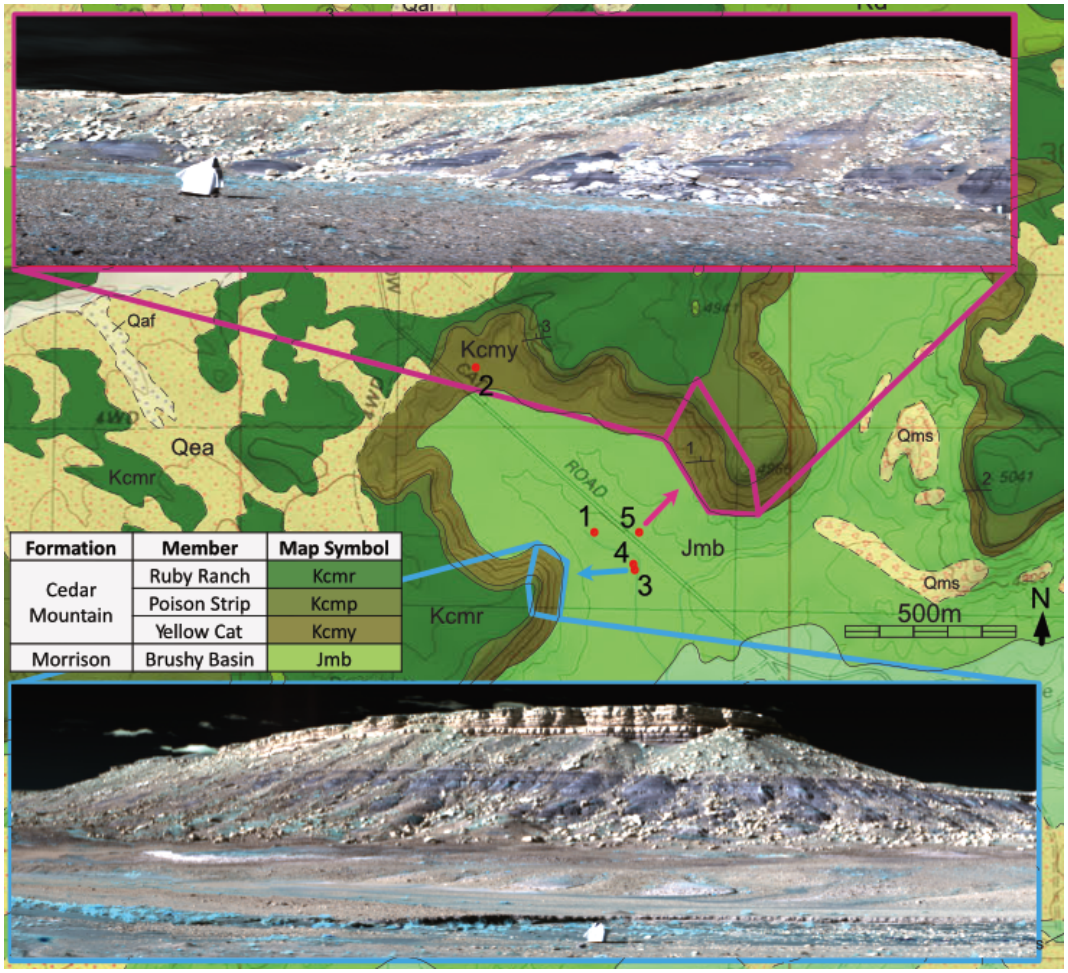

Figure 4.1: Geologic Map of Field Site: This map shows the overlay of the geologic map from the Utah geologic survey of the field site in Yellow Cat Utah (Doelling and Kuehne, 2013). The contour interval is 40 ft (12.2m). Red dots 1-5 show locations of the hyperspectral camera. At sites 3 and 5, arrows indicate the orientation of the HSI for data collection, and false color HSI images from the datacubes collected at these locations is shown. These datacubes are the two scans highlighted in table 4.1 which are analyzed in this study.

Figure 4.2: PikaIR hyperspectral imager in Yellow Cat, Utah field site with white calibration target. Cliff 1 is shown in the background.

the field site (Noe Dobrea et al., 2023). Figure 4.3 was used by Zoë's autonomous programming and the humans on the science team to plan the rover's route.

4.2.1 Hyperspectral Data Collection

The near infrared HSI used in this study is the PikaIR, loaned by Resonon Inc. in Boseman, MT. The PikaIR camera has a wavelength range of $0.9 - 1.7\mu m$ and 164 spectral channels with a FWHM of 8.8 nm. The camera scans from right to left at a rate of 0.2038 degrees per second and 4.993 frames per second (Resonon, 2024). It is drone mountable, but for this study it remained mounted to a tripod and was carried throughout the field site for simplicity.

Reflectance spectrometers like the PikaIR use the Sun as an illumination source and measure the light reflected off of the target. Water or snow on the ground will limit the ability to observe the minerals below, as water has spectral features in the near infrared that would dominate over other spectral features of the minerals (as discussed in section 1.3). Optimal operational conditions are therefore a dry, cloud-free day when the Sun is at the correct angle to illuminate the cliffs. During TREX's two week field campaign, the PikaIR was available for one week which also had dramatic weather conditions including snow, hail, and rain. The best data collection occurred on October 27th, 2022 which was dry and sunny, and a summary of the PikaIR field operations are in Table 4.1. This study will use datacubes from 2 locations which are highlighted in grey.

Each scan started with a dark current measurement taken with the lens cap on. This measures the background signal on the sensor caused by temperature and varies dramatically throughout the day. Next the integration time was set based on a rate of five frames per second. This varied based on lighting; when conditions are bright, the detector received more photons, requiring less time to collect the signal. A white reference was included in each scan which is shown as a white canvas in the background of Fig. 4.2. I collected data at distances ranging from ∼40-60m from the cliff faces which results in spatial data under 0.1m per pixel. The raw spectral counts were converted to radiance using the imager calibration provided by Resonon, and then the white reference was used to convert radiance to reflectance values. Using reflectance values excludes some of the effect

1 μm Group Minerals Mapped by AVIRIS

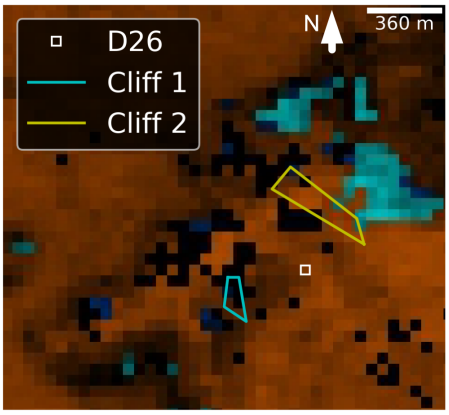

Fe3+ oxide	Fe3+ hydroxide
Hematite coarse grained	Goethite coarse grained
Hematite medium grained	Goethite medium grained
Hematite fine grained	Goethite fine grained
Hematite nano	Goethite thin coating
Fe2+, Fe3+ minerals	
Fe2+ minerals	Fe2+ /Fe3+ mixtures
Fe2+ minerals	Fe3+ Mixtures
Fe2+ minerals	Fe3+ Iron Sulphates
	Fe3+ Jarosite

2 μm Group Minerals Mapped by AVIRIS

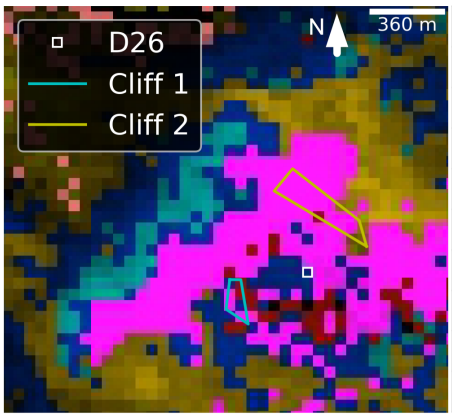

Clays	
Montmorillonite Group	Kaolinite Group
Mont. Group Mixtures	Mixtures with Kaolinite
Illite / Muscovite	Illite / Muscovite Mistures
Sulfates	**Carbonates**
Gypsum	Calcite
Mixtures with Gypsum	Mixtures with Calcite
Other Sulfates	Other Carbonates
Other Minerals	
Zeolites	Chlorites, Serpentines, Other

Figure 4.3: Airborne Visible / Infrared Imaging Spectrometer (AVIRIS) datacube with minerals mapped by the Tetracorder expert system (Clark et al., 2003). Colors represent the mineral groups described by the table, and the blue and yellow polygons represent Cliff 1 and Cliff 2, respectively. The white square D26 indicates a calibration spot that matches the D26 rover stop from Noe Dobrea et al. (2023).

Table 4.1: Summary of PikaIR scans collected in the field. The time, date, and location of each scan are indicated in the first three columns. The PikaIR instrument settings (integration time and direction pointed at the start of the scan) are in columns four and five. Column six contains notes from the scan, such as relevant weather conditions or objects in the field of view. Grey highlighted rows indicate the two scans (of cliff 1 and cliff 2 respectivley, as shown in Fig. 4.1) selected for analysis in this work.

Time (hh:mm)	Latitude ($^\circ N$)	Longitude ($^\circ W$)	Integration Time (ms)	Direction (deg)	Notes
day1	tbd	109.54123	20	184 S	Day 1, wet
day2	tbd	109.5451	23	NW	Day 2, wet
10:55	38.85152	109.53989	14.959	210 SW	Day 3, sunny with thin sparse clouds
11:06	38.85152	109.53989	14.959	210 SW	
11:22	38.85152	109.53989	15.905	210 SW	
11:29	38.85152	109.53989	15.905	210 SW	
11:49	38.85152	109.53989	15.905	210 SW	windy
12:27	38.85152	109.53989	14.208	210 SW	pointed camera at ground
12:50	38.85152	109.53989	12.866	210 SW	measured ground with closer calibration target
13:15	38.85152	109.53989	7.269	210 SW	wind blew over calibration target
13:27	38.85152	109.53989	7.269	223 SW	box truck is calibration target
13:36	38.85152	109.53989	7.269	233 SW	box truck is calibration target, lisa in FOV
14:49	38.8525	109.53966	7.269	SE	D26 ground, white canvas reference, along rover path
14:53	38.8525	109.53966	7.269	SE	
14:58	38.8525	109.53966	7.269	SE	
15:20	38.8525	109.53966	7.269	192 S	clear skies, small clouds, hand on tripod to stabilize during wind gusts
15:34	38.8525	109.53966	7.269	192 S	
15:48	38.8525	109.53966	7.269	192 S	stepper mode, 0.040938^o step size
16:01	38.8525	109.53966	7.269	192 S	auto

of varying environmental conditions, and can be compared with a library of reference spectra (also reported in units of reflectance). Superimposed on Fig. 4.1 are PikaIR images of the cliff faces to the south-west (cliff 1) and north-east (cliff 2) of the valley explored by the rover. Each pixel from these images contains full spectral information and can be analyzed to assist in mineral identification of the surrounding area.

Zoë has three rover mounted instruments: a $0.35 - 2.5\mu m$ VNIR line spectrometer from Advanced Spectral Devices (ASD), a color camera, and a rover mounted gamma ray spectrometer (GRS). In addition, the TREX field team operated several portable instruments: a hand-held $0.35 - 2.5\mu$m VNIR probe from ASD, a hand-held $4 - 15\mu$m FTIR, a portable UV spectrometer, a micro imager, and a portable powder X-Ray Diffraction (XRD) instrument. Zoë continuously collected data while driving with the mounted VNIR and GRS. At each stop, Zoë collected data with the VNIR and color camera, and took measurements from the portable instruments (Noe Dobrea et al., 2023).

The remote science team received in situ measurements from the rover stops and compared them with the map from AVIRIS (Fig. 4.3) to interpret the field site. The resolution gap between these data sets is compounded by the topography and stratigraphy in this field site. For instance, the cliff faces surrounding the valley explored by the rover contain diverse geologic layers, namely a $\sim$ 15m thick mudstone unit (Doelling and Kuehne, 2013) containing red and white layers which are impossible to resolve with AVIRIS, but can be seen with Zoë's visible color camera. Additionally, in planned planetary missions, cliffs (like the ones in Yellow Cat) may be too steep for the rover or astronauts to traverse to directly sample with in situ instruments. However, the rover or astronauts may occasionally encounter material from this unit as float in the valley floor. If the science team had HSI data of the cliff at < 0.5m/pixel resolution, it would be more plausible to trace this float back to a stratigraphic layer. Thus HSI is a powerful tool that could transform the understanding of minerals in a broader region around the rover landing site than is otherwise possible from satellites and rovers alone.

Although the spatial resolution of the PikaIR has the potential to enable new scientific anal-

yses, the limited spectral range of $0.9 - 1.7\mu$m when compared with AVIRIS's range of $0.4 - 2.5\mu$m creates new challenges. Figure 4.4 examines the spatial and spectral gaps between these HSI instruments in more detail. Fig. 4.4.a shows Cliff 1 with the visible red / white mudstone units. Fig. 4.4.b shows re-processed AVIRIS data restricted to the same spectral range as the PikaIR. The AVIRIS spatial resolution is far too coarse to identify the horizontal mudstone units. Additionally, the restricted $0.9 - 1.7\mu$m spectral range highlights the limitations of Tetracorder's mineral identification in the NIR. Zeolite, ulexite, and alunite minerals are mis-identifications with poor spectral fits because most minerals in Tetracorder require features outside of the $0.9 - 1.7\mu$m range for a positive identification. This exposed the limits of AVIRIS data, which has channels removed due to atmospheric interferance between $1.3 - 1.5\mu$m, and cannot be used in this limited spectral range. In Fig. 4.4.c, I used the method developed chapter 3 to identify minerals from the PikaIR dataset. The spatial resolution and spectral range is enough to identify horizontal layering of different clay minerals, which will be discussed more in section 4.3.

4.2.2 Hyperspectral Data Analysis

Spectronon software was used to calibrate the datacube from the PikaIR using the canvas as a white reference with a measured spectrum (measured by the ASD HandHeld 2 contact spectrometer) (Resonon, 2024). Spectra of the raw data on the canvas (in light and in shadow) and on some representative rocks were reviewed to determine bad channels (e.g. near the water absorption band in the atmosphere) where there was not enough signal. These channels are removed and the datacube is imported into Tetracorder for mineral identification. This approach requires a comprehensive library of reference spectra acquired under controlled conditions to serve as a basis for comparison with the unknown PikaIR spectra. The reference spectra used in this project are from the USGS Spectral Library version 7 database, which has over 1,100 spectra of pure and mixed minerals (Kokaly et al., 2017). These reference spectra are loaded into the library software Specpr (SPECtrum Processing Routines). Specpr is an open source software with similar features to ENVI which is used for general spectral analysis and plotting. These spectra were convolved to

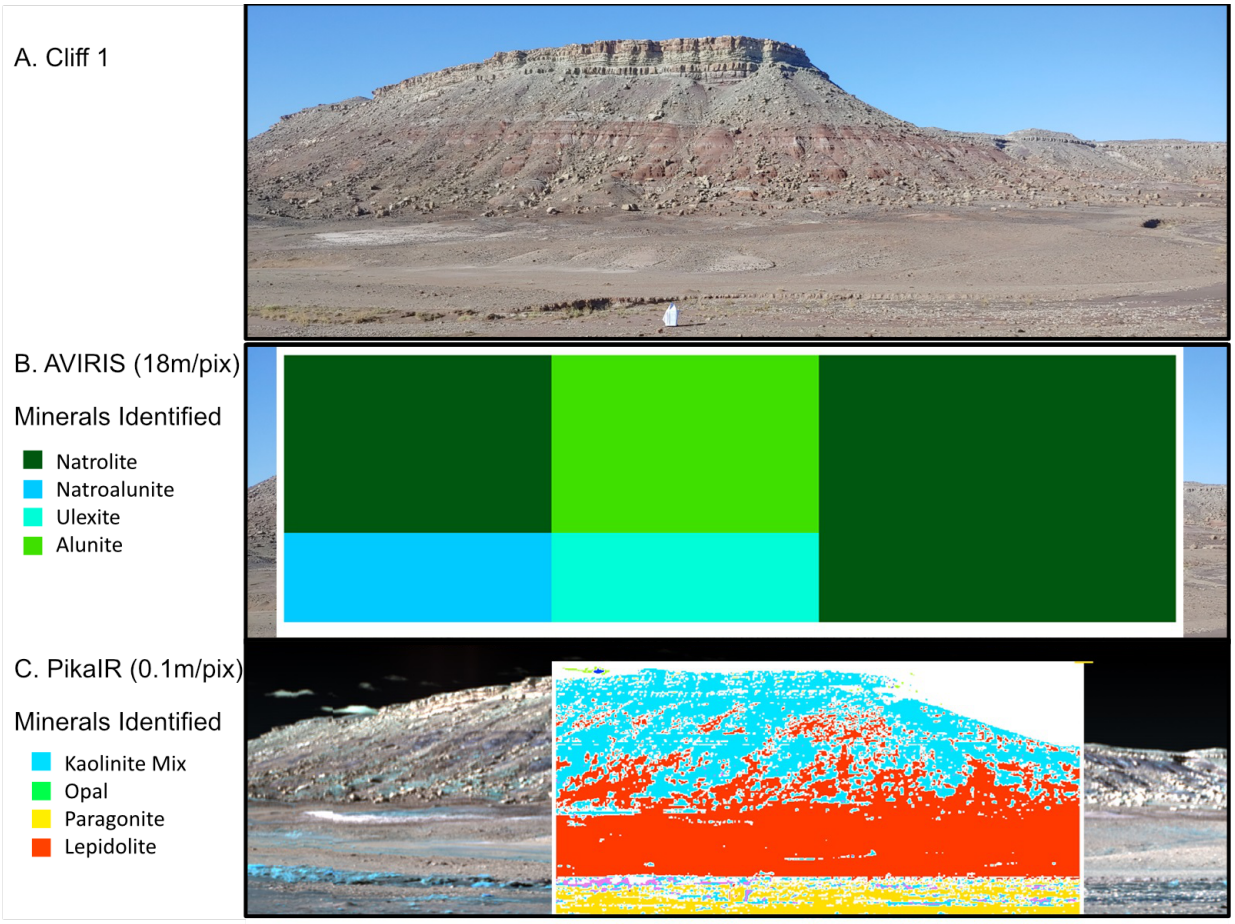

Figure 4.4: Comparing the spatial resolution and spectral ranges of the AVIRIS and PikaIR instruments for cliff 1 from the Yellow Cat field site from in Fig. 4.1. A: Color photo of cliff 1. B: Minerals identified in AVIRIS data restricted to the subset of frequencies within the PikaIR range ($0.9\mu m$ - $1.7\mu m$) overlaid on the approximate area of the cliff. C: Minerals identified in the PikaIR data from the 1.4 μm group overlaid on cliff.

match the wavelength channels of the PikaIR instrument for comparison. In the Tetracorder expert system (meaning the code that identifies minerals based on spectral features), minerals are grouped based on their absorption features, as discussed in Chapter 1. In this study, I reference the VNIR groups, which include $1\mu m$ and $2\mu m$, developed during the AVIRIS program and used on many mission projects. Spectroscopists manually catalogued each of the mineral absorption features in the expert system and did extensive testing in Cuperite, NV to determine that they can be used to make unique identifications (Clark et al., 2003; Swayze et al., 2003, 2014).

Mineral diagnostic features must fit within the wavelength range of the spectrometer to be identified by Tetracorder. For instance, hematite has a broad feature that extends below the lowest range of the PikaIR (0.9μm - see Fig. 1.1). Since there are no data available in the starting wavelength window defined by the expert system, Tetracorder cannot use it for mineral identification. Future studies could evaluate adding a hematite shoulder to address this. Similarly, group 2 minerals like calcite and muscovite have features from $2.2 - 2.4\mu m$ which cannot be used (see Fig. 1.1). In fact, I found that the only group 2 minerals that could be identified in the $0.9 - 1.7\mu m$ range were alunite mixtures, but manual verification of these spectra showed a poor fit (Steckel et al., 2024a). The atmospheric water band previously made using data in the 1.3, 1.4, and 1.5μm groups inaccessible to AVIRIS and similar air and space spectrometers on Earth, so their use in this setting is novel. Further work described in chapter 3 included manual editing of the expert system to fit features within the $0.9 - 1.7\mu$m range where possible and an additional manual spectra validation process. Upon further investigation, several phyllosilicates could be identified using this process, and will be discussed in section 4.3. Snippets of the expert system referenced in this project can be found in appendix D.

4.3 Results: Field Site Characterization

A high-resolution hyperspectral imager was tested in a planetary analog setting to simulate the effects of drone assisted exploration, inspired by the Ingenuity helicopter in the Mars 2020 mission. A drone-mountable PikaIR HSI collected NIR spectral data from layers exposed in sur-

rounding cliffs in the field site which were missed from aerial and in situ exploration by AVIRIS and Zoë. Tetracorder was used alongside manual tools to process the data and identify minerals from the USGS spectral library. These observations are interpreted with additional data provided by TREX collaborators in Noe Dobrea et al. (2023) to characterizate the field site.

Understanding the constituents of these cliffs is critical to understanding the context of the field site. Fig. 4.2 shows visible layers which are also seen in the false color NIR images in Fig. 4.1. By using a HSI, minerals in layers of these cliffs can be identified in space which adds context to the interpretation of targets studied by the rover, which may include float from these units. For example, if the cliffs are made up of all secondary minerals common in evaporative depositional environments, rocks are likely sedimentary in origin. Alternativley, if the cliffs contain many igneous minerals that show little or no signs of alteration, rocks likely have an igneous origin. In future studies, if layers in the cliffs have unique spectral signatures, pieces of float from the canyon floor could be traced to its parent material. This type of investigation is currently underway with the Mars 2020 science team in Jezero Crater, who started collecting samples in a river delta but are now climbing the rim of an impact basin. Context of the surrounding outcrops aids the selection of sampling targets for the rover, for instance to seek out a missing unit in a stratigraphy column.

This TREX field study was initialized with low resolution (18m/pixel) data collected by AVIRIS. The group 1μm minerals mapped in Fig. 4.3 show a mixture of hematite grain sizes in and between both cliffs. Around cliff 1, kaolinite mixtures are shown in magenta and illite / muscovite mixtures are shown in the blue in the 2 μm group minerals from Fig. 4.3. Cliff 2 was dominated by kaolinite mixtures with some calcite mixtures in the yellow pixel near the southernmost end of the cliff face in Fig. 4.3. The coarse spatial resolution and steep angle of the cliff faces means these minerals cannot be traced to the units exposed in the cliff. However, these observations are useful context when interpreting the setting of this area.

During the TREX field work, the rover team could not access the cliffs due to their steep incline and poorly consolidated material which could not be climbed. Although Zoë had a VNIR spectrometer mounted to its mast capable of collecting data from remote distances, a malfunction

early in the field campaign required engineers to lock it pointed towards the ground so that it could access its calibration target and and continue to operate (Noe Dobrea et al., 2023). This prevented the spectrometer from sampling the surrounding cliffs, which became the primary target of the PikaIR.

The PikaIR HSI targeted these cliffs using the setup from Fig. 4.2. The processed results of the HSI data are shown in Fig. 4.5 and 4.6. These data were processed with Tetracorder alongside custom manual tools I developed to group similar spectra, average them, and compare them to the USGS spectral library. Spectra were examined manually with my custom Python scripts to evaluate the mineral with the best fit as shown in Fig. 4.7. In 4.7.a, the data plotted in black is the mean spectrum from the green pixels in Fig. 4.5.a. All 99 library minerals from these groups were scaled to match this absorption feature. Each data point in the plotted spectral range around the absorption feature (not from the entire spectrum) was used to calculate the least squared fit parameter (r). The best 4 library mineral fits are plotted in color in 4.7.a, and the minimum r is the best fit, which is the kaolinite/muscovite mixture plotted in blue. This is an areal (linear) mixture calculated using the spectra of pure end members 50% kaolinite CM9 and 50% muscovite GDS113 (Clark et al., 2007). The ascii files of each library mineral were downloaded from Kokaly et al. (2017), and this database includes other mixtures of kaolinite and muscovite (from different end member spectral samples) which were also found to be close fits, and data cards describing this are in Clark et al. (2007). The r values for all of the other minerals checked are listed in table B.1. In addition, the r values for the other two groups in 4.5.a, the blue and light blue, are included in table B.1. This same process was applied to all of the identified mineral groups from Fig. 4.5.b, 4.5.c, and 4.6.a-4.6.c. The tables detailing the fit parameter for all minerals are in appendix B tables B.2, B.3, and B.4.

The jarosite identification in Fig. 4.7.c exposes some of the limitations of this method. Jarosite has a small vibrational absorption feature around 1.5μm which changes in width and position based on the amount of potassium or sodium present (Swayze et al., 2008). In the PikaIR data, the feature is very small and its shape is very bland. This results in an excellent fit parameter

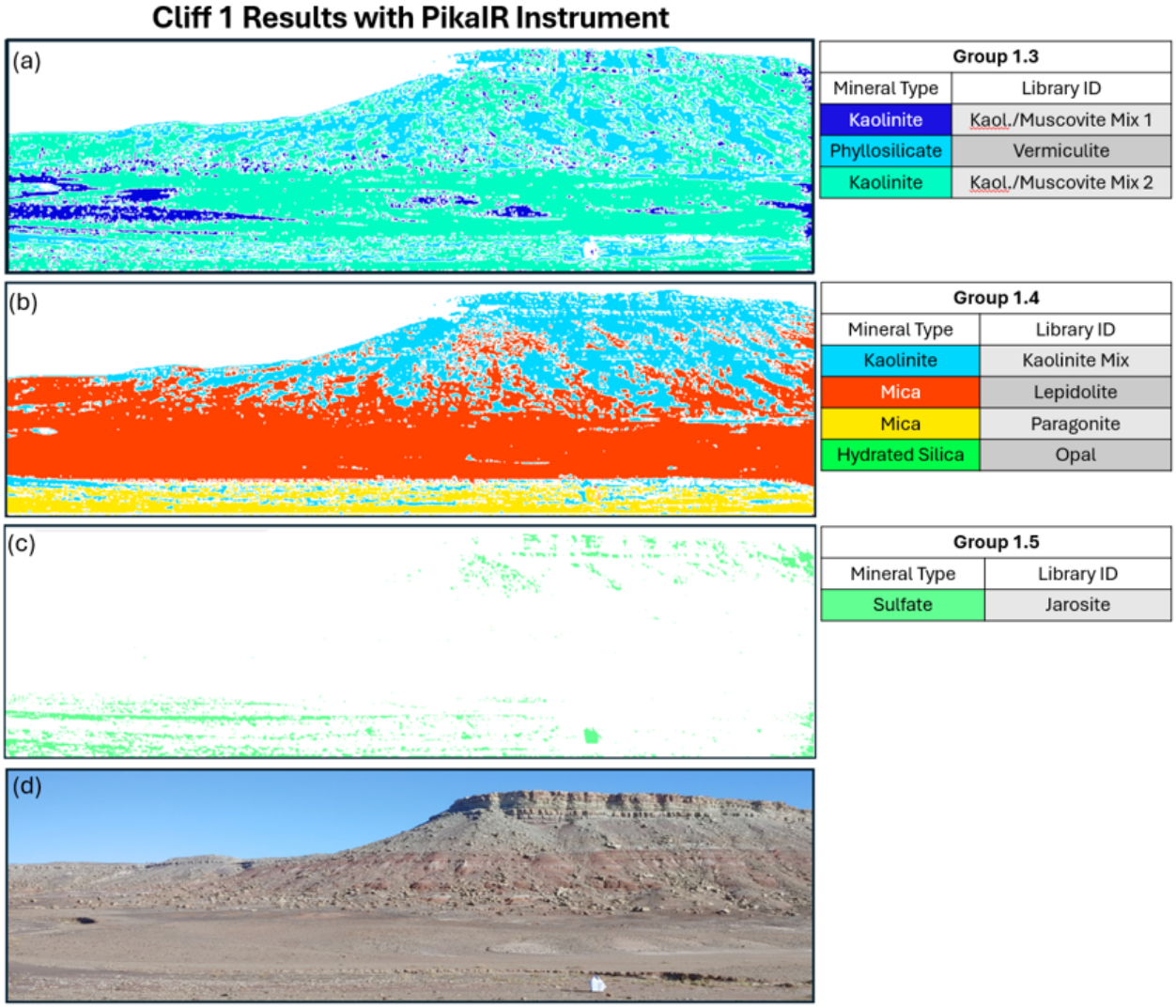

Figure 4.5: Minerals identified in cliff 1 from PikaIR data are provisional based on the analysis in this work. Color represents a mineral and white represents no mineral identified. Further investigation is required before these identifications can be considered definitive. Details of the fits for each mineral are in appendix B. A) Three minerals were identified in the 1.3 μm group, and are colored in blue, light blue, or green. B) Four minerals were identified in the 1.3 μm group, and are colored in light blue, red, yellow, or green. C) One mineral was identified in group 1.5 μm which is colored in green. D) Color photo of cliff 1 for visual reference showing the location of the white canvas calibration target.

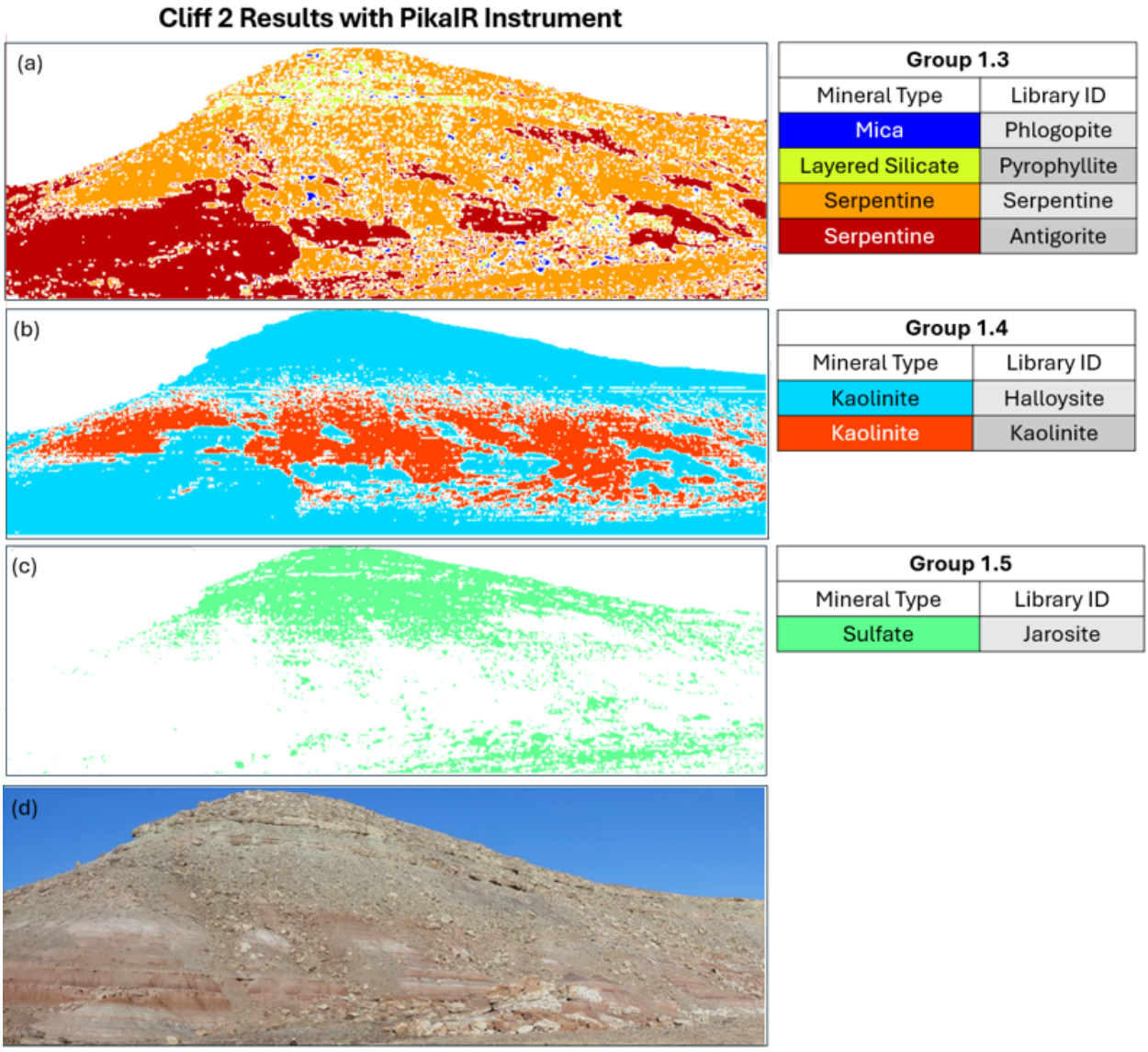

Figure 4.6: Minerals identified in cliff 2 from PikaIR data are provisional based on the analysis in this work. Color represents a mineral and white represents no mineral identified. Further investigation is required before these identifications can be considered definitive. Details of the fits for each mineral are in appendix B. A) Four minerals were identified in the 1.3 μm group, and are colored in blue, yellow, orange, and red. The orange and red are not present in the site and are discussed in the text as spectra that do not have a unique enough feature for identification. B) Two minerals were identified in the 1.4 μm group, and are colored in light blue, and red. C) One mineral was identified in group 1.5 μm which is colored in green. D) Color photo of cliff 2 for visual reference.

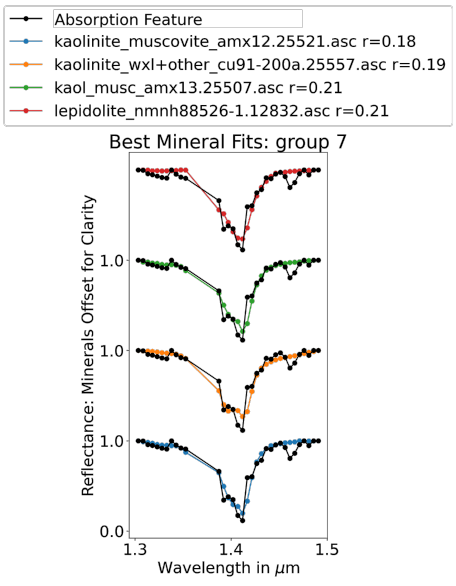

(a) Manual mineral ID of a Kaolinite/ Muscovite mixture using the 1.3μm group of minerals in the cliff 1 (green)

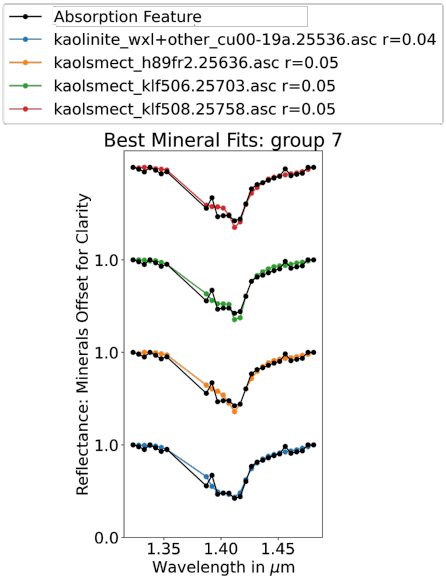

(b) Manual mineral ID of a Kaolinite using the 1.4μm group of minerals in the cliff 1 (light blue)

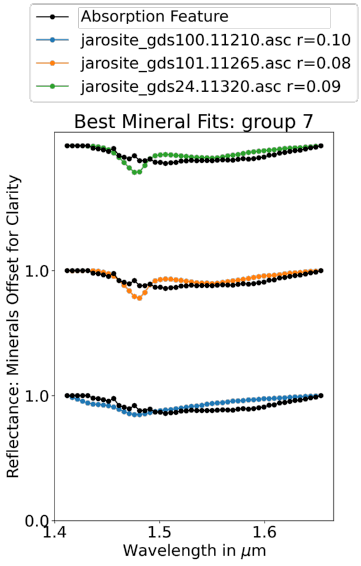

(c) Manual mineral ID of Jarosite using the 1.5μm group minerals in the cliff 1 (green)

Figure 4.7: The absorption feature used for mineral identification from one of the color groups group in Fig. 4.5 is plotted in black. This is the average spectrum from the PikaIR data and with the background continua removed. The best fitting library minerals have been plotted in color for comparison and have been scaled to match the feature depth. The least squared fit parameter r is computed and listed in the legend, with the lowest number indicating the best fit. Library data is from Kokaly et al. (2017).

($r = 0.09$), but likely not a real fit due to its flat profile as seen in Fig. 4.7.c. This material was also found in some pixels of the calibration target, which indicates that this could be noise from the calibration process. Similar issues came up in the 1.3 μm group in cliff 2. Serpentines were found in the red and orange groups of Fig. 4.6.a with excellent r fit parameters. This feature has a single peak and its position and width overlap with many other minerals, so there is not enough unique characteristics to be identified from the cliff spectrum. Additional features outside of the PikaIR spectral range are required to make this identification. Serpentines are alteration products closely associated with mafic or ultramafic material, which was not found anywhere in this site by TREX or the Utah geologic survey (Doelling and Kuehne, 2013).

In summary, the PikaIR identified clays (phyllosilicate group minerals) including mixtures of kaolinites and micas. These classes of clay minerals have long been a target for Mars surface science due to their mineral-bound water, and are often considered to be proof of past liquid water-rock interaction in Mars' history (Du et al., 2023; **?**). In Yellow Cat, this is indeed the source of these clays. This canyon floor is in the brushy basin member of the Morrison formation, and this interpretation is consistent with the Utah geologic survey's interpretation of this layer (Doelling and Kuehne, 2013).

By limiting this study to wavelengths around the water absorption frequencies, I have artificially constrained the diversity of minerals that can be identified and reduced the fidelity of measurement since only one or two spectral features are present in the given range for each group. This is made clear by the ability to identify mixtures that include the kaolinite doublet but the struggle to identify materials with a single feature. If the spectral range were expanded, a larger number of identifying features would be present in the data, and mineral identification would improve.

The limited results present in Fig. 4.5 and 4.6 show that the layers visible in the color images can also be identified in the NIR. In addition to the kaolinite/mica identified by the PikaIR, TREX found hematites, calcite, Fe^{2+} carbonates, illite, and montmorillionite in nearby float materials (Noe Dobrea et al., 2023). This is consistent with the minerals identified by AVIRIS in Fig. 4.3.

These are all minerals commonly found in sedimentary environments. Sometimes referred to as secondary minerals, they are produced from some kind of alteration process, typically requiring water, temperature, and/or pressure. Montmorillionite is in the smectite group of clay minerals, which is often referred to as a "swelling clay" due to its ability expand and take up water between structural layers. Calcite is a common mineral abundant in veins and alteration products. It is a typical precipitate in sediment, and is also common as a cementing medium in sedimentary rocks. These observations could be interpreted as a possible lacustrian origin to the cliff's mudstone unit, with changes in color possibly originating from changes in the oxidation state of iron as water level (and therefore available oxygen) in the lake changed (Deer et al., 2013). If found in a Martian environment, minerals that indicate chemical redox potential (such as $Fe^{2+} - Fe^{3+}$) alongside geomorphic evidence for water are some of the key elements required for life to form. In addition, the expectation of small grained mudstones make this unit an exciting target for biosignature preservation if life was present (Bosak et al., 2021).

4.4 Discussion and Conclusion

Tetracorder can be used to group spectra by similar features and deliver datacubes in real time during planetary surface exploration. During this field study, the PikaIR identified clay minerals and horizontal layering in surrounding cliffs, and provided useful context supporting a likely lacustrian origin of these units. This demonstrates how hyperspectral surveys may aid robotic, human, and/or symbiotic human and robotic exploration of planetary bodies.

In this work, limiting the spectral range to the NIR reduced the minerals that can be identified to a small subset (from over 1,100 to 99) with features in that narrow range. Tetracorder was developed to work in a spectral range of $0.35 - 2.5\mu$m, and more development would be required to correctly identify minerals in the limited range of $0.9 - 1.7\mu$m (Clark et al., 2003). In addition, manual evaluation of the spectra produced mixed results. Some minerals with unique spectral shapes (such as alunite, montmorillionite, and kaolinite) might be uniquely identifiable from this information. However, many minerals (such as serpentine and jarosite) only have a single feature

with a single peak in this range, which is not unique enough to make a definitive identification. Future projects should evaluate additional spectrometers outside of the NIR (such as the PikaII VNIR spectrometer) which could identify multiple features per mineral for future work.

The sedimentary setting of the Cedar Mountian and Morrison formations limited the minerals available for testing. Most of the minerals at this site with features in the $0.9 - 1.7\mu$m were phyllosilicates and sulfates. Performing the same analysis using a field site with more diverse minerals, such as the Cuperite, NV hydrothermal systems, would likely yield more identifications of other mineral types (from igneous or metamorphic origins) with features in the same spectral window. Cuperite has the secondary advantage of serving as a calibration site for the AVIRIS program, so there is a lot of existing data characterizing the minerals in the region to use for method development (Swayze et al., 2014; van der Meero and Bakker, 1997; Swayze et al., 1992). This type of hydrothermal site may also be a good analog for the types of minerals seen in ancient hydrothermal settings on Mars, which are interesting astrobiological targets (Hynek et al., 2013; Black and Hynek, 2018; Hynek et al., 2018).

Sedimentary strata containing minerals of non-igneous origin (i.e. secondary minerals) and hydrated minerals have often been a target for surface missions on Mars. The depositional environments forming these minerals are interesting astrobiological targets to study the ancient habitability and organic preservation potential of Mars (Sheppard et al., 2021). From orbit, clay minerals, sulfates, and anhydrous Fe-oxides are global mineral assemblages identified from VNIR spectra that are sometimes referred to as the phyllosian, theiikian, and siderikian mineralogical time periods on Mars. These mineralogical time periods come from comparison with epochs derived from crater counts (i.e. Noachian, Heperian, and Amazonian), and have been linked with changing climatic conditions on the planet (Sheppard et al., 2021). However, it is difficult to connect a mineral assemblage with a specific period in geologic time using this data. Our field study in Yellow Cat, Utah provides the opportunity to identify some of these minerals in horizontal layers with clear superposition relationships representing specific periods in geologic time. As this chapter shows, orbital studies alone do not have the resolution to tie these minerals to specific stratigraphic layers

in the cliffs, and they typically would not be identified until after the rover landed and started collecting in situ data, which may take weeks, months, or years on Mars. With one data collection, a hyperspectral survey prior to landing, or early after landing, could find these minerals and tie them to a specific geologic layer. This would greatly aid the science team when trying to tie secondary minerals with specific formational or depositional time periods, and could have a big impact to the planned exploration strategy. However, hyperspectral data is no substitute for in situ measurements by the rover's suite of high resolution instruments, due to the complex nature of natural surface materials. Measurements from additional instruments such as the rover VNIR and FTIR provide a more complete picture of the site than the HSI acquires alone. This conclusion is consistent with the previous work of Black and Hynek (2018), which had a major finding of the need to expand rover instrumentation beyond the VNIR to the full VIS-SWIR wavelengths to identify more unique spectral features in longer wavelengths valuable for mineral identification. However, even with the limited spectral range of the PikaIR, the TREX team noted that Zoë could have been routed to identify float on the valley floor to match a cliff layer, and more efficiently build a more complete picture of that geologic unit.

Hyperspectral surveys provide valuable context for geologic origins on planetary surfaces. Commercial drone-mountable instruments such as the PikaIR have a limited spectral range, but their close distance to target (50m vs. 20,000m) enables some signal to penetrate through the atmospheric water band. As new missions push the boundaries of exploration out into the far reaches of the solar system, engineering challenges (and costs) accrue just to make the trip and communicate with Earth. For such expensive missions, it is tempting to select simple mission concepts that feel risk free. However, the expense also means these mission opportunities will be rare, making it just as tempting to try riskier techniques for a dramatic science return. Finding ways to expand surveys of geologic surfaces into automated mission routines has the potential to enable surface science that is not otherwise available to outer solar system missions.

Chapter 5

Conclusion

This thesis has presented three remote sensing projects that each develop new techniques to analyze planetary surfaces. Chapter 2 uses new modeling techniques and orbital remote sensing data to gain insight on the source of valley network formation during the Noachian epoch on Mars. Landscape evolution models were developed to simulate the expected morphological differences between two end member scenarios: (1) evenly distributed source water from a climate warm enough to allow precipitation, or (2) water sourced from similar elevations caused by ephemeral melting of ice caps in an otherwise cold and dry climate. The distribution of valley heads versus elevation in the equatorial region of Mars was compared with simulation results. From -1,800m to 3,500m valley heads were evenly distributed, encompassing $> 96\%$ of total valley heads in the area. Individual valley networks at a similar scale to the simulations were also evaluated and found to have no correlation with elevation. On Mars, there is little evidence for concentrations of valley heads at higher elevations expected if ice melt is the dominant water source. These geomorphic observations indicate that valley networks on Mars are not fully explained by the late Noachian icy highlands model, and are better accounted for by a warm and wet climate dominated by precipitation and runoff. Future studies could add detail to the landscape evolution modeling effort to incorperate the effect of sediment tranport on valley incision. In addition, different landscape shapes and spatial distributions of input water could also be evaluated to more accurately represent a natural watershed to see if this affects the head distributions.

In chapter 3, a NIR hyperspectral imager was also used to expand existing mineral identifi-

cation techniques. Tetracorder, a semi-autonomous mineral identification tool, was modified and expanded upon to develop a semi-autonomous mineral mapping technique. I explored if the unique data set collected by the HSI (attenuated by $\sim$ 1m of Earth atmosphere) could be used to identify absorption features around the atmospheric water band. A set of 99 minerals grouped by Tetracorder were evaluated, and although further development of the autonomous software is required, manual identification showed that some features were unique enough to be identified (such as a doublet in kaolinite). However, some spectral data had shapes that were less unique and more difficult to match. More work is required to evaluate all minerals in this spectral range, compare any with similar central wavelengths and feature widths, and ensure they have unique enough shapes to be used for identification. To develop these techniques further, future studies should consider a field site with more mineral diversity such as the Cuprite, NV hydrothermal system to expand the mineral detection. More minerals and mineral mixtures may also need to be added to the database, depending on the field site tested.

Semi-autonomous mineral identification using a drone mountable HSI is valuable for many Earth industries in addition to the planetary science community. NIR spectrometers have been developed for many agricultural applications which include using drones to autonomously survey crop fields remotely. The mining industry could also benefit from drone based mineral identification for mineral exploration. These platforms currently ignore data in the water absorption band, but chapter 3 shows that there is potental to collect data in this area, with several caveats. Existing polynomial fit techniques to the spectral features identified around the 1.3-1.5μm are not sufficient for mineral identification, but expanding the spectral range to add other VNIR features in shorter and longer wavelengths may result in more robust and detailed mineral identifications than is currently available. For planetary scientists, it would be useful to test these techniques on Earth before moving to atmospheres with different compositions and different attenuation bands.

To improve the ability to capture geologic context data in a planetary surface setting, chapter 4 describes the field test of a portable, mid resolution hyperspectral imager (HSI) alongside rover and orbital datasets. The field site contained sedimentary units ideal for preserving biomarkers,

with exposure on steep cliff walls inaccessible to the orbital and rover teams. HSI acquired high resolution NIR spectra of these units and found different compositions of phyllosilicates. Clay minerals are difficult to differentiate with spectra due to their structural similarities, but the preliminary grouping of spectra with Tetracorder revealed some detail of the sedimentary units and horizontal layering. Knowledge of the phyllosilicates alongside the in situ and orbital data implies a lacustrian origin to the unit, improving the geologic interpretation of the sedimentary unit origins. Future projects could develop this further by using an imager with a broader spectral range, or by selecting field sites containing more diverse mineral groups (such as the hydrothermal vents at Cuperite, Nevada).

As we explore deeper into the solar system with more advanced robotic tools and higher computational capacities, it will no longer be possible or advantageous to have humans directly operating these robots in real time. With increased distance from earth, the time required for human centric decisions becomes intractable and a new form of in situ measurement and exploration will be required. Secondary to MSR, the most recent decadal survey (Origins, Worlds, and Life) prioritizes the exploration of astrobiological targets, particularly icy moons in the outer solar system with interior oceans (NASEM, 2022). The closest of these targets to Earth is Europa in orbit around Jupiter, which is planned to be studied by the Europa Clipper mission in 2030 (Pappalardo et al., 2024). Another compelling ocean world target with the largest unmapped surface in our solar system is Triton, a moon in orbit around Neptune at 30 AU (Hansen et al., 2021). The round-trip communication delay at Europa is approximately 2 hours, and at Triton is approximately 8 hours, which prevents scientists from directing the exploration in real time as they have before. Improved instrument capability will aggravate this bottleneck as data volumes increase.

Surface mission durations may also shorten as missions extend farther into the outer solar system, highlighting the need for efficient science operations. Europa Clipper will require a 5.5 year cruise before arriving at Europa (Pappalardo et al., 2024), and mission concepts to Triton typically require an approximately 15 year cruise (Steckel et al., 2024b). It is difficult to get enough solar power to support a mission past Jupiter, and alternative power sources like Radioisotope

Thermoelectric Generators (RTGs) are designed to have only a 14 year operational life further shortening mission duration (Whiting, 2023).

Unfortunately, these long travel times coupled with the large number of diverse moons in the outer solar system make it very unlikely to revisit the planetary surface multiple times. Historically, repeat missions to similar environments allows engineers to implement lessons learned and extend designed surface mission lifetimes. In 1977, the Sojourner rover sent to Mars was designed to last 7 days for its primary mission (Golombek, 1997). In 2004, the Spirit and Opportunity rovers were designed to last 90 days (Crisp et al., 2003; Squyres, 2005). In contrast, modern rovers Curiosity (in 2012) and Perseverance (in 2020) were designed to last 1 and 2 years respectively (Lakdawalla, 2018; Lorenz, 2020). Four rover missions revisiting the same body resulted in a **104x** extension for designed surface operation lifetime. Missions to the outer solar system are less likely to benefit from this enhancement.

The Enceladus Orbilander mission can be used as an example of a reasonable mission concept to the outer solar system where surface exploration time is a bottleneck. The Orbilander mission was selected from an initial group of 163 submitted concepts, then a second pool of 17 mission proposals which received detailed technical risk and cost evaluations by the Aerospace Corporation to be one of 3 flagship missions (receiving the highest level of funding) prioritized by the decadal survey (NASEM, 2022). This mission has a unique concept of operations which includes 1.5 years in orbit, then landing on the surface to spend only 15 days to finish its science goals, maintained only by battery power (MacKenzie et al., 2021). The lander's lifetime is very similar to that of the first Sojourner rover on Mars, but it is less likely that we will return to Enceladus's surface with a lander three additional times.

In this new paradigm of exploration, perpetration for data collection on the planet surface is no longer enough to ensure optimal scientific results. Now, remote sensing prior to mission planning could be paired with autonomous, in-situ, and local geologic scouting to ensure that the data collected is from the most significant sites. This thesis shows a blueprint for how this can be accomplished for distant planets. Once a target is selected, global scale remote data, including

digital elevation measurements, should be used to identify geological features. From these data and remote hyperspectral measurements, several areas of interest can be identified as targets for further investigation. Once arriving on the surface, autonomous scouting via hyperspectral aerial vehicles will inform the exploration track utilizing processing software that can identify minerals and other features that require further contact or local investigation.

Thus, through a combination of orbital remote sensing and targeted in situ exploration, scientists are piecing together the complex geologic histories of planets and moons in our solar system. The advancements in computational power used to simulate landscape evolution or process hyperspectral data have significantly improved our understanding of Mars, leading to new scientific insights and strategic directions for current and future missions. Continuing the development of techniques from this thesis will enable deeper exploration farther into the solar system.

Bibliography

Adão, T., Hruška, J., Pádua, L., Bessa, J., Peres, E., Morais, R., and Sousa, J. J. (2017). Hyperspectral Imaging: A Review on UAV-Based Sensors, Data Processing and Applications for Agriculture and Forestry. Remote Sensing, 9(11):1110. Number: 11 Publisher: Multidisciplinary Digital Publishing Institute.

Alemanno, G., Orofino, V., and Mancarella, F. (2018). Global Map of Martian Fluvial Systems: Age and Total Eroded Volume Estimations. Earth and Space Science, 5(10):560–577.

Anderson, J. L., Karras, J. T., Cacan, M., Kubiak, G., Pyrzak, G., Dor, H., and Pipenberg, B. (2023). Ingenuity, One Year of Flying on Mars. In 2023 IEEE Aerospace Conference, pages 1–18. ISSN: 1095-323X.

Anderson, R. C., Adamo, D., Buczkowski, D., Dohm, J., Haidegger, T., Jones, T., Podnar, G., and Wyrick, D. (2021). Next frontier in planetary geological reconnaissance: Low-latency telepresence. Icarus, 368:114558.

Andrews, D. and Bucknam, R. C. (1987). Fitting degradation of shoreline scarps by a nonlinear diffusion model. Journal of Geophysical Research: Solid Earth, 92(B12):12857–12867.

Antonenko, I., Osinski, G. R., Battler, M., Beauchamp, M., Cupelli, L., Chanou, A., Francis, R., Mader, M. M., Marion, C., McCullough, E., Pickersgill, A. E., Preston, L. J., Shankar, B., Unrau, T., and Veillette, D. (2013). Issues of geologically-focused situational awareness in robotic planetary missions: Lessons from an analogue mission at Mistastin Lake impact structure, Labrador, Canada. Advances in Space Research, 52(2):272–284.

Arvidson, R. E., Poulet, F., Bibring, J.-P., Wolff, M., Gendrin, A., Morris, R. V., Freeman, J. J., Langevin, Y., Mangold, N., and Bellucci, G. (2005). Spectral Reflectance and Morphologic Correlations in Eastern Terra Meridiani, Mars. Science, 307(5715):1591–1594. Publisher: American Association for the Advancement of Science.

Bapst, J., Parker, T. J., Balaram, J., Tzanetos, T., Matthies, L. H., Edwards, C. D., Freeman, A., Withrow-Maser, S., Johnson, W., Amador-French, E., Bishop, J. L., Daubar, I. J., Dundas, C. M., Fraeman, A. A., Hamilton, C. W., Hardgrove, C., Horgan, B., Leung, C. W., Lin, Y., Mittelholz, A., and Weiss, B. P. (2021). Mars Science Helicopter: Compelling Science Enabled by an Aerial Platform. Bulletin of the AAS, 53(4).

Barducci, A., Guzzi, D., Marcoionni, P., and Pippi, I. (2004). Algorithum for the retrieval of columnar water vapor from hyperspectral remotely sensed data. Applied Optics, 43(29):5552–5563.

Barnes, J. W., Turtle, E. P., Trainer, M. G., Lorenz, R. D., MacKenzie, S. M., Brinckerhoff, W. B., Cable, M. L., Ernst, C. M., Freissinet, C., Hand, K. P., Hayes, A. G., Hörst, S. M., Johnson, J. R., Karkoschka, E., Lawrence, D. J., Gall, A. L., Lora, J. M., McKay, C. P., Miller, R. S., Murchie, S. L., Neish, C. D., Newman, C. E., Núñez, J., Panning, M. P., Parsons, A. M., Peplowski, P. N., Quick, L. C., Radebaugh, J., Rafkin, S. C. R., Shiraishi, H., Soderblom, J. M., Sotzen, K. S., Stickle, A. M., Stofan, E. R., Szopa, C., Tokano, T., Wagner, T., Wilson, C., Yingst, R. A., Zacny, K., and Stähler, S. C. (2021). Science Goals and Objectives for the Dragonfly Titan Rotorcraft Relocatable Lander. The Planetary Science Journal, 2(4):130. Publisher: IOP Publishing.

Barnhart, K. R., Hutton, E. W., Tucker, G. E., Gasparini, N. M., Istanbulluoglu, E., Hobley, D. E., Lyons, N. J., Mouchene, M., Nudurupati, S. S., and Adams, J. M. (2020). Landlab v2. 0: A software package for Earth surface dynamics. Earth Surface Dynamics, 8(2):379–397. ISBN: 2196-6311 Publisher: Copernicus GmbH.

Bishop, J. L., Bell Iii, J. F., and Moersch, J. E., editors (2019). Remote Compositional Analysis: Techniques for Understanding Spectroscopy, Mineralogy, and Geochemistry of Planetary Surfaces. Cambridge University Press, 1 edition.

Bishop, J. L., Lane, M. D., Dyar, M. D., and Brown, A. J. (2008). Reflectance and emission spectroscopy study of four groups of phyllosilicates: smectites, kaolinite-serpentines, chlorites and micas. Clay Minerals, 43(1):35–54.

Black, S. R. and Hynek, B. M. (2018). Characterization of terrestrial hydrothermal alteration products with mars analog instrumentation: implications for current and future rover investigations. Icarus, 307:235–259.

Bohren, C. F. and Clothiaux, E. E. (2006). Fundamentals of atmospheric radiation : an introduction with 400 problems / Craig F. Bohren and Eugene E. Clothiaux. Publisher: Wiley-VCH.

Bonnet-Bidaud, J.-M., Praderie, F., and Whitfield, S. (2009). THE DUNHUANG CHINESE SKY: A COMPREHENSIVE STUDY OF THE OLDEST KNOWN STAR ATLAS. Journal of Astronomical History and Heritage, 12(1):39–59.

Bosak, T., Moore, K. R., Gong, J., and Grotzinger, J. P. (2021). Searching for biosignatures in sedimentary rocks from early earth and mars. Nature Reviews Earth & Environment, 2(7):490–506.

Brockers, R., Proença, P., Delaune, J., Todd, J., Matthies, L., Tzanetos, T., and Balaram, J. B. (2022). On-board Absolute Localization Based on Orbital Imagery for a Future Mars Science Helicopter. In 2022 IEEE Aerospace Conference (AERO), pages 1–11. ISSN: 1095-323X.

Burr, D. M., Enga, M.-T., Williams, R. M. E., Zimbelman, J. R., Howard, A. D., and Brennand, T. A. (2009). Pervasive aqueous paleoflow features in the Aeolis/Zephyria Plana region, Mars. Icarus, 200(1):52–76.

Burr, D. M., Williams, R. M. E., Wendell, K. D., Chojnacki, M., and Emery, J. P. (2010). Inverted fluvial features in the Aeolis/Zephyria Plana region, Mars: Formation mechanism and initial paleodischarge estimates. Journal of Geophysical Research: Planets, 115(E7). _eprint: https://onlinelibrary.wiley.com/doi/pdf/10.1029/2009JE003496.

Bárta, V., Racek, F., and Krejcí, J. (2018). NATO hyperspectral measurement of natural background. In Target and Background Signatures IV, volume 10794, pages 17–32. SPIE.

Cabrol, N. A., Wettergreen, D., Warren-Rhodes, K., Grin, E. A., Moersch, J., Diaz, G. C., Cockell, C. S., Coppin, P., Demergasso, C., Dohm, J. M., Ernst, L., Fisher, G., Glasgow, J., Hardgrove, C., Hock, A. N., Jonak, D., Marinangeli, L., Minkley, E., Ori, G. G., Piatek, J., Pudenz, E., Smith, T., Stubbs, K., Thomas, G., Thompson, D., Waggoner, A., Wagner, M., Weinstein, S., and Wyatt, M. (2007). Life in the Atacama: Searching for life with rovers (science overview). Journal of Geophysical Research: Biogeosciences, 112(G4). _eprint: https://onlinelibrary.wiley.com/doi/pdf/10.1029/2006JG000298.

Candela, A., Thompson, D., Dobrea, E. N., and Wettergreen, D. (2017). Planetary robotic exploration driven by science hypotheses for geologic mapping. In 2017 IEEE/RSJ International Conference on Intelligent Robots and Systems (IROS), pages 3811–3818. ISSN: 2153-0866.

Cardenas, B. T., Lamb, M. P., and Grotzinger, J. P. (2022). Martian landscapes of fluvial ridges carved from ancient sedimentary basin fill. Nature Geoscience, 15(11):871–877. ISBN: 1752-0894 Publisher: Nature Publishing Group UK London.

Carr, M. H. (1995). The Martian drainage system and the origin of valley networks and fretted channels. Journal of Geophysical Research: Planets, 100(E4):7479–7507. _eprint: https://agupubs.onlinelibrary.wiley.com/doi/pdf/10.1029/95JE00260.

Carter, J., Poulet, F., Bibring, J.-P., Mangold, N., and Murchie, S. (2013). Hydrous minerals on Mars as seen by the CRISM and OMEGA imaging spectrometers: Updated global view. Journal of Geophysical Research: Planets, 118(4):831–858. _eprint: https://onlinelibrary.wiley.com/doi/pdf/10.1029/2012JE004145.

Carter, J., Riu, L., Poulet, F., Bibring, J.-P., Langevin, Y., and Gondet, B. (2023). A Mars orbital catalog of aqueous alteration signatures (MOCAAS). Icarus, 389:115164.

Cevoli, C. and Fabbri, A. (2020). In-field hyperspectral imaging: An overview on the ground-based applications in agriculture. Journal of Agricultural Engineering, 51(3):129–139. Num Pages: 129-139 Place: Bologna, Italy Publisher: PAGEPress Publications Section: Review Articles.

Chevez, L., Apaza, A., Rodriguez, J., Puga, R., Dávalos, J., and Loro, H. (2021). Virtual Dimension Analysis of Hyperspectral Imaging to Characterize A Mining Sample. In 2021 11th Workshop on Hyperspectral Imaging and Signal Processing: Evolution in Remote Sensing (WHISPERS), pages 1–5. ISSN: 2158-6276.

Clark, R. N., Livo, K. E., and Kokaly, R. F. (1998). Geometric Correction of AVIRIS Imagery Using On-Board Navigation and Engineering Data. Summaries of the Seventh Annual JPL Airborne Earth Science Workshop, pages 57–65.

Clark, R. N. and Roush, T. L. (1984). Reflectance spectroscopy: Quantitative analysis techniques for remote sensing applications. Journal of Geophysical Research: Solid Earth, 89(B7):6329–6340.

Clark, R. N., Swayze, G. A., Livo, K. E., Kokaly, R. F., Sutley, S. J., Dalton, J. B., McDougal, R. R., and Gent, C. A. (2003). Imaging spectroscopy: Earth and planetary remote sensing with the USGS Tetracorder and expert systems. Journal of Geophysical Research: Planets, 108(E12). _eprint: https://onlinelibrary.wiley.com/doi/pdf/10.1029/2002JE001847.

Clark, R. N., Swayze, G. A., Wise, R. A., Livo, K. E., Hoefen, T. M., Kokaly, R. F., and Sutley, S. J. (2007). Usgs digital spectral library splib06a. Technical report, US Geological Survey.

Craddock, R. A. and Howard, A. D. (2002). The case for rainfall on a warm, wet early Mars. Journal of Geophysical Research: Planets, 107(E11):21–1–21–36. _eprint: https://onlinelibrary.wiley.com/doi/pdf/10.1029/2001JE001505.

Crisp, J. A., Adler, M., Matijevic, J. R., Squyres, S. W., Arvidson, R. E., and Kass, D. M. (2003). Mars Exploration Rover mission. Journal of Geophysical Research: Planets, 108(E12). _eprint: https://onlinelibrary.wiley.com/doi/pdf/10.1029/2002JE002038.

Culling, W. E. H. (1963). Soil creep and the development of hillside slopes. The Journal of Geology, 71(2):127–161. ISBN: 0022-1376 Publisher: University of Chicago Press.

Deer, W. A., Howie, R. A., and Zussman, J. (2013). An introduction to the rock-forming minerals. The Minerological Society, London, third edition edition.

Di Achille, G. and Hynek, B. M. (2010). Ancient ocean on Mars supported by global distribution of deltas and valleys. Nature Geoscience, 3(7):459–463. ISBN: 1752-0894 Publisher: Nature Publishing Group UK London.

Di Achille, G., Hynek, B. M., and Searls, M. L. (2009). Positive identification of lake strandlines in Shalbatana Vallis, Mars. Geophysical Research Letters, 36(14). ISBN: 0094-8276 Publisher: Wiley Online Library.

Doelling, H. H. and Kuehne, P. A. (2013). Geologic Map of the Mollie Hogans Quadrangle: the Utah Geological Survey, map 258DM.

Du, P., Yuan, P., Liu, J., and Ye, B. (2023). Clay minerals on Mars: An up-to-date review with future perspectives. Earth-Science Reviews, 243:104491.

Ehlmann, B. L. and Edwards, C. S. (2014). Mineralogy of the Martian Surface. Annual Review of Earth and Planetary Sciences, 42(1):291–315. _eprint: https://doi.org/10.1146/annurev-earth-060313-055024.

Eppler, D., Adams, B., Archer, D., Baiden, G., Brown, A., Carey, W., Cohen, B., Condit, C., Evans, C., Fortezzo, C., Garry, B., Graff, T., Gruener, J., Heldmann, J., Hodges, K., Hörz, F., Hurtado, J., Hynek, B., Isaacson, P., Juranek, C., Klaus, K., Kring, D., Lanza, N., Lederer, S., Lofgren, G., Marinova, M., May, L., Meyer, J., Ming, D., Monteleone, B., Morisset, C., Noble, S., Rampe, E., Rice, J., Schutt, J., Skinner, J., Tewksbury-Christle, C. M., Tewksbury, B. J., Vaughan, A., Yingst, A., and Young, K. (2013). Desert Research and Technology Studies (DRATS) 2010 science operations: Operational approaches and lessons learned for managing science during human planetary surface missions. Acta Astronautica, 90(2):224–241.

Farley, K. A., Stack, K. M., Shuster, D. L., Horgan, B. H. N., Hurowitz, J. A., Tarnas, J. D., Simon, J. I., Sun, V. Z., Scheller, E. L., Moore, K. R., McLennan, S. M., Vasconcelos, P. M., Wiens, R. C., Treiman, A. H., Mayhew, L. E., Beyssac, O., Kizovski, T. V., Tosca, N. J., Williford, K. H., Crumpler, L. S., Beegle, L. W., Bell, J. F., Ehlmann, B. L., Liu, Y., Maki, J. N., Schmidt, M. E., Allwood, A. C., Amundsen, H. E. F., Bhartia, R., Bosak, T., Brown, A. J., Clark, B. C., Cousin, A., Forni, O., Gabriel, T. S. J., Goreva, Y., Gupta, S., Hamran, S.-E., Herd, C. D. K., Hickman-Lewis, K., Johnson, J. R., Kah, L. C., Kelemen, P. B., Kinch,

K. B., Mandon, L., Mangold, N., Quantin-Nataf, C., Rice, M. S., Russell, P. S., Sharma, S., Siljeström, S., Steele, A., Sullivan, R., Wadhwa, M., Weiss, B. P., Williams, A. J., Wogsland, B. V., Willis, P. A., Acosta-Maeda, T. A., Beck, P., Benzerara, K., Bernard, S., Burton, A. S., Cardarelli, E. L., Chide, B., Clavé, E., Cloutis, E. A., Cohen, B. A., Czaja, A. D., Debaille, V., Dehouck, E., Fairén, A. G., Flannery, D. T., Fleron, S. Z., Fouchet, T., Frydenvang, J., Garczynski, B. J., Gibbons, E. F., Hausrath, E. M., Hayes, A. G., Henneke, J., Jørgensen, J. L., Kelly, E. M., Lasue, J., Le Mouélic, S., Madariaga, J. M., Maurice, S., Merusi, M., Meslin, P.-Y., Milkovich, S. M., Million, C. C., Moeller, R. C., Núñez, J. I., Ollila, A. M., Paar, G., Paige, D. A., Pedersen, D. A. K., Pilleri, P., Pilorget, C., Pinet, P. C., Rice, J. W., Royer, C., Sautter, V., Schulte, M., Sephton, M. A., Sharma, S. K., Sholes, S. F., Spanovich, N., St. Clair, M., Tate, C. D., Uckert, K., VanBommel, S. J., Yanchilina, A. G., and Zorzano, M.-P. (2022). Aqueously altered igneous rocks sampled on the floor of Jezero crater, Mars. Science, 377(6614):eabo2196. Publisher: American Association for the Advancement of Science.

Fassett, C. I. and Head III, J. W. (2008). Valley network-fed, open-basin lakes on Mars: Distribution and implications for Noachian surface and subsurface hydrology. Icarus, 198(1):37–56. ISBN: 0019-1035 Publisher: Elsevier.

Fastook, J. L. and Head, J. W. (2015). Glaciation in the Late Noachian Icy Highlands: Ice accumulation, distribution, flow rates, basal melting, and top-down melting rates and patterns. Planetary and Space Science, 106:82–98. ISBN: 0032-0633 Publisher: Elsevier.

Fastook, J. L., Head, J. W., Marchant, D. R., Forget, F., and Madeleine, J.-B. (2012). Early Mars climate near the Noachian–Hesperian boundary: Independent evidence for cold conditions from basal melting of the south polar ice sheet (Dorsa Argentea Formation) and implications for valley network formation. Icarus, 219(1):25–40. ISBN: 0019-1035 Publisher: Elsevier.

Feulner, G. (2012). The faint young Sun problem. Reviews of Geophysics, 50(2). _eprint: https://onlinelibrary.wiley.com/doi/pdf/10.1029/2011RG000375.

Flahaut, J., Martinot, M., Bishop, J., Davies, G., and Potts, N. (2017). Remote sensing and in situ mineralogic survey of the chilean salars: An analog to mars evaporate deposits? Icarus, 282:152–173.

Forget, F., Wordsworth, R., Millour, E., Madeleine, J. B., Kerber, L., Leconte, J., Marcq, E., and Haberle, R. M. (2013). 3D modelling of the early martian climate under a denser CO2 atmosphere: Temperatures and CO2 ice clouds. Icarus, 222(1):81–99.

Gallagher, C. J. and Bahia, R. (2021). Outflow channels on mars. In Mars Geological Enigmas, pages 13–40. Elsevier.

Golombek, M. P. (1997). The Mars Pathfinder Mission. Journal of Geophysical Research: Planets, 102(E2):3953–3965. _eprint: https://onlinelibrary.wiley.com/doi/pdf/10.1029/96JE02805.

Goudge, T. A., Fassett, C. I., Head, J. W., Mustard, J. F., and Aureli, K. L. (2016). Insights into surface runoff on early Mars from paleolake basin morphology and stratigraphy. Geology, 44(6):419–422.

Green, R. O., Eastwood, M. L., Sarture, C. M., Chrien, T. G., Aronsson, M., Chippendale, B. J., Faust, J. A., Pavri, B. E., Chovit, C. J., Solis, M., Olah, M. R., and Williams, O. (1998). Imaging Spectroscopy and the Airborne Visible/Infrared Imaging Spectrometer (AVIRIS). Remote Sensing of Environment, 65(3):227–248.

Green, R. O., Mahowald, N., Thompson, D. R., Ung, C., Brodrick, P., Pollock, R., Bennett, M., Lundeen, S., Joyce, M., Olson-Duvall, W., et al. (2023). Performance and early results from the earth surface mineral dust source investigation (emit) imaging spectroscopy mission. In 2023 IEEE aerospace conference, pages 1–10. IEEE.

Grotzinger, J. P., Sumner, D. Y., Kah, L. C., Stack, K., Gupta, S., Edgar, L., Rubin, D., Lewis, K., Schieber, J., Mangold, N., Milliken, R., Conrad, P. G., DesMarais, D., Farmer, J., Siebach, K., Calef, F., Hurowitz, J., McLennan, S. M., Ming, D., Vaniman, D., Crisp, J., Vasavada, A., Edgett, K. S., Malin, M., Blake, D., Gellert, R., Mahaffy, P., Wiens, R. C., Maurice, S., Grant, J. A., Wilson, S., Anderson, R. C., Beegle, L., Arvidson, R., Hallet, B., Sletten, R. S., Rice, M., Bell, J., Griffes, J., Ehlmann, B., Anderson, R. B., Bristow, T. F., Dietrich, W. E., Dromart, G., Eigenbrode, J., Fraeman, A., Hardgrove, C., Herkenhoff, K., Jandura, L., Kocurek, G., Lee, S., Leshin, L. A., Leveille, R., Limonadi, D., Maki, J., McCloskey, S., Meyer, M., Minitti, M., Newsom, H., Oehler, D., Okon, A., Palucis, M., Parker, T., Rowland, S., Schmidt, M., Squyres, S., Steele, A., Stolper, E., Summons, R., Treiman, A., Williams, R., Yingst, A., Team, M. S., Kemppinen, O., Bridges, N., Johnson, J. R., Cremers, D., Godber, A., Wadhwa, M., Wellington, D., McEwan, I., Newman, C., Richardson, M., Charpentier, A., Peret, L., King, P., Blank, J., Weigle, G., Li, S., Robertson, K., Sun, V., Baker, M., Edwards, C., Farley, K., Miller, H., Newcombe, M., Pilorget, C., Brunet, C., Hipkin, V., Leveille, R., Marchand, G., Sanchez, P. S., Favot, L., Cody, G., Fluckiger, L., Lees, D., Nefian, A., Martin, M., Gailhanou, M., Westall, F., Israel, G., Agard, C., Baroukh, J., Donny, C., Gaboriaud, A., Guillemot, P., Lafaille, V., Lorigny, E., Paillet, A., Perez, R., Saccoccio, M., Yana, C., Armiens-Aparicio, C., Rodriguez, J. C., Blazquez, I. C., Gomez, F. G., Gomez-Elvira, J., Hettrich, S., Malvitte, A. L., Jiménez, M. M., Martínez-Frías, J., Martín-Soler, J., Martín-Torres, F. J., Jurado, A. M., Mora-Sotomayor, L., Caro, G. M., Lopez, S. N., Peinado-González, V., Pla-Garcia, J., Manfredi, J. A. R., Romeral-Planelló, J. J., Fuentes, S. A. S., Martinez, E. S., Redondo, J. T., Urqui-O'Callaghan, R., Mier, M.-P. Z., Chipera, S., Lacour, J.-L., Mauchien, P., Sirven, J.-B., Manning, H., Fairen, A., Hayes, A., Joseph, J., Sullivan, R., Thomas, P., Dupont, A., Lundberg, A., Melikechi, N., Mezzacappa, A., DeMarines, J., Grinspoon, D., Reitz, G., Prats, B., Atlaskin, E., Genzer, M., Harri, A.-M., Haukka, H., Kahanpaa, H., Kauhanen, J., Paton, M., Polkko, J., Schmidt, W., Siili, T., Fabre, C., Wray, J., Wilhelm, M. B., Poitrasson, F., Patel, K., Gorevan, S., Indyk, S., Paulsen, G., Bish, D., Gondet, B., Langevin, Y., Geffroy, C., Baratoux, D., Berger, G., Cros, A., d'Uston, C., Forni, O., Gasnault, O., Lasue, J., Lee, Q.-M., Meslin, P.-Y., Pallier, E., Parot, Y., Pinet, P., Schroder, S., Toplis, M., Lewin, E., Brunner, W., Heydari, E., Achilles, C., Sutter, B., Cabane, M., Coscia, D., Szopa, C., Robert, F., Sautter, V., Le Mouelic, S., Nachon, M., Buch, A., Stalport, F., Coll, P., François, P., Raulin, F., Teinturier, S., Cameron, J., Clegg, S., Cousin, A., DeLapp, D., Dingler, R., Jackson, R. S., Johnstone, S., Lanza, N., Little, C., Nelson, T., Williams, R. B., Jones, A., Kirkland, L., Baker, B., Cantor, B., Caplinger, M., Davis, S., Duston, B., Fay, D., Harker, D., Herrera, P., Jensen, E., Kennedy, M. R., Krezoski, G., Krysak, D., Lipkaman, L., McCartney, E., McNair, S., Nixon, B., Posiolova, L., Ravine, M., Salamon, A., Saper, L., Stoiber, K., Supulver, K., Van Beek, J., Van Beek, T., Zimdar, R., French, K. L., Iagnemma, K., Miller, K., Goesmann, F., Goetz, W., Hviid, S., Johnson, M., Lefavor, M., Lyness, E., Breves, E., Dyar, M. D., Fassett, C., Edwards, L., Haberle, R., Hoehler, T., Hollingsworth, J., Kahre, M., Keely, L., McKay, C., Bleacher, L., Brinckerhoff, W., Choi, D., Dworkin, J. P., Floyd, M., Freissinet, C., Garvin, J., Glavin, D., Harpold, D., Martin, D. K., McAdam, A., Pavlov, A., Raaen, E., Smith, M. D., Stern, J., Tan, F., Trainer, M., Posner, A., Voytek, M., Aubrey, A., Behar, A., Blaney, D., Brinza, D., Christensen, L., DeFlores, L.,

Feldman, J., Feldman, S., Flesch, G., Jun, I., Keymeulen, D., Mischna, M., Morookian, J. M., Pavri, B., Schoppers, M., Sengstacken, A., Simmonds, J. J., Spanovich, N., Juarez, M. d. l. T., Webster, C. R., Yen, A., Archer, P. D., Cucinotta, F., Jones, J. H., Morris, R. V., Niles, P., Rampe, E., Nolan, T., Fisk, M., Radziemski, L., Barraclough, B., Bender, S., Berman, D., Dobrea, E. N., Tokar, R., Cleghorn, T., Huntress, W., Manhès, G., Hudgins, J., Olson, T., Stewart, N., Sarrazin, P., Vicenzi, E., Bullock, M., Ehresmann, B., Hamilton, V., Hassler, D., Peterson, J., Rafkin, S., Zeitlin, C., Fedosov, F., Golovin, D., Karpushkina, N., Kozyrev, A., Litvak, M., Malakhov, A., Mitrofanov, I., Mokrousov, M., Nikiforov, S., Prokhorov, V., Sanin, A., Tretyakov, V., Varenikov, A., Vostrukhin, A., Kuzmin, R., Clark, B., Wolff, M., Botta, O., Drake, D., Bean, K., Lemmon, M., Schwenzer, S. P., Lee, E. M., Sucharski, R., Hernandez, M. A. d. P., Avalos, J. J. B., Ramos, M., Kim, M.-H., Malespin, C., Plante, I., Muller, J.-P., Navarro-González, R., Ewing, R., Boynton, W., Downs, R., Fitzgibbon, M., Harshman, K., Morrison, S., Kortmann, O., Williams, A., Lugmair, G., Wilson, M. A., Jakosky, B., Balic-Zunic, T., Frydenvang, J., Jensen, J. K., Kinch, K., Koefoed, A., Madsen, M. B., Stipp, S. L. S., Boyd, N., Campbell, J. L., Perrett, G., Pradler, I., VanBommel, S., Jacob, S., Owen, T., Savijärvi, H., Boehm, E., Böttcher, S., Burmeister, S., Guo, J., Köhler, J., García, C. M., Mueller-Mellin, R., Wimmer-Schweingruber, R., Bridges, J. C., McConnochie, T., Benna, M., Franz, H., Bower, H., Brunner, A., Blau, H., Boucher, T., Carmosino, M., Atreya, S., Elliott, H., Halleaux, D., Rennó, N., Wong, M., Pepin, R., Elliott, B., Spray, J., Thompson, L., Gordon, S., Ollila, A., Williams, J., Vasconcelos, P., Bentz, J., Nealson, K., Popa, R., Moersch, J., Tate, C., Day, M., Francis, R., McCullough, E., Cloutis, E., ten Kate, I. L., Scholes, D., Slavney, S., Stein, T., Ward, J., Berger, J., and Moores, J. E. (2014). A Habitable Fluvio-Lacustrine Environment at Yellowknife Bay, Gale Crater, Mars. Science, 343(6169):1242777. Publisher: American Association for the Advancement of Science.

Gulick, V. C. and Baker, V. R. (1989). Fluvial valleys and martian palaeoclimates. Nature, 341(6242):514–516. Number: 6242 Publisher: Nature Publishing Group.

Hansen, C. J., Castillo-Rogez, J., Grundy, W., Hofgartner, J. D., Martin, E. S., Mitchell, K., Nimmo, F., Nordheim, T. A., Paty, C., Quick, L. C., Roberts, J. H., Runyon, K., Schenk, P., Stern, A., and Umurhan, O. (2021). Triton: Fascinating Moon, Likely Ocean World, Compelling Destination! The Planetary Science Journal, 2(4):137.

Harrell, J. A. and Brown, V. M. (1992). The World's Oldest Surviving Geological Map: The 1150 B.C. Turin Papyrus from Egypt. Journal of Geology, 100:3–18.

Hartmann, W. K. and Neukum, G. (2001). Cratering Chronology and the Evolution of Mars. In Kallenbach, R., Geiss, J., and Hartmann, W. K., editors, Chronology and Evolution of Mars, Space Sciences Series of ISSI, pages 165–194, Dordrecht. Springer Netherlands.

Head, J. W. and Marchant, D. R. (2008). Evidence for Non-Polar Ice Deposits in the Past History of Mars. page 1295. Conference Name: 39th Annual Lunar and Planetary Science Conference ADS Bibcode: 2008LPI....39.1295H.

Head, J. W., Wordsworth, R., Forget, F., Madeleine, J. B., and Halevy, I. (2014). Late Noachian "Cold and Icy Highlands" Model: Geological Predictions for Equilibrium Environments and Equilibrium/Non-Equilibrium Melting Scenarios. page 1412. Conference Name: 45th Annual Lunar and Planetary Science Conference ADS Bibcode: 2014LPI....45.1412H.

Heydari, E., Schroeder, J. F., Calef, F. J., Parker, T. J., and Fairen, A. G. (2023). Lacustrine sedimentation by powerful storm waves in Gale crater and its implications for a warming episode on Mars. Scientific Reports, 13(1):18715. Number: 1 Publisher: Nature Publishing Group.

Hobley, D. E. J., Adams, J. M., Nudurupati, S. S., Hutton, E. W. H., Gasparini, N. M., Istanbulluoglu, E., and Tucker, G. E. (2017). Creative computing with Landlab: an open-source toolkit for building, coupling, and exploring two-dimensional numerical models of Earth-surface dynamics. Earth Surface Dynamics, 5(1):21–46. Publisher: Copernicus GmbH.

Hoke, M. R. T. and Hynek, B. M. (2009). Roaming zones of precipitation on ancient Mars as recorded in valley networks. Journal of Geophysical Research: Planets, 114(E8). _eprint: https://onlinelibrary.wiley.com/doi/pdf/10.1029/2008JE003247.

Hoke, M. R. T., Hynek, B. M., and Tucker, G. E. (2011). Formation timescales of large Martian valley networks. Earth and Planetary Science Letters, 312(1):1–12.

Howard, A. D. (1994). A detachment-limited model of drainage basin evolution. Water resources research, 30(7):2261–2285.

Hurowitz, J. A., Grotzinger, J. P., Fischer, W. W., McLennan, S. M., Milliken, R. E., Stein, N., Vasavada, A. R., Blake, D. F., Dehouck, E., Eigenbrode, J. L., Fairén, A. G., Frydenvang, J., Gellert, R., Grant, J. A., Gupta, S., Herkenhoff, K. E., Ming, D. W., Rampe, E. B., Schmidt, M. E., Siebach, K. L., Stack-Morgan, K., Sumner, D. Y., and Wiens, R. C. (2017). Redox stratification of an ancient lake in Gale crater, Mars. Science, 356(6341):eaah6849. Publisher: American Association for the Advancement of Science.

Hynek, B. M., Arvidson, R. E., and Phillips, R. J. (2002). Geologic setting and origin of Terra Meridiani hematite deposit on Mars. Journal of Geophysical Research: Planets, 107(E10):18–1–18–14. _eprint: https://onlinelibrary.wiley.com/doi/pdf/10.1029/2002JE001891.

Hynek, B. M., Beach, M., and Hoke, M. R. T. (2010). Updated global map of Martian valley networks and implications for climate and hydrologic processes. Journal of Geophysical Research: Planets, 115(E9). _eprint: https://onlinelibrary.wiley.com/doi/pdf/10.1029/2009JE003548.

Hynek, B. M., McCollom, T. M., Marcucci, E. C., Brugman, K., and Rogers, K. L. (2013). Assessment of environmental controls on acid-sulfate alteration at active volcanoes in nicaragua: Applications to relic hydrothermal systems on mars. Journal of Geophysical Research: Planets, 118(10):2083–2104.

Hynek, B. M., Rogers, K. L., Antunovich, M., Avard, G., and Alvarado, G. E. (2018). Lack of microbial diversity in an extreme mars analog setting: Poás volcano, costa rica. Astrobiology, 18(7):923–933.

Irwin III, R. P., Howard, A. D., Craddock, R. A., and Moore, J. M. (2005). An intense terminal epoch of widespread fluvial activity on early Mars: 2. Increased runoff and paleolake development. Journal of Geophysical Research: Planets, 110(E12). _eprint: https://onlinelibrary.wiley.com/doi/pdf/10.1029/2005JE002460.

Ivanov, M. and Head, J. (2001). Chryse planitia, mars: Topographic configuration, outflow channel continuity and sequence, and tests for hypothesized ancient bodies of water using mars orbiter laser altimeter (mola) data. Journal of Geophysical Research: Planets, 106(E2):3275–3295.

Jr, J. A. S., Huff, A. E., Fortezzo, C. M., Gaither, T., Hare, T. M., Hunter, M. A., and Buban, H. (2019). Planetary geologic mapping—Program status and future needs. Technical Report 2019-1012, U.S. Geological Survey. ISSN: 2331-1258 Publication Title: Open-File Report.

Kamada, A., Kuroda, T., Kasaba, Y., Terada, N., Nakagawa, H., and Toriumi, K. (2020). A coupled atmosphere–hydrosphere global climate model of early Mars: A 'cool and wet' scenario for the formation of water channels. Icarus, 338:113567.

Kamps, O. M., Hewson, R. D., van Ruitenbeek, F. J. A., and van der Meer, F. D. (2020). Defining Surface Types of Mars Using Global CRISM Summary Product Maps. Journal of Geophysical Research: Planets, 125(8):e2019JE006337. _eprint: https://agupubs.onlinelibrary.wiley.com/doi/pdf/10.1029/2019JE006337.

Kasting, J. F. (1991). CO2 condensation and the climate of early Mars. Icarus, 94(1):1–13.

Kirsch, M., Lorenz, S., Zimmermann, R., Tusa, L., Möckel, R., Hödl, P., Booysen, R., Khodadadzadeh, M., and Gloaguen, R. (2018). Integration of Terrestrial and Drone-Borne Hyperspectral and Photogrammetric Sensing Methods for Exploration Mapping and Mining Monitoring. Remote Sensing, 10(9):1366. Number: 9 Publisher: Multidisciplinary Digital Publishing Institute.

Kite, E. S., Mayer, D. P., Wilson, S. A., Davis, J. M., Lucas, A. S., and Stucky de Quay, G. (2019). Persistence of intense, climate-driven runoff late in Mars history. Science Advances, 5(3):eaav7710. Publisher: American Association for the Advancement of Science.

Kloos, J. L., Moores, J. E., Godin, P. J., and Cloutis, E. (2021). Illumination conditions within permanently shadowed regions at the lunar poles: Implications for in-situ passive remote sensing. Acta Astronautica, 178:432–451.

Kokaly, R. F., Clark, R. N., Swayze, G. A., Livo, K. E., Hoefen, T., Pearson, N. C., Wise, R., Benzel, W., Lowers, H., Driscoll, R., and Klein, A. (2017). USGS Spectral Library Version 7: U.S. Geological Survey Data Series 1035. page 61.

Kopal, Z. (1969). The earliest maps of the moon. The moon, 1(1):59–66.

Koroleva, A. O., Kassi, S., and Campargue, A. (2022). The water vapor self-continuum absorption at room temperature in the 1.25 um window. Journal of Quantitative Spectroscopy and Radiative Transfer, 286:108206.

Lakdawalla, E. (2018). The Design and Engineering of Curiosity. Springer International Publishing, Cham.

Laura, J. R. and Beyer, R. A. (2021). Knowledge Inventory of Foundational Data Products in Planetary Science. The Planetary Science Journal, 2(1):18. Publisher: IOP Publishing.

Lefort, A., Burr, D. M., Beyer, R. A., and Howard, A. D. (2012). Inverted fluvial features in the Aeolis-Zephyria Plana, western Medusae Fossae Formation, Mars: Evidence for post-formation modification. Journal of Geophysical Research: Planets, 117(E3). _eprint: https://onlinelibrary.wiley.com/doi/pdf/10.1029/2011JE004008.

Logan, R. D., Scherrer, B., Senecal, J., Walton, N. S., Peerlinck, A., Sheppard, J. W., and Shaw, J. A. (2020). Hyperspectral imaging and machine learning for monitoring produce ripeness. In Sensing for Agriculture and Food Quality and Safety XII, volume 11421, pages 95–108. SPIE.

Lorenz, R. D. (2020). How far is far enough? Requirements derivation for planetary mobility systems. Advances in Space Research, 65(5):1383–1401.

Lorenz, R. D., Turtle, E. P., Barnes, J. W., Trainer, M. G., Adams, D. S., Hibbard, K. E., Sheldon, C. Z., Zacny, K., Peplowski, P. N., Lawrence, D. J., Ravine, M. A., McGee, T. G., Sotzen, K. S., MacKenzie, S. M., Langelaan, J. W., Schmitz, S., Wolfarth, L. S., and Bedini, P. D. (2018). Dragonfly: R.D.Lorenzetal. A Rotorcraft Lander Concept for Scientific Exploration at Titan. Johns Hopkins APL Technical Digest, 34(3).

Luo, W. and Stepinski, T. F. (2009). Computer-generated global map of valley networks on Mars. Journal of Geophysical Research: Planets, 114(E11). _eprint: https://onlinelibrary.wiley.com/doi/pdf/10.1029/2009JE003357.

MacKenzie, S. M., Neveu, M., Davila, A. F., Lunine, J. I., Craft, K. L., Cable, M. L., Phillips-Lander, C. M., Hofgartner, J. D., Eigenbrode, J. L., Waite, J. H., Glein, C. R., Gold, R., Greenauer, P. J., Kirby, K., Bradburne, C., Kounaves, S. P., Malaska, M. J., Postberg, F., Patterson, G. W., Porco, C., Núñez, J. I., German, C., Huber, J. A., McKay, C. P., Vera, J.-P. d., Brucato, J. R., and Spilker, L. J. (2021). The Enceladus Orbilander Mission Concept: Balancing Return and Resources in the Search for Life. The Planetary Science Journal, 2(2):77. Publisher: IOP Publishing.

Malin, M. C. and Edgett, K. S. (2003). Evidence for Persistent Flow and Aqueous Sedimentation on Early Mars. Science, 302(5652):1931–1934. Publisher: American Association for the Advancement of Science.

Matese, A., Czarnecki, J. M. P., Samiappan, S., and Moorhead, R. (2024). Are unmanned aerial vehicle-based hyperspectral imaging and machine learning advancing crop science? Trends in Plant Science, 29(2):196–209. Publisher: Elsevier.

McKay, C. P. (2014). Requirements and limits for life in the context of exoplanets. Proceedings of the National Academy of Sciences, 111(35):12628–12633. Publisher: Proceedings of the National Academy of Sciences.

Mier-Hicks, F., Grip, H. F., Kalantari, A., Moreland, S., Pipenberg, B., Keennon, M., Canham, T. K., Pauken, M., Decrossas, E., Tzanetos, T., and Balaram, J. B. (2023). Sample Recovery Helicopter. In 2023 IEEE Aerospace Conference, pages 1–11. ISSN: 1095-323X.

Milkovich, S. M., Stack, K. M., Sun, V. Z., Maxwell, K., Kronyak, R., Schnadt, S. L., Steadman, K., and Spanovich, N. (2022). Balancing Predictive and Reactive Science Planning for Mars 2020 Perseverance. In 2022 IEEE Aerospace Conference (AERO), pages 1–12. ISSN: 1095-323X.

Minkina, W. and Klecha, D. (2016). Atmospheric transmission coefficient modelling in the infrared for thermovision measurements. Journal of sensors and sensor systems, 5(1):17–23.

Mlawer, E. J., Payne, V. H., Moncet, J.-L., Delamere, J. S., Alvarado, M. J., and Tobin, D. C. (2012). Development and recent evaluation of the mt_ckd model of continuum absorption. Philosophical Transactions of the Royal Society A: Mathematical, Physical and Engineering Sciences, 370(1968):2520–2556.

Moon, S., Paige, D. A., Siegler, M. A., and Russell, P. S. (2021). Geomorphic Evidence for the Presence of Ice Deposits in the Permanently Shadowed Regions of Scott-E Crater on the Moon. Geophysical Research Letters, 48(2):e2020GL090780. _eprint: https://onlinelibrary.wiley.com/doi/pdf/10.1029/2020GL090780.

Morgan, A. M., Wilson, S. A., and Howard, A. D. (2022). The global distribution and morphologic characteristics of fan-shaped sedimentary landforms on Mars. Icarus, 385:115137.

Murchie, S., Arvidson, R., Bedini, P., Beisser, K., Bibring, J.-P., Bishop, J., Boldt, J., Cavender, P., Choo, T., Clancy, R. T., Darlington, E. H., Des Marais, D., Espiritu, R., Fort, D., Green, R., Guinness, E., Hayes, J., Hash, C., Heffernan, K., Hemmler, J., Heyler, G., Humm, D., Hutcheson, J., Izenberg, N., Lee, R., Lees, J., Lohr, D., Malaret, E., Martin, T., McGovern, J. A., McGuire, P., Morris, R., Mustard, J., Pelkey, S., Rhodes, E., Robinson, M., Roush, T., Schaefer, E., Seagrave, G., Seelos, F., Silverglate, P., Slavney, S., Smith, M., Shyong, W.-J., Strohbehn, K., Taylor, H., Thompson, P., Tossman, B., Wirzburger, M., and Wolff, M. (2007). Compact Reconnaissance Imaging Spectrometer for Mars (CRISM) on Mars Reconnaissance Orbiter (MRO). Journal of Geophysical Research: Planets, 112(E5). _eprint: https://onlinelibrary.wiley.com/doi/pdf/10.1029/2006JE002682.

Murchie, S. L., Mustard, J. F., Ehlmann, B. L., Milliken, R. E., Bishop, J. L., McKeown, N. K., Noe Dobrea, E. Z., Seelos, F. P., Buczkowski, D. L., Wiseman, S. M., Arvidson, R. E., Wray, J. J., Swayze, G., Clark, R. N., Des Marais, D. J., McEwen, A. S., and Bibring, J.-P. (2009). A synthesis of Martian aqueous mineralogy after 1 Mars year of observations from the Mars Reconnaissance Orbiter. Journal of Geophysical Research: Planets, 114(E2). _eprint: https://onlinelibrary.wiley.com/doi/pdf/10.1029/2009JE003342.

NASEM (2022). Origins, Worlds, and Life: A Decadal Strategy for Planetary Science and Astrobiology 2023-2032. Technical report.

Naß, A., Di, K., Elgner, S., van Gasselt, S., Hare, T., Hargitai, H., Karachevtseva, I., Kersten, E., Manaud, N., Roatsch, T., Rossi, A. P., Skinner Jr., J., and Wählisch, M. (2017). PLANETARY CARTOGRAPHY AND MAPPING: WHERE WE ARE TODAY, AND WHERE WE ARE HEADING FOR? The International Archives of the Photogrammetry, Remote Sensing and Spatial Information Sciences, XLII-3-W1:105–112. Conference Name: ICWG III/II
2017 International Symposium on Planetary Remote Sensing and Mapping (Volume XLII-3/W1) - 13–16 August 2017, Hong Kong Publisher: Copernicus GmbH.

Noe Dobrea, E. Z., Ahrens, C., Banks, M. E., Bell, E., Breitfeld, A., Bristow, T., Candela, A., Clark, R. N., Hansen, M., Hendrix, A., Holsclaw, G., Knightly, P., Kumari, N., Lane, M. D., Martin, A. C., Meier, M. L., Patterson, R. V., Pearson, N. C., Prettyman, T. H., Steckel, A. V., Vijayarangan, S., Vilas, F., Wettergreen, D., and Wright, S. P. (2023). Autonomous Rover Science in the Field: Yellow Cat. 2806:2366. Conference Name: 54th Lunar and Planetary Science Conference ADS Bibcode: 2023LPICo2806.2366N.

OIG (2017). Audit of the Mars 2020 Rover Project. Technical Report IG-17-009, NASA OIG. Section: Audit Reports.

Osinski, G. R., Battler, M., Caudill, C. M., Francis, R., Haltigin, T., Hipkin, V. J., Kerrigan, M., Pilles, E. A., Pontefract, A., Tornabene, L. L., Allard, P., Bakambu, J. N., Balachandran, K., Beaty, D. W., Bednar, D., Bina, A., Bourassa, M., Cao, F., Christoffersen, P., Choe, B.-H.,

Cloutis, E., Cote, K., Cross, M., D'Aoust, B., Draz, O., Dudley, B., Duff, S., Dzamba, T., Fulford, P., Godin, E., Goordial, J., Grau Galofre, A., Haid, T., Harrington, E., Harrison, T., Hawkswell, J., Hickson, D., Hill, P., Innis, L., King, D., Kissi, J., Laughton, J., Li, Y., Lymer, E., Maggiori, C., Maloney, M., Marion, C. L., Maris, J., Mcfadden, S., McLennan, S. M., Mittelholz, A., Morse, Z., Newman, J., O'Callaghan, J., Pascual, A., Patel, P., Picard, M., Pritchard, I., Poitras, J. T., Ryan, C., Sapers, H., Silber, E. A., Simpson, S., Sopoco, R., Svensson, M., Tolometti, G., Uribe, D., Wilks, R., Williford, K. H., Xie, T., and Zylberman, W. (2019). The CanMars Mars Sample Return analogue mission. Planetary and Space Science, 166:110–130.

Osterloo, M. M., Anderson, F. S., Hamilton, V. E., and Hynek, B. M. (2010). Geologic context of proposed chloride-bearing materials on Mars. Journal of Geophysical Research: Planets, 115(E10). _eprint: https://onlinelibrary.wiley.com/doi/pdf/10.1029/2010JE003613.

Palumbo, A. M. and Head, J. W. (2020). Groundwater Release on Early Mars: Utilizing Models and Proposed Evidence for Groundwater Release to Estimate the Required Climate and Subsurface Water Budget. Geophysical Research Letters, 47(8):e2020GL087230. _eprint: https://onlinelibrary.wiley.com/doi/pdf/10.1029/2020GL087230.

Palumbo, A. M., Head, J. W., and Wordsworth, R. D. (2018). Late Noachian Icy Highlands climate model: Exploring the possibility of transient melting and fluvial/lacustrine activity through peak annual and seasonal temperatures. Icarus, 300:261–286.

Pappalardo, R. T., Buratti, B. J., Korth, H., Senske, D. A., Blaney, D. L., Blankenship, D. D., Burch, J. L., Christensen, P. R., Kempf, S., Kivelson, M. G., Mazarico, E., Retherford, K. D., Turtle, E. P., Westlake, J. H., Paczkowski, B. G., Ray, T. L., Kampmeier, J., Craft, K. L., Howell, S. M., Klima, R. L., Leonard, E. J., Matiella Novak, A., Phillips, C. B., Daubar, I. J., Blacksberg, J., Brooks, S. M., Choukroun, M. N., Cochrane, C. J., Diniega, S., Elder, C. M., Ernst, C. M., Gudipati, M. S., Luspay-Kuti, A., Piqueux, S., Rymer, A. M., Roberts, J. H., Steinbrügge, G., Cable, M. L., Scully, J. E. C., Castillo-Rogez, J. C., Hay, H. C. F. C., Persaud, D. M., Glein, C. R., McKinnon, W. B., Moore, J. M., Raymond, C. A., Schroeder, D. M., Vance, S. D., Wyrick, D. Y., Zolotov, M. Y., Hand, K. P., Nimmo, F., McGrath, M. A., Spencer, J. R., Lunine, J. I., Paty, C. S., Soderblom, J. M., Collins, G. C., Schmidt, B. E., Rathbun, J. A., Shock, E. L., Becker, T. C., Hayes, A. G., Prockter, L. M., Weiss, B. P., Hibbitts, C. A., Moussessian, A., Brockwell, T. G., Hsu, H.-W., Jia, X., Gladstone, G. R., McEwen, A. S., Patterson, G. W., McNutt, R. L., Evans, J. P., Larson, T. W., Cangahuala, L. A., Havens, G. G., Buffington, B. B., Bradley, B., Campagnola, S., Hardman, S. H., Srinivasan, J. M., Short, K. L., Jedrey, T. C., St. Vaughn, J. A., Clark, K. P., Vertesi, J., and Niebur, C. (2024). Science Overview of the Europa Clipper Mission. Space Science Reviews, 220(4):40.

Parente, M., Itoh, Y., and Saranathan, A. (2019). New CRISM Data Products for Improved Characterization and Analysis of the Mars2020 Landing Site. In IGARSS 2019 - 2019 IEEE International Geoscience and Remote Sensing Symposium, pages 4911–4914. ISSN: 2153-7003.

Pineau, M., Mathian, M., Baron, F., Rondeau, B., Deit, L. L., Allard, T., and Mangold, N. (2022). Estimating kaolinite crystallinity using near-infrared spectroscopy: Implications for its geology on earth and mars. American Mineralogist, 107(8):1453–1469.

Pollack, J. B., Kasting, J. F., Richardson, S. M., and Poliakoff, K. (1987). The case for a wet, warm climate on early Mars. Icarus, 71(2):203–224.

Ptashnik, I. V., Petrova, T. M., Ponomarev, Y. N., Solodov, A. A., and Solodov, A. M. (2015). Water vapor continuum absorption in near-IR atmospheric windows. Atmospheric and Oceanic Optics, 28(2):115–120.

Ramirez, R. M. and Craddock, R. A. (2018). The geological and climatological case for a warmer and wetter early Mars. Nature Geoscience, 11(4):230–237. Number: 4 Publisher: Nature Publishing Group.

Ramirez, R. M., Craddock, R. A., and Usui, T. (2020). Climate Simulations of Early Mars With Estimated Precipitation, Runoff, and Erosion Rates. Journal of Geophysical Research: Planets, 125(3):e2019JE006160. _eprint: https://onlinelibrary.wiley.com/doi/pdf/10.1029/2019JE006160.

Rencz, A. N. and Ryerson, R. A. (1999). Manual of remote sensing, remote sensing for the earth sciences, volume 3. John Wiley & Sons.

Resonon (2024). Pika IR Hyperspectral Camera.

Roering, J. J., Kirchner, J. W., and Dietrich, W. E. (1999). Evidence for nonlinear, diffusive sediment transport on hillslopes and implications for landscape morphology. Water Resources Research, 35(3):853–870.

Saez, A., Manzo, M., and Ciarcià, M. (2021). Mars Drone Configurations And Approaches to Rotor Design: A Review. In Volume 7A: Dynamics, Vibration, and Control, page V07AT07A046, Virtual, Online. American Society of Mechanical Engineers.

Sautter, V., Toplis, M. J., Beck, P., Mangold, N., Wiens, R., Pinet, P., Cousin, A., Maurice, S., LeDeit, L., Hewins, R., Gasnault, O., Quantin, C., Forni, O., Newsom, H., Meslin, P.-Y., Wray, J., Bridges, N., Payré, V., Rapin, W., and Le Mouélic, S. (2016). Magmatic complexity on early Mars as seen through a combination of orbital, in-situ and meteorite data. Lithos, 254-255:36–52.

Scanlon, K. E., Head, J. W., Madeleine, J.-B., Wordsworth, R. D., and Forget, F. (2013). Orographic precipitation in valley network headwaters: Constraints on the ancient martian atmosphere. Geophysical Research Letters, 40(16):4182–4187.

Schörghofer, N. and Rufu, R. (2023). Past extent of lunar permanently shadowed areas. Science Advances, 9(37):eadh4302.

Seelos, F. P., Seelos, K. D., Murchie, S. L., Novak, M. A. M., Hash, C. D., Morgan, M. F., Arvidson, R. E., Aiello, J., Bibring, J.-P., Bishop, J. L., Boldt, J. D., Boyd, A. R., Buczkowski, D. L., Chen, P. Y., Clancy, R. T., Ehlmann, B. L., Frizzell, K., Hancock, K. M., Hayes, J. R., Heffernan, K. J., Humm, D. C., Itoh, Y., Ju, M., Kochte, M. C., Malaret, E., McGovern, J. A., McGuire, P., Mehta, N. L., Moreland, E. L., Mustard, J. F., Nair, A. H., Núñez, J. I., O'Sullivan, J. A., Packer, L. L., Poffenbarger, R. T., Poulet, F., Romeo, G., Santo, A. G., Smith, M. D., Stephens, D. C., Toigo, A. D., Viviano, C. E., and Wolff, M. J. (2023). The CRISM investigation in Mars orbit: Overview, history, and delivered data products. Icarus, page 115612.

Segura, T. L., Toon, O. B., Colaprete, A., and Zahnle, K. (2002). Environmental Effects of Large Impacts on Mars. Science, 298(5600):1977–1980. Publisher: American Association for the Advancement of Science.

Sheppard, R. Y., Thorpe, M. T., Fraeman, A. A., Fox, V. K., and Milliken, R. E. (2021). Merging Perspectives on Secondary Minerals on Mars: A Review of Ancient Water-Rock Interactions in Gale Crater Inferred from Orbital and In-Situ Observations. Minerals, 11(9):986. Number: 9 Publisher: Multidisciplinary Digital Publishing Institute.

Smith, D. E., Zuber, M. T., Frey, H. V., Garvin, J. B., Head, J. W., Muhleman, D. O., Pettengill, G. H., Phillips, R. J., Solomon, S. C., Zwally, H. J., Banerdt, W. B., Duxbury, T. C., Golombek, M. P., Lemoine, F. G., Neumann, G. A., Rowlands, D. D., Aharonson, O., Ford, P. G., Ivanov, A. B., Johnson, C. L., McGovern, P. J., Abshire, J. B., Afzal, R. S., and Sun, X. (2001). Mars Orbiter Laser Altimeter: Experiment summary after the first year of global mapping of Mars. Journal of Geophysical Research: Planets, 106(E10):23689–23722. _eprint: https://onlinelibrary.wiley.com/doi/pdf/10.1029/2000JE001364.

Sopegno, L., Martini, S., Pedone, S., Fagiolini, A., Rutherford, M. J., Stefanovic, M., Rizzo, A., Livreri, P., and Valavanis, K. P. (2024). An Advanced Hexacopter for Mars Exploration: Attitude Control and Autonomous Navigation. IEEE Transactions on Aerospace and Electronic Systems, pages 1–14. Conference Name: IEEE Transactions on Aerospace and Electronic Systems.

Soto, A., Mischna, M., Schneider, T., Lee, C., and Richardson, M. (2015). Martian atmospheric collapse: Idealized GCM studies. Icarus, 250:553–569.

Squyres, S. W. (2005). Roving Mars: Spirit, Opportunity, and the exploration of the red planet. Hyperion, New York, 1st ed edition. OCLC: ocm61156249.

Squyres, S. W., Arvidson, R. E., Bell, J. F., Brückner, J., Cabrol, N. A., Calvin, W., Carr, M. H., Christensen, P. R., Clark, B. C., Crumpler, L., Marais, D. J. D., d'Uston, C., Economou, T., Farmer, J., Farrand, W., Folkner, W., Golombek, M., Gorevan, S., Grant, J. A., Greeley, R., Grotzinger, J., Haskin, L., Herkenhoff, K. E., Hviid, S., Johnson, J., Klingelhöfer, G., Knoll, A. H., Landis, G., Lemmon, M., Li, R., Madsen, M. B., Malin, M. C., McLennan, S. M., McSween, H. Y., Ming, D. W., Moersch, J., Morris, R. V., Parker, T., Rice, J. W., Richter, L., Rieder, R., Sims, M., Smith, M., Smith, P., Soderblom, L. A., Sullivan, R., Wänke, H., Wdowiak, T., Wolff, M., and Yen, A. (2004). The Opportunity Rover's Athena Science Investigation at Meridiani Planum, Mars. Science, 306(5702):1698–1703. Publisher: American Association for the Advancement of Science.

Steckel, A. V., Clark, R. N., Pearson, N. C., Buxner, S., Prettyman, T. H., Kumari, N., Meier, M. L., Ahrens, C. J., Martin, A. C., Patterson, R. V., Lane, M., Vilas, F., Knightly, P., Wettergreen, D., Banks, M. E., Bell, E., Wright, S. P., Noe Dobrea, E. Z., and Hendrix, A. (2023). Utilizing a Hyperspectral Camera for Field Surveys During the TREX Field Mission. 2806:2720. Conference Name: 54th Lunar and Planetary Science Conference ADS Bibcode: 2023LPICo2806.2720S.

Steckel, A. V., Clark, R. N., Prettyman, T. H., Kumari, N., Meier, M. L., Pearson, N. C., Ahrens, C. J., Martin, A. C., Patterson, R. V., Lane, M., Vilas, F., Knightly, P., Wettergreen, D., Banks, M. E., Bell, E., Wright, S. P., Noe Dobrea, E. Z., and Hendrix, A. (2024a). Mineral Identification Using Tetracorder During the TREX Field Campaign. 3040:2793. Conference Name: LPI Contributions ADS Bibcode: 2024LPICo3040.2793S.

Steckel, A. V., Conrad, J. W., Dekarske, J., Dolan, S., Downey, B., Felton, R., Giesche, A., Hanson, L. E., Horvath, T., Maxwell, R., Shumway, A. O., Siddique, A. A., Strom, C., Teece, B. L., Todd, J., Trinh, K. T., Velez, M. A., Walter, C. A., Lowes, L., Hudson, T. L., and Scully, J. E. C.

(2024b). The Science Case for Nautilus: A Multi-Flyby Mission Concept to Triton. 3040:1173. Conference Name: LPI Contributions ADS Bibcode: 2024LPICo3040.1173S.

Strahler, A. (1957). Quantitative analysis of watershed geomorphology. Eos, Transactions American Geophysical Union, 38(6):913–920. _eprint: https://onlinelibrary.wiley.com/doi/pdf/10.1029/TR038i006p00913.

Swayze, G., Clark, R. N., Kruse, F., Sutley, S., and Gallagher, A. (1992). Ground-truthing aviris mineral mapping at cuprite, nevada. In JPL, Summaries of the Third Annual JPL Airborne Geoscience Workshop. Volume 1: AVIRIS Workshop.

Swayze, G., Desborough, G., Smith, K., Lowers, H., Hammarstrom, J., Diehl, S., Leinz, R., and Driscoll, R. (2008). Understanding Jarosite-From mine waste to Mars, volume 1328, pages 8–13.

Swayze, G. A., Clark, R. N., Goetz, A. F., Livo, K. E., Breit, G. N., Kruse, F. A., Sutley, S. J., Snee, L. W., Lowers, H. A., Post, J. L., Stoffregen, R. E., and Ashley, R. P. (2014). Mapping Advanced Argillic Alteration at Cuprite, Nevada, Using Imaging Spectroscopy. Economic Geology, 109(5):1179–1221.

Swayze, G. A., Clark, R. N., Goetz, A. F. H., Chrien, T. G., and Gorelick, N. S. (2003). Effects of spectrometer band pass, sampling, and signal-to-noise ratio on spectral identification using the Tetracorder algorithm. Journal of Geophysical Research: Planets, 108(E9). _eprint: https://onlinelibrary.wiley.com/doi/pdf/10.1029/2002JE001975.

Swayze, G. A., Clark, R. N., Sutley, S. J., Gent, C. A., Rockwell, B. W., Blaney, D. L., Post, J. L., Farm, B. P., and Green, R. (2002). Mineral mapping mauna kea and mauna loa shield volcanos on hawaii using aviris data and the usgs tetracorder spectral identification system: Lessons applicable to the search for relict martian hydrothermal systems. In Proceedings of the 11th JPL airborne earth science workshop, pages 03–4. Jet Propulsion Laboratory Publication 03-4.

Tanaka, K. L. and Kolb, E. J. (2001). Geologic History of the Polar Regions of Mars Based on Mars Global Surveyor Data: I. Noachian and Hesperian Periods. Icarus, 154(1):3–21.

Thompson, D. R., Braverman, A., Brodrick, P. G., Candela, A., Carmon, N., Clark, R. N., Connelly, D., Green, R. O., Kokaly, R. F., Li, L., et al. (2020a). Quantifying uncertainty for remote spectroscopy of surface composition. Remote Sensing of Environment, 247:111898.

Thompson, D. R., Braverman, A., Brodrick, P. G., Candela, A., Carmon, N., Clark, R. N., Connelly, D., Green, R. O., Kokaly, R. F., Li, L., Mahowald, N., Miller, R. L., Okin, G. S., Painter, T. H., Swayze, G. A., Turmon, M., Susilouto, J., and Wettergreen, D. S. (2020b). Quantifying uncertainty for remote spectroscopy of surface composition. Remote Sensing of Environment, 247:111898.

Tonasso, R., Tataru, D., Rauch, H., Pozsgay, V., Pfeiffer, T., Uythoven, E., and Rodríguez-Martínez, D. (2024). A lunar reconnaissance drone for cooperative exploration and high-resolution mapping of extreme locations. Acta Astronautica, 218:1–17.

Tucker, G. E., Hobley, D. E., Hutton, E., Gasparini, N. M., Istanbulluoglu, E., Adams, J. M., and Nudurupati, S. S. (2015). Celllab-cts 2015: a python library for continuous-time stochastic cellular automaton modeling using landlab. Geoscientific Model Development Discussions, 8(11):9507–9552.

Tzanetos, T., Aung, M., Balaram, J., Grip, H. F., Karras, J. T., Canham, T. K., Kubiak, G., Anderson, J., Merewether, G., and Starch, M. (2022). Ingenuity mars helicopter: From technology demonstration to extraterrestrial scout. In 2022 IEEE Aerospace Conference (AERO), pages 01–19. IEEE.

van der Meero, F. and Bakker, W. (1997). Cross correlogram spectral matching: application to surface mineralogical mapping by using aviris data from cuprite, nevada. Remote sensing of environment, 61(3):371–382.

Vane, G., Green, R. O., Chrien, T. G., Enmark, H. T., Hansen, E. G., and Porter, W. M. (1993). The airborne visible/infrared imaging spectrometer (AVIRIS). Remote Sensing of Environment, 44(2):127–143.

Vaniman, D. T., Bish, D., Ming, D., Bristow, T., Morris, R., Blake, D., Chipera, S., Morrison, S., Treiman, A., Rampe, E., et al. (2014). Mineralogy of a mudstone at yellowknife bay, gale crater, mars. science, 343(6169):1243480.

Vaz, D. A., Di Achille, G., Hynek, B. M., Nelson, W., and Williams, R. M. E. (2020). Martian fan deposits: Insights on depositional processes and origin from mass balance survey. Earth and Planetary Science Letters, 533:116049.

Viviano, C. E., Seelos, F. P., Murchie, S. L., Kahn, E. G., Seelos, K. D., Taylor, H. W., Taylor, K., Ehlmann, B. L., Wiseman, S. M., Mustard, J. F., and Morgan, M. F. (2014). Revised CRISM spectral parameters and summary products based on the currently detected mineral diversity on Mars. Journal of Geophysical Research: Planets, 119(6):1403–1431. _eprint: https://agupubs.onlinelibrary.wiley.com/doi/pdf/10.1002/2014JE004627.

Warren-Rhodes, K., Cabrol, N. A., Phillips, M., Tebes-Cayo, C., Kalaitzis, F., Ayma, D., Demergasso, C., Chong-Diaz, G., Lee, K., Hinman, N., et al. (2023). Orbit-to-ground framework to decode and predict biosignature patterns in terrestrial analogues. Nature Astronomy, 7(4):406–422.

Weiss, D. K. and Head, J. W. (2015). Crater degradation in the noachian highlands of mars: Assessing the hypothesis of regional snow and ice deposits on a cold and icy early mars. Planetary and Space Science, 117:401–420.

Whipple, K. X. and Tucker, G. E. (1999). Dynamics of the stream-power river incision model: Implications for height limits of mountain ranges, landscape response timescales, and research needs. Journal of Geophysical Research: Solid Earth, 104(B8):17661–17674. _eprint: https://onlinelibrary.wiley.com/doi/pdf/10.1029/1999JB900120.

Whiting, C. E. (2023). Estimating the Next Gen RTG Mod 1 Performance Based on Analysis of the New Horizons Mission. In 2023 IEEE Aerospace Conference, pages 1–7, Big Sky, MT, USA. IEEE.

Williams, R. M. E., Grotzinger, J. P., Dietrich, W. E., Gupta, S., Sumner, D. Y., Wiens, R. C., Mangold, N., Malin, M. C., Edgett, K. S., Maurice, S., Forni, O., Gasnault, O., Ollila, A., Newsom, H. E., Dromart, G., Palucis, M. C., Yingst, R. A., Anderson, R. B., Herkenhoff, K. E., Le Mouelic, S., Goetz, W., Madsen, M. B., Koefoed, A., Jensen, J. K., Bridges, J. C., Schwenzer, S. P., Lewis, K. W., Stack, K. M., Rubin, D., Kah, L. C., Bell, J. F., Farmer, J. D., Sullivan,

R., Van Beek, T., Blaney, D. L., Pariser, O., Deen, R. G., MSL Science Team, Kemppinen, O., Bridges, N., Johnson, J. R., Minitti, M., Cremers, D., Edgar, L., Godber, A., Wadhwa, M., Wellington, D., McEwan, I., Newman, C., Richardson, M., Charpentier, A., Peret, L., King, P., Blank, J., Weigle, G., Schmidt, M., Li, S., Milliken, R., Robertson, K., Sun, V., Baker, M., Edwards, C., Ehlmann, B., Farley, K., Griffes, J., Miller, H., Newcombe, M., Pilorget, C., Rice, M., Siebach, K., Stolper, E., Brunet, C., Hipkin, V., Léveillé, R., Marchand, G., Sobrón Sánchez, P., Favot, L., Cody, G., Steele, A., Flückiger, L., Lees, D., Nefian, A., Martin, M., Gailhanou, M., Westall, F., Israel, G., Agard, C., Baroukh, J., Donny, C., Gaboriaud, A., Guillemot, P., Lafaille, V., Lorigny, E., Paillet, A., Pérez, R., Saccoccio, M., Yana, C., Aparicio, C. A., Caride Rodríguez, J., Carrasco Blázquez, I., Gomez Gomez, F., Elvira, J. G., Hettrich, S., Lepinette Malvitte, A., Marín Jiménez, M., Frías, J. M., Soler, J. M., Torres, F. J. M., Molina Jurado, A., Sotomayor, L. M., Munoz Caro, G., Navarro López, S., Gonzalez, V. P., García, J. P., Rodriguez Manfredi, J. A., Planelló, J. J. R., Alejandra Sans Fuentes, S., Sebastian Martinez, E., Torres Redondo, J., O'Callaghan, R. U., Zorzano Mier, M.-P., Chipera, S., Lacour, J.-L., Mauchien, P., Sirven, J.-B., Manning, H., Fairén, A., Hayes, A., Joseph, J., Squyres, S., Thomas, P., Dupont, A., Lundberg, A., Melikechi, N., Mezzacappa, A., DeMarines, J., Grinspoon, D., Reitz, G., Prats, B., Atlaskin, E., Genzer, M., Harri, A.-M., Haukka, H., Kahanpaa, H., Kauhanen, J., Paton, M., Polkko, J., Schmidt, W., Siili, T., Fabre, C., Wray, J., Wilhelm, M. B., Poitrasson, F., Patel, K., Gorevan, S., Indyk, S., Paulsen, G., Bish, D., Schieber, J., Gondet, B., Langevin, Y., Geffroy, C., Baratoux, D., Berger, G., Cros, A., Uston, C. d., Lasue, J., Lee, Q.-M., Meslin, P.-Y., Pallier, E., Parot, Y., Pinet, P., Schroder, S., Toplis, M., Lewin, E., Brunner, W., Heydari, E., Achilles, C., Oehler, D., Sutter, B., Cabane, M., Coscia, D., Szopa, C., Robert, F., Sautter, V., Nachon, M., Buch, A., Stalport, F., Coll, P., Francois, P., Raulin, F., Teinturier, S., Cameron, J., Clegg, S., Cousin, A., DeLapp, D., Dingler, R., Jackson, R. S., Johnstone, S., Lanza, N., Little, C., Nelson, T., Williams, R. B., Jones, A., Kirkland, L., Treiman, A., Baker, B., Cantor, B., Caplinger, M., Davis, S., Duston, B., Fay, D., Hardgrove, C., Harker, D., Herrera, P., Jensen, E., Kennedy, M. R., Krezoski, G., Krysak, D., Lipkaman, L., McCartney, E., McNair, S., Nixon, B., Posiolova, L., Ravine, M., Salamon, A., Saper, L., Stoiber, K., Supulver, K., Van Beek, J., Zimdar, R., French, K. L., Iagnemma, K., Miller, K., Summons, R., Goesmann, F., Hviid, S., Johnson, M., Lefavor, M., Lyness, E., Breves, E., Dyar, M. D., Fassett, C., Blake, D. F., Bristow, T., DesMarais, D., Edwards, L., Haberle, R., Hoehler, T., Hollingsworth, J., Kahre, M., Keely, L., McKay, C., Bleacher, L., Brinckerhoff, W., Choi, D., Conrad, P., Dworkin, J. P., Eigenbrode, J., Floyd, M., Freissinet, C., Garvin, J., Glavin, D., Harpold, D., Mahaffy, P., Martin, D. K., McAdam, A., Pavlov, A., Raaen, E., Smith, M. D., Stern, J., Tan, F., Trainer, M., Meyer, M., Posner, A., Voytek, M., Anderson, R. C., Aubrey, A., Beegle, L. W., Behar, A., Brinza, D., Calef, F., Christensen, L., Crisp, J. A., DeFlores, L., Feldman, J., Feldman, S., Flesch, G., Hurowitz, J., Jun, I., Keymeulen, D., Maki, J., Mischna, M., Morookian, J. M., Parker, T., Pavri, B., Schoppers, M., Sengstacken, A., Simmonds, J. J., Spanovich, N., de la Torre Juarez, M., Vasavada, A. R., Webster, C. R., Yen, A., Archer, P. D., Cucinotta, F., Jones, J. H., Ming, D., Morris, R. V., Niles, P., Rampe, E., Nolan, T., Fisk, M., Radziemski, L., Barraclough, B., Bender, S., Berman, D., Dobrea, E. N., Tokar, R., Vaniman, D., Leshin, L., Cleghorn, T., Huntress, W., Manhès, G., Hudgins, J., Olson, T., Stewart, N., Sarrazin, P., Grant, J., Vicenzi, E., Wilson, S. A., Bullock, M., Ehresmann, B., Hamilton, V., Hassler, D., Peterson, J., Rafkin, S., Zeitlin, C., Fedosov, F., Golovin, D., Karpushkina, N., Kozyrev, A., Litvak, M., Malakhov, A., Mitrofanov, I., Mokrousov, M., Nikiforov, S., Prokhorov, V., Sanin, A., Tretyakov, V., Varenikov, A., Vostrukhin, A., Kuzmin, R., Clark, B., Wolff, M., McLennan, S., Botta, O., Drake, D., Bean, K., Lemmon, M., Lee, E. M., Sucharski, R., Hernandez, M. A. d. P., Blanco Avalos, J. J.,

Ramos, M., Kim, M.-H., Malespin, C., Plante, I., Muller, J.-P., Gonzalez, R. N., Ewing, R., Boynton, W., Downs, R., Fitzgibbon, M., Harshman, K., Morrison, S., Kortmann, O., Williams, A., Lugmair, G., Wilson, M. A., Jakosky, B., Zunic, T. B., Frydenvang, J., Kinch, K., Stipp, S. L. S., Boyd, N., Campbell, J. L., Gellert, R., Perrett, G., Pradler, I., VanBommel, S., Jacob, S., Owen, T., Rowland, S., Savijarvi, H., Boehm, E., Bottcher, S., Burmeister, S., Guo, J., Kohler, J., Garcia, C. M., Mellin, R. M., Schweingruber, R. W., McConnochie, T., Benna, M., Franz, H., Bower, H., Brunner, A., Blau, H., Boucher, T., Carmosino, M., Atreya, S., Elliott, H., Halleaux, D., Renno, N., Wong, M., Pepin, R., Elliott, B., Spray, J., Thompson, L., Gordon, S., Williams, J., Vasconcelos, P., Bentz, J., Nealson, K., Popa, R., Moersch, J., Tate, C., Day, M., Kocurek, G., Hallet, B., Sletten, R., Francis, R., McCullough, E., Cloutis, E., ten Kate, I. L., Arvidson, R., Fraeman, A., Scholes, D., Slavney, S., Stein, T., Ward, J., Berger, J., and Moores, J. E. (2013). Martian Fluvial Conglomerates at Gale Crater. Science, 340(6136):1068–1072. Publisher: American Association for the Advancement of Science.

Wolman, M. G. and Miller, J. P. (1960). Magnitude and frequency of forces in geomorphic processes. The Journal of Geology, 68(1):54–74.

Wordsworth, R., Forget, F., Millour, E., Head, J. W., Madeleine, J. B., and Charnay, B. (2013). Global modelling of the early martian climate under a denser CO2 atmosphere: Water cycle and ice evolution. Icarus, 222(1):1–19.

Wordsworth, R., Kalugina, Y., Lokshtanov, S., Vigasin, A., Ehlmann, B., Head, J., Sanders, C., and Wang, H. (2017). Transient reducing greenhouse warming on early Mars. Geophysical Research Letters, 44(2):665–671. _eprint: https://onlinelibrary.wiley.com/doi/pdf/10.1002/2016GL071766.

Wordsworth, R. D., Kerber, L., Pierrehumbert, R. T., Forget, F., and Head, J. W. (2015). Comparison of "warm and wet" and "cold and icy" scenarios for early Mars in a 3-D climate model. Journal of Geophysical Research: Planets, 120(6):1201–1219. _eprint: https://onlinelibrary.wiley.com/doi/pdf/10.1002/2015JE004787.

Yingst, R. A., Bartley, J. K., Chidsey, T. J., Cohen, B. A., Hynek, B. M., Kah, L. C., Minitti, M. E., Vanden Berg, M. D., Williams, R. M., Adams, M., Black, S., El-Maarry, M. R., Gemperline, J., Kronyak, R., and Lotto, M. (2020). Is a Linear or a Walkabout Protocol More Efficient When Using a Rover to Choose Biologically Relevant Samples in a Small Region of Interest? Astrobiology, 20(3):327–348.

Yingst, R. A., Berger, J., Cohen, B. A., Hynek, B., and Schmidt, M. E. (2017). Determining best practices in reconnoitering sites for habitability potential on Mars using a semi-autonomous rover: A GeoHeuristic Operational Strategies Test. Acta Astronautica, 132:268–281.

Yingst, R. A., Cohen, B. A., Ming, D. W., and Eppler, D. B. (2013). Comparing Apollo and Mars Exploration Rover (MER)/phoenix operations paradigms for human exploration during NASA Desert-RATS science operations. Acta Astronautica, 90(2):311–317.

Zhu, K., Quan, Q., Wang, K., Tang, D., Tang, B., Dong, Y., Wu, Q., and Deng, Z. (2023). Conceptual design and aerodynamic analysis of a Mars octocopter for sample collection. Acta Astronautica, 207:10–23.

Appendix A

Additional details from the TREX field work

A.1 Exploration Scenarios

The rover explored the field site in three different scenarios: 1) standard, 2) fully autonomous, or 3) astronaut/rover collaboration (Candela et al., 2017). In scenario 1, the science team selected stops for each day of exploration, then analyzed the data received and updated their plans. This operational approach is similar to how the rovers are controlled on Mars (Milkovich et al., 2022). In scenario 2, the rover's onboard computer automatically ran Tetracorder to process spectra from the VNIR and FTIR instruments, and used the mineral identifications to update its knowledge of the geologic history and to select the next location autonomously. The science team received this data and used it to interpret the field site, but did not select rover stops. In scenario 3, the rover ran in the same autonomous mode, but there were two astronauts working alongside, who had not seen the field site before. The science team selected stops where the rover and astronauts would meet up, and the astronauts were allowed to communicate their impressions and findings to the science team in addition to the rover data. Astronauts were also allowed to select different stops to collect samples separate from the rover in between these meeting points. Those astronaut samples got the same measurements from all of the hand-held and portable instruments. Each scenario started at the same ''landing site" at the top of the canyon, as shown in Fig. 4.1. This study will focus on the initial 1km region of overlapping rover and hyperspectral data collection as shown in Fig. 4.1, but the rover did explore an additional 3km region to the southeast.

A.1.1 Aligning AVIRIS and PikaIR Datasets

The initial survey for the study was completed with 18m/pixel aerial images from the AVIRIS hyperspectral dataset to map mineralogy with Tetracorder. A reference area to the NW of the Yellow Cat field site was measured by VNIR spectrometer on the day of the flight and used for calibration (to remove artifacts from the reflectance data). This data is part of the dataset used to calibrate AVIRIS data and is a trusted reference for this project (Clark et al., 1998, 2003). The radiative transfer ground calibrated data cube and mineral identification maps of this region were provided Roger Clark and were both used to create the mineral identification maps shown in figure 4.3. These figures were created in python using the SPy spectral library. Since this data set is nearly 30 years old, spatial data was collected separately and is missing from the files. In figure 4.3, the red square is a parking lot located at $38^0 51' 27.74'' N, 109^0 32' 50.38'' W$. This feature was used to manually align the AVIRIS data cube and mineral maps with the sites measured in the field in python. The white square from figure 4.3 indicates rover stop D26, which is hyperspectral imager stop 5 as shown in figure refgeomap.

Appendix B

Full Mineral Identification Results

In the tables below, the mineral column is populated by the file name of the mineral spectra from the USGS library version 7 (Kokaly et al., 2017). Details from some of the mineral mixtures listed can be found in Clark et al. (2007). The average spectrum for each color from Fig. 4.5 and 4.6 is an average of all the pixels of that color, which have been grouped due to their similar spectral features. Tables B.1 - **??** compare the average spectrum to each library mineral in the group (e.g., 1.3, 1.4 or 1.5 μm). The fit parameter r is described in equation 3.5 from chapter 3.

Table B.1: All Mineral Fits from 1.3μm Group in Cliff 1

Mineral	r_{blue}	$r_{lightblue}$	r_{green}
actinolite_hs116.91	1.49	6.39	1.44
actinolite_hs22.105	1.21	6.17	0.89
actinolite_hs315.164	1.33	6.29	0.94
actinolite_nmnh16485.235	1.4	6.41	1.17
actinolite_nmnh80714.223	0.98	6.04	0.83
antigorite_nmnh17958.2782	0.81	5.79	0.24
antigorite_nmnh96917.2797	0.67	5.55	0.17
antigorite_nmnh96917.2813	0.71	5.21	0.24
antigorite_nmnh96917.2876	0.68	5.37	0.21

Table B.1 Continued from previous page

Mineral	r_{blue}	$r_{lightblue}$	r_{green}
antigorite_nmnh96917.2939	0.61	5.41	0.09
antigorite_nmnh96917.3002	0.71	5.36	0.18
antigorite_nmnh96917.3065	0.61	5.02	0.12
chlorite-serpentine_skarn_br93-22b.24951	0.67	2.37	0.62
chlorite_hs179.4691	1.25	4.01	0.73
chlorite_hs197.4745	1.17	2.9	0.91
chlorite_mixture_cu93-4b.24750	0.39	2.86	1.93
chlorite_mixture_cu93-65a.24855	0.48	4.22	2.17
chlorite_phyllite_cu91_238a.24936	0.57	3.34	2.32
chlorite_smr13.4847	1.19	2.73	0.84
chlorite_smr13.4908	1.25	2.66	1.06
chlorite_smr13.4923	1.43	2.98	1.26
chlorite_smr13.4984	1.28	3.03	1.03
chlorite_smr13.5045	1.3	3.23	1.22
chrysotile_hs323.5218	1.73	5.63	1.23
chrysotile_ml99-12a.5230	0.83	4.44	0.3
chrysotile_ml99-12c.5250	1.08	5.22	0.45
clinochlore_gds157.5542	0.49	3.95	1.5
clinochlore_gds157.5556	0.34	3.43	1.02
clinochlore_gds158.5327	0.65	4.27	0.58
clinochlore_gds159.5386	0.73	2.28	0.56
clinochlore_nmnh83369.5444	1.26	3.16	1.21
clinochlore_sc-cca-1.5666	1	2.63	0.66
clinochlore_sc-cca-1.5725	0.57	3.31	0.45

Table B.1 Continued from previous page

Mineral	r_{blue}	$r_{lightblue}$	r_{green}
clinochlore_sc-cca-1.5784	0.45	2.91	1.26
cookeite_car1.6074	0.36	3.57	0.23
cookeite_car1.6131	0.28	3.74	0.32
cookeite_car1.6228	0.28	3.72	0.31
dickite_nmnh106242.6820	0.65	4.01	1.77
dickite_nmnh46967.6913	0.7	4.12	1.93
dick_musc_gyp_jar_amx20.24965	0.57	2.23	1.96
endellite_gds16.7379	0.24	3.36	0.46
kaolinite_cm3.11788	0.2	4.4	0.51
kaolinite_cm5.11846	0.19	4.51	0.52
kaolinite_cm7.11904	0.2	4.36	0.57
kaolinite_cm9.11962	0.18	4.73	0.38
kaolinite_gds11.12060	0.19	4.78	0.43
kaolinite_kga1.12117	0.19	4.7	0.46
kaolinite_kl502.12272	0.24	3.74	0.59
kaolinite_mixture_cu93-5c.25494	0.35	2.41	1.64
kaolinite_muscovite_amx12.25521	0.13	4.73	0.89
kaolinite_pfn1_kga2.12176	0.21	4.29	0.65
kaolinite_wxl+other_cu00-19a.25536	0.16	2.87	0.74
kaolinite_wxl+other_cu91-200a.25557	0.16	3.64	0.68
kaolsmect_h89fr2.25636	0.2	3.04	1.06
kaolsmect_h89fr5.25691	0.3	2.19	1.28
kaolsmect_klf506.25703	0.26	3.47	1
kaolsmect_klf508.25758	0.26	2.59	1.03

Table B.1 Continued from previous page

Mineral	r_{blue}	$r_{lightblue}$	r_{green}
kaolsmect_klf511.25581	0.49	1.79	1.93
kaol_alun_amx14.25812	0.17	2.45	0.83
kaol_musc_amx13.25507	0.16	4.32	1
lepidolite_hs167.12655	0.38	5.83	0.19
lepidolite_nmnh105538.12711	0.19	4.49	1.1
lepidolite_nmnh105541.12766	0.28	4.38	0.98
lepidolite_nmnh88526-1.12832	0.15	4.87	0.84
lizard_nmnhr4687.12941	1.07	5.27	0.57
lizard_nmnhr4687.12954	1.11	4.99	0.58
lizard_nmnhr4687.13011	1.16	5.22	0.64
lizard_nmnhr4687.13068	2.39	3.05	3.89
nacrite_gds88.15578	0.67	4.19	1.76
opal_cu00-15e.26266	0.29	1.69	0.72
opal_tm8896.17216	0.18	1.75	0.92
opal_ws732.17271	0.55	2.01	1.39
paragonite_gds109.17429	0.18	4.82	1.18
phlogopite_gds20.17614	1.66	6.14	1.04
phlogopite_hs23.17673	1.62	5.83	1.01
phlogopite_sand_mix_br93-20.26287	0.67	1.83	2.22
phlogopite_ws496.17731	1.86	5.86	1.33
phlogopite_ws675.17787	1.6	4.54	1.23
pyrophyllite_pys1a.18788	1.34	5.8	0.93
pyrophyllite_pys1a.18885	1.56	6.06	1.35
pyrophyllite_su1421.18941	0.88	4.63	0.63

Table B.1 Continued from previous page

Mineral	r_{blue}	$r_{lightblue}$	r_{green}
pyroph_mont_amx16.26348	0.36	1.72	1.25
richterite_nmnh150800.19500	2.01	6.18	1.8
saponite_sapca1.19977	0.46	1.44	0.76
saponite_sapca1.19990	0.41	2.2	0.51
serpentine_hs318.20395	0.79	5.24	0.33
serpentine_hs8.20407	0.96	5.96	0.32
smaragdite_hs290.20628	0.38	5.73	0.2
talc_clinochl_hs327.26428	1.25	5	0.81
talc_clinochl_hs327.26454	1.62	5.07	1.2
talc_gds23.21499	1.72	5.73	1.56
talc_hs21.21556	1.49	4.72	1.34
talc_tl2702.21613	1.57	5.09	1.47
talc_ws659.21626	1.64	5.17	1.51
tremolite_hs18.23052	2.04	6.35	1.9
tremolite_nmnh117611.23109	2.12	6.39	1.96
uralite_hs345.23325	1.12	5.79	1.48
vermiculite_gds13.23435	0.84	1.3	1.14
vermiculite_vtx-1-flx.23448	0.86	1.34	1.2
vermiculite_vtx-1a.23461	1.12	1	2.51
vermiculite_ws681.23472	0.87	1.81	1.04

Table B.2: All Mineral Fits from the 1.3μm Group in Cliff 2

Mineral	r_{blue}	r_{yellow}	r_{orange}	r_{red}
actinolite_hs116.91	0.36	1.36	1.19	1.79
actinolite_hs22.105	-0.13	0.98	0.58	1.28
actinolite_hs315.164	-6.11	0.84	0.66	1.17
actinolite_nmnh16485.235	-11.46	1.02	0.83	1.61
actinolite_nmnh80714.223	0.23	0.97	0.79	0.64
antigorite_nmnh17958.2782	0.54	0.42	0.04	0.88
antigorite_nmnh96917.2797	1.31	0.5	-0.28	0.43
antigorite_nmnh96917.2813	0.64	0.65	0.11	0.63
antigorite_nmnh96917.2876	0.67	0.47	0.15	0.56
antigorite_nmnh96917.2939	0.58	0.53	-0.47	0
antigorite_nmnh96917.3002	0.44	0.38	-0.09	0.45
antigorite_nmnh96917.3065	0.57	0.58	-0.06	0.56
chlorite-serpentine_skarn_br93-22b.24951	2.31	3.38	0.52	3.66
chlorite_hs179.4691	0.65	2.07	0.52	1.17
chlorite_hs197.4745	1.63	2.4	0.92	2.85
chlorite_mixture_cu93-4b.24750	2.72	3.67	3.12	3.49
chlorite_mixture_cu93-65a.24855	2.82	3.98	3.64	5.47
chlorite_phyllite_cu91_238a.24936	2.85	4.43	4.33	5.74
chlorite_smr13.4847	1.22	2.08	0.64	2.18
chlorite_smr13.4908	1.72	2.58	0.84	2.9
chlorite_smr13.4923	1.42	2.16	1.02	2.52
chlorite_smr13.4984	0.98	1.81	0.61	1.91
chlorite_smr13.5045	1.7	2.67	0.72	3.05
chrysotile_hs323.5218	0.43	1.05	1.22	1.34

Table B.2 Continued from previous page

Mineral	r_{blue}	r_{yellow}	r_{orange}	r_{red}
chrysotile_ml99-12a.5230	0.46	0.61	0.1	0.73
chrysotile_ml99-12c.5250	1.66	0.62	0.38	0.53
clinochlore_gds157.5542	2.3	3.18	-0.48	2.54
clinochlore_gds157.5556	2.17	3.22	-1.04	2.29
clinochlore_gds158.5327	1.45	1.89	0.23	-0.72
clinochlore_gds159.5386	1.93	2.81	0.46	3.06
clinochlore_nmnh83369.5444	1.57	2.42	1.4	2.75
clinochlore_sc-cca-1.5666	2.04	3.41	0.81	3.61
clinochlore_sc-cca-1.5725	1.42	3.4	1.25	1.84
clinochlore_sc-cca-1.5784	2.09	3.65	1.55	1.58
cookeite_car1.6074	1.48	1.98	-0.11	1.83
cookeite_car1.6131	1.57	2.07	0.11	1.88
cookeite_car1.6228	1.33	2.27	-6.67	1.49
dickite_nmnh106242.6820	3.1	4.2	10.48	130.82
dickite_nmnh46967.6913	3.39	6.25	8.51	-7.28
dick_musc_gyp_jar_amx20.24965	3.11	4.92	8.09	15.03
endellite_gds16.7379	1.77	2.37	1.88	1.82
kaolinite_cm3.11788	1.84	2.4	3.67	2.58
kaolinite_cm5.11846	1.83	2.49	4.15	2.4
kaolinite_cm7.11904	1.99	2.75	6.74	-37.12
kaolinite_cm9.11962	1.52	1.88	2.46	1.31
kaolinite_gds11.12060	1.69	2.19	3.53	2.95
kaolinite_kga1.12117	1.72	2.27	3.61	1.83
kaolinite_kl502.12272	1.96	2.82	3.32	2.63

Table B.2 Continued from previous page

Mineral	r_{blue}	r_{yellow}	r_{orange}	r_{red}
kaolinite_mixture_cu93-5c.25494	2.84	4.24	6.26	4.19
kaolinite_muscovite_amx12.25521	2.2	3.23	4.11	1.36
kaolinite_pfn1_kga2.12176	2.06	3.09	45.61	1.99
kaolinite_wxl+other_cu00-19a.25536	2.17	3.02	2.35	2.59
kaolinite_wxl+other_cu91-200a.25557	2.12	2.99	2.6	2.97
kaolsmect_h89fr2.25636	2.55	3.91	4.89	3.81
kaolsmect_h89fr5.25691	2.68	3.88	5.17	3.86
kaolsmect_klf506.25703	2.64	4.63	5.4	4.67
kaolsmect_klf508.25758	2.52	3.96	9.35	3.97
kaolsmect_klf511.25581	2.96	4.28	3.87	4.45
kaol_alun_amx14.25812	2.14	2.9	3.67	2.7
kaol_musc_amx13.25507	2.39	3.58	4.26	11.57
lepidolite_hs167.12655	1.33	1.04	0.35	-0.16
lepidolite_nmnh105538.12711	2.4	3.43	3.05	2.98
lepidolite_nmnh105541.12766	2.27	3.3	1.96	2.86
lepidolite_nmnh88526-1.12832	2.24	3.22	2.86	2.93
lizard_nmnhr4687.12941	0.69	0.62	0.52	0.9
lizard_nmnhr4687.12954	0.86	0.56	0.61	1.03
lizard_nmnhr4687.13011	0.65	0.66	0.55	1.08
lizard_nmnhr4687.13068	3.77	5.97	5.1	6.91
nacrite_gds88.15578	3.18	5.16	6.94	25.12
opal_cu00-15e.26266	2.55	3.63	1.15	3.85
opal_tm8896.17216	2.48	3.48	-1.6	3.42
opal_ws732.17271	6.8	6.79	1.93	6.53

Table B.2 Continued from previous page

Mineral	r_{blue}	r_{yellow}	r_{orange}	r_{red}
paragonite_gds109.17429	2.32	3.36	2.77	2.75
phlogopite_gds20.17614	0.11	0.88	1.27	1.67
phlogopite_hs23.17673	7.09	1.37	0.37	0.81
phlogopite_sand_mix_br93-20.26287	3.04	4.43	3.06	4.67
phlogopite_ws496.17731	0.48	0.96	1.43	1.78
phlogopite_ws675.17787	0.6	1.92	0.84	2.23
pyrophyllite_pys1a.18788	0.44	**0.34**	0.77	0.92
pyrophyllite_pys1a.18885	-2.18	0.87	1.25	1.37
pyrophyllite_su1421.18941	0.46	0.64	0.4	0.73
pyroph_mont_amx16.26348	2.71	3.93	1.85	4.14
richterite_nmnh150800.19500	0.31	1.69	1.75	2.4
saponite_sapca1.19977	2.56	3.68	0.8	3.97
saponite_sapca1.19990	2.06	2.96	0.55	2.95
serpentine_hs318.20395	0.73	0.73	5.4	0.32
serpentine_hs8.20407	0.43	0.45	0.01	0.67
smaragdite_hs290.20628	0.99	0.98	-0.16	0.05
talc_clinochl_hs327.26428	2.31	1.16	0.52	1.47
talc_clinochl_hs327.26454	0.52	1.35	0.85	1.95
talc_gds23.21499	0.55	1.45	1.51	1.94
talc_hs21.21556	0.61	1.44	1.16	1.86
talc_tl2702.21613	0.55	1.37	1.5	1.77
talc_ws659.21626	0.59	1.41	1.63	1.85
tremolite_hs18.23052	0.61	1.7	1.71	2.36
tremolite_nmnh117611.23109	0.62	2.04	2.05	2.05

Table B.2 Continued from previous page

Mineral	r_{blue}	r_{yellow}	r_{orange}	r_{red}
uralite_hs345.23325	-0.51	1.54	1.16	1.56
vermiculite_gds13.23435	2.94	4.31	0.62	4.81
vermiculite_vtx-1-flx.23448	2.93	4.26	0.8	4.77
vermiculite_vtx-1a.23461	3.36	4.84	4.4	5.49
vermiculite_ws681.23472	2.75	3.87	0.93	4.35

Table B.3: All Mineral Fits from the 1.4μm Group in Cliff 1

Mineral	$r_{lightblue}$	r_{red}	r_{yellow}	r_{green}
alunite_al706.966	1.95	9.35	2.32	2.69
alunite_gds82.1063	1.48	4.96	2.06	2.43
alunite_gds83.1079	1.89	8.45	2.32	2.67
alunite_gds84.1175	1.81	7.51	2.27	2.63
alunite_hs295.1388	1.74	7.14	2.23	2.6
alunite_hs295.1411	1.75	6.88	2.34	2.69
alunite_nh4+jar_nmnh145596.24175	1.72	7.59	1.7	2.19
alunite_nh4+jar_nmnh145596.24230	1.64	6.62	1.59	2.09
alunite_sustda20.1702	1.92	8.73	2.34	2.69
analcime_gds1.1930	0.79	1.65	1.62	1.96
clinoptilolite_gds152.5841	0.46	0.88	0.91	1.2
clinoptilolite_gds2.5896	0.4	0.9	0.8	1.11
chrysocolla_hs297.5163	0.26	1	0.36	0.64
cookeite_car1.6074	0.21	1.45	0.44	0.13
cookeite_car1.6131	0.19	1.64	0.35	0.11
cookeite_car1.6228	0.27	2.05	0.32	0.09

Table B.3 Continued from previous page

Mineral	$r_{lightblue}$	r_{red}	r_{yellow}	r_{green}
copiapite_gds21.6285	1.58	5.94	2.06	2.43
elbaite_nmnh94217.7249	1.45	4.04	2.16	2.48
elbaite_nmnh94217.7308	1.45	4.19	2.09	2.42
elbaite_nmnh94217.7367	1.54	4.54	2.1	2.44
eugsterite_gds140.7700	1.26	3.87	1.83	2.22
gibbsite_hs423.8057	1.33	2.17	1.27	1.58
gibbsite_ws214.8111	1.04	2.65	1.3	1.65
gypsum_hs333.8796	1.75	5	2.3	2.65
gypsum_su2202.8850	1.84	5.91	2.3	2.65
gyp_jar_ill_brcm1.25237	0.44	1.92	0.48	0.9
gyp_jar_mus_amx24.25287	1.15	3.62	1.44	1.86
gyp_jar_mus_dic_amx22.25258	0.19	1.92	0.55	0.81
gyp_jar_mus_dic_amx23.25272	0.38	1.2	0.89	1.17
halloysite_cm13.8921	0.07	1.77	0.39	0.14
halloysite_kaolinite_cm29.25328	0.08	2.87	0.36	0.13
halloysite_klh503.8977	0.06	0.93	0.47	0.25
halloysite_nmnh106236.8988	0.06	1.63	0.45	0.2
halloysite_nmnh106237.8999	0.07	2.07	0.44	0.18
hectorite_shca-1.9093	0.14	0.38	0.51	0.33
hectorite_shca-1.9107	0.18	0.34	0.61	0.48
heulandite_gds3.9788	0.47	0.85	0.92	1.18
heulandite_nmnh84534.9843	0.66	1.29	1.24	1.57
hydrogrossular_nmnh120555.10236	0.17	0.6	0.6	0.54
kaolinite_cm3.11788	0.11	5.27	0.34	0.16

Table B.3 Continued from previous page

Mineral	$r_{lightblue}$	r_{red}	r_{yellow}	r_{green}
kaolinite_cm5.11846	0.12	5.51	0.32	0.16
kaolinite_cm7.11904	0.09	5.01	0.35	0.18
kaolinite_cm9.11962	0.16	5.83	0.29	0.11
kaolinite_gds11.12060	0.16	6.03	0.3	0.13
kaolinite_kga1.12117	0.15	5.92	0.3	0.14
kaolinite_kl502.12272	0.07	3.28	0.4	0.21
kaolinite_mixture_cu93-5c.25494	0.11	1.79	0.4	0.55
kaolinite_muscovite_amx12.25521	0.11	5.79	0.16	0.22
kaolinite_pfn1_kga2.12176	0.1	5.1	0.35	0.2
kaolinite_wxl+other_cu00-19a.25536	0.04	1.85	0.28	0.21
kaolinite_wxl+other_cu91-200a.25557	0.06	3.35	0.27	0.19
kaolsmect_h89fr2.25636	0.05	1.94	0.33	0.32
kaolsmect_h89fr5.25691	0.08	0.92	0.41	0.44
kaolsmect_klf506.25703	0.05	3.12	0.36	0.32
kaolsmect_klf508.25758	0.05	1.66	0.4	0.34
kaolsmect_klf511.25581	0.19	0.83	0.51	0.7
kaol_alun_amx14.25812	0.12	1.53	0.34	0.26
kaol_musc_amx13.25507	0.08	4.94	0.23	0.27
laumontite_gds5.12491	0.81	1.56	1.43	1.77
lazurite_hs418.12545	0.94	2.48	1.34	1.74
lepidolite_hs167.12655	0.4	6.86	0.33	0.09
lepidolite_nmnh105538.12711	0.08	4.32	0.25	0.3
lepidolite_nmnh105541.12766	0.08	3.47	0.46	0.33
lepidolite_nmnh88526-1.12832	0.08	5.11	0.22	0.2

Table B.3 Continued from previous page

Mineral	$r_{lightblue}$	r_{red}	r_{yellow}	r_{green}
margarite_gds106.13344	0.52	7.85	0.43	0.94
mizzonite_bm931-12.14023	0.29	3.9	0.25	0.6
mizzonite_hs350.14082	0.96	2.51	1.72	2.1
mizzonite_hs351.14141	0.63	3.74	1.1	1.45
mizzonite_nmnh113775-1.14199	0.98	2.61	1.73	2.11
meionite_ws700.13567	0.55	1.28	1.27	1.54
meionite_ws701.13581	0.7	4.14	0.54	0.91
mordenite_gds151.14796	0.45	1	0.86	1.21
mordenite_gds18.14743	0.49	1.11	0.91	1.28
montmorillonite-Na_cu93-52.25995	0.47	1.28	0.86	1.24
montmorillonite_cm20.14324	0.21	0.56	0.51	0.65
montmorillonite_cm26.14382	0.13	1.21	0.38	0.52
montmorillonite_cm27.14440	0.12	1.02	0.36	0.48
montmorillonite_cm37.25969	0.2	2.78	0.47	0.76
montmorillonite_cm42.25982	0.27	0.9	0.63	0.86
montmorillonite_saz1.14498	0.32	0.85	0.64	0.9
montmorillonite_sca2.14557	0.2	0.62	0.43	0.55
montmorillonite_sca2.14571	0.34	0.98	0.7	0.99
montmorillonite_stx1.14630	0.19	0.73	0.44	0.62
montmorillonite_swy1.14688	0.13	1.51	0.35	0.54
mont_calc_amx15.24629	0.3	0.83	0.64	0.9
muscovite-lowAl_cu98-8h.26121	0.21	3.51	0.41	0.73
muscovite-medhi-Al_CU91-252d.26143	0.16	5.02	0.2	0.46
muscovite-medlow-Al_cu91-250a.26166	0.12	4.59	0.25	0.41

Table B.3 Continued from previous page

Mineral	$r_{lightblue}$	r_{red}	r_{yellow}	r_{green}
muscovite_gds107.14887	0.25	5.85	0.31	0.66
muscovite_gds108.14944	0.28	5.92	0.25	0.64
muscovite_gds111.15002	0.63	5.69	1.12	1.56
muscovite_gds113.15059	0.25	6.46	0.23	0.58
muscovite_gds114.15116	0.37	4.9	0.64	1.05
muscovite_gds116.15173	0.42	5.72	0.74	1.16
muscovite_gds117.15230	0.25	4.83	0.35	0.73
muscovite_gds118.15287	0.47	5.26	0.82	1.24
muscovite_gds119.15344	0.24	3.87	0.4	0.77
muscovite_gds120.15401	0.25	4.05	0.42	0.78
muscovite_hs146.15457	0.31	5.68	0.47	0.86
muscovite_hs24.15512	0.35	5.84	0.58	0.98
muscovite_il107.15566	0.46	5.33	0.77	1.21
muscovite_mix_cu93-314.26008	0.31	3.09	0.46	0.85
nacrite_gds88.15578	0.25	5.9	0.78	0.72
natrolite_hs169.15604	1.62	5.4	2.06	2.44
natrolite_nmnh83380.15659	1.59	4.31	2.11	2.48
natrolite_zeolite_hs168.26211	0.51	1.18	0.83	1.21
nontronite_cu00-13a.26189	0.81	1.61	1.42	1.79
nontronite_ng1.15991	0.64	1.25	1.13	1.47
nontronite_ng1.16050	0.68	1.39	1.24	1.59
nontronite_swa1.16109	0.45	0.92	0.84	1.12
nontronite_swa1.16168	0.49	0.92	0.94	1.23
opal_cu00-15e.26266	0.14	0.29	0.44	0.3

Table B.3 Continued from previous page

Mineral	$r_{lightblue}$	r_{red}	r_{yellow}	r_{green}
opal_tm8896.17216	0.1	0.6	0.26	0.25
opal_ws732.17271	0.9	1.07	0.73	0.64
palygorskite_cm46.17404	0.48	1.28	0.97	1.32
palygorskite_pfl1.17415	0.63	1.5	1.24	1.6
paragonite_gds109.17429	0.16	5.59	0.11	0.3
roscoelite_en124.19682	0.41	2.14	0.85	1.21
sauconite_gds135.20044	0.34	1.11	0.46	0.8
schwertmannite_bz93-1.20097	1.4	5.3	1.91	2.3
scolecite_gds7.20112	1.28	2.62	1.89	2.26
stilbite_gds8.21224	0.39	0.69	0.75	0.96
stilbite_hs482.21279	0.48	0.83	0.86	1.09
topaz_10.22940	0.79	8.99	0.49	0.79
topaz_12.22664	1.06	9.83	0.65	1.01
topaz_13.22719	0.87	9.19	0.48	0.8
topaz_14.22774	0.91	7.98	0.56	0.97
topaz_15.22829	0.75	8.53	0.44	0.77
topaz_16.22884	0.8	8.37	0.44	0.79
topaz_2.22137	0.87	9.49	0.46	0.77
topaz_22.22484	0.86	9.38	0.47	0.79
topaz_3.22416	0.93	9.87	0.55	0.85
topaz_4.22608	0.91	9.28	0.52	0.9
topaz_41.22540	0.86	9.31	0.43	0.85
topaz_42.22081	0.77	8.7	0.5	0.83
topaz_5.22595	0.64	8.85	0.3	0.73

Table B.3 Continued from previous page

Mineral	$r_{lightblue}$	r_{red}	r_{yellow}	r_{green}
topaz_6.22193	0.99	10.02	0.61	0.93
topaz_8.22249	0.82	9.24	0.53	0.78
topaz_9.22429	0.83	7.8	0.61	0.89
topaz_hs184.22304	0.7	8.69	0.33	0.68
tourmaline_hs282.22996	1.72	6.44	2.27	2.62
vermiculite_gds13.23435	0.44	0.85	1.04	0.72
vermiculite_vtx-1-flx.23448	0.43	0.79	1.08	0.76
vermiculite_vtx-1a.23461	0.59	1.57	1.13	1.21
vermiculite_ws681.23472	0.33	0.69	1.02	0.63

Table B.4: All Mineral Fits for the 1.5μm Group in Cliffs 1 and 2

Mineral	Cliff 1 r_{green}	Cliff 2 r_{green}
bloedite_gds147.3703	0.44	0.41
datolite_hs442.6695	1.88	1.94
datolite_su51399.6752	0.97	1.08
gibbsite_hs423.8057	0.88	0.84
gibbsite_ws214.8111	0.29	0.38
jarosite_gds100.11210	0.1	0.16
jarosite_gds101.11265	0.08	0.13
jarosite_gds24.11320	0.09	0.14
jarosite_gds98.11375	0.15	0.24
jarosite_gds99.11469	0.13	0.2
jarosite_jr2501.11562	0.12	0.2
jarosite_nmnh95074-1.11574	0.13	0.21

Table B.4: All Mineral Fits for the 1.5μm Group in Cliffs 1 and 2

Mineral	Cliff 1 r_{green}	Cliff 2 r_{green}
jarosite_pb_ws368.11723	0.16	0.26
jarosite_sj1.11629	0.11	0.18
natrolite_hs169.15604	0.58	0.67
natrolite_nmnh83380.15659	0.37	0.52
natrolite_zeolite_hs168.26211	0.34	0.52
prehnite_gds613.18141	0.28	0.44
prehnite_gds613.18212	0.7	0.78

Appendix C

Python Code

C.1 Display Tetracorder Results

```
# -*- coding: utf-8 -*-
"""
Created on Thu May  2 10:49:59 2024

@author: Amanda Steckel
"""
# Manual Inputs:  Mark only 1 as true
#D26, Cliff1, Cliff2
datalocation=[True,False,False]
#1.3, 1.4, 1.5, 2 micron
mineralgroup=[False,True,False,False]

import numpy as np
import matplotlib as mpl
import matplotlib.pyplot as plt
from featurewav import min_name2,min_name15,min_name14
from featurewav import min_name13,minlist13,minlist14
from featurewav import minlist15,minlist2
from tetfunctions import disptetracorder,avgspectra,continuum_removal
from tetfunctions import isolatefeature,scalefeature,plotscaledabsfits


```

```
23 mpl.rcParams['figure.dpi'] = 300
24 path=r'C:\Users\avste\localdoc\TREXcode'
25
26 # folder from tetracorder run: new6td26, pika1129, newt1601
27 if datalocation[0]:
28     loc=r'\new6td26'
29     datacube=r'C:\Users\avste\localdoc\TREXcode\D26_1458_D-cal4.bil.hdr'
30     datacube_name=r'Cliff 2 '
31     subfol=r'\d26_cal4_extracted_data'
32
33 if datalocation[1]:
34     loc='pika1129'
35     datacube=r'C:\Users\avste\localdoc\TREXcode\20221027_1129_D-cal3.bil.hdr'
36     datacube_name=r'Cliff 1 '
37     subfol=r'\cliff1_extracted_data'
38
39 if datalocation[2]:
40     loc=r'\newt1601'
41     tmppath=r'C:\Users\avste\localdoc\TREXcode'
42     datacube=r'C:\Users\avste\localdoc\TREXcode\20221027_1601_D-cal5crop.bil.hdr'
43     datacube_name=r'Cliff 2 '
44     subfol=r'\cliff2_extracted_data' # folder to put data
45
46 if mineralgroup[0]:
47     min_group=r'\group.1.3-1.4um'
48     min_name=min_name13
49     libmins=minlist13
50     lowerunit=9
51     upperunit=7
52
53 if mineralgroup[1]:
54     min_group=r'\group.1.4um'
55     min_name=min_name14
```

```
56      libmins=minlist14
57      lowerunit=34
58      upperunit=7
59
60  if mineralgroup[2]:
61      min_group=r'\group.1.5um'
62      min_name=min_name15
63      libmins=minlist15
64      lowerunit=6
65      upperunit=7
66
67  if mineralgroup[3]:
68      min_group=r'\group.2um'
69      min_name=min_name2
70      libmins=minlist2
71      lowerunit=4
72      upperunit=5
73
74  # Create dataframe of library spectra
75  from makelib import librarydf
76  librarypath=r'C:\Users\avste\localdoc\TREX\library06\ASCII'
77  num_lib_mins,files,df = librarydf(librarypath)
78
79
80  # type of tetracorder results
81  data_type='.fd'
82  threshold = 10 # change as needed (250)
83
84
85  data,b,matrixcube=disptetracorder(path,loc,min_group,subfol,data_type,
86                                    threshold,min_name,datacube,datacube_name)
87  bands=np.shape(matrixcube)[2]
88  lam=np.linspace(0.89369, 1.71782,bands)
```

```
89
90  good=[]
91  good=np.arange(12,95)
92  good=np.append(good,np.arange(100,163))
93  print('Good Channels: ',good)
94
95  ################ From tetracorder expert system
96  alunite_feature=[1.342,1.456] #group 14 lib228 or lib306
97  kaolinite_feature=[1.25,1.55] #group14 lib672
98  halloysite_feature=[1.26,1.55]#group 14 lib684
99  muscovite_feature=[1.3,1.56] #group 14 lib3336
100 mont1_feature=[1.3,1.57] #group 14 lib588
101 mont2_feature=[1.3,1.61] #group 14 lib3228
102
103 ###################### Pick a mineral group for average spectra ########
104 # Plot Mineral index to check
105 fig,ax=plt.subplots(1,2,figsize=(20,100))
106 ax[0].imshow(b[lowerunit],cmap='jet',vmin=0,vmax=1)
107 ax[0].set_title(min_name[lowerunit],rotation = -90)
108 ax[1].imshow(b[upperunit],cmap='jet',vmin=0,vmax=1)
109 ax[1].set_title(min_name[upperunit],rotation = -90)
110 plt.show()
111
112 mean34=avgspectra(b[lowerunit],bands,matrixcube)
113 mean7=avgspectra(b[7][356:380,125:155],bands,matrixcube)
114
115 good2=np.array([ 12,  13,  14,  15,  16,  17,  18,  19,  20,  21,  22,
116                  23,  24,25,  26,  27,  28,  29,  30,  31,  32,  33,  34,
117                  35,  36,  37,
118         38,  39,  40,  41,  42,  43,  44,  45,  46,  47,  48,  49,  50,
119         51,  52,  53,  54,  55,  56,  57,  58,  59,  60,  61,  62,  63,
120         64,  65,  66,  67,  68,  69,  70,  71,  72,  73,  74,  75,  76,
121         77,  78,  79,  80,  81,  82,  83,  84,  85,  86,  87,  88,  89,
```

```
122          90,  91,  92,  93, 95, 96,97, 98, 99, 100, 101, 102, 103, 104, 105, 106,
                 107, 108,
123         109, 110, 111, 112, 113, 114, 115, 116, 117, 118, 119, 120, 121,
124         122, 123, 124, 125, 126, 127, 128, 129, 130, 131, 132, 133, 134,
125         135, 136, 137, 138, 139, 140, 141, 142, 143, 144, 145, 146, 147,
126         148, 149, 150, 151, 152, 153, 154, 155, 156, 157, 158, 159, 160,
127         161, 162])
128
129 ############### Lower cliff unit, Cliff 1
130 x34,obs34,N34,lib34=isolatefeature(lam,good2,[1.3,1.5],mean34,libmins,df,
131                                     files,min_name,lowerunit)
132 k34=np.zeros(len(libmins))
133 Ls34=[]
134 r34=np.zeros(len(libmins))
135 chi34=np.zeros(len(libmins))
136 coeffs=np.arange(-0.99,0,.01)
137 for i in range(0,len(libmins)):
138     allr=np.zeros(len(coeffs))
139     for j in range(0,len(coeffs)):
140         allr[j]=scalefeature(lib34[i][:,1],lib34[i][:,0],obs34,coeffs[j],
141                              files[libmins[i]],libmins[i],False,False)
142     loc=np.argmin(np.abs(allr))
143
144     chi2,r,Ls=scalefeature(lib34[i][:,1],lib34[i][:,0],obs34,coeffs[loc],
145                            files[libmins[i]],libmins[i],True,False)
146     #print('Coefficient: c= ',coeffs[loc])
147     k34[i]=coeffs[loc]
148     Ls34.append(Ls)
149     r34[i]=r
150     chi34[i] = chi2
151 Ls34=np.array(Ls34)
152 lib34=np.array(lib34)
153 ind34=np.argmin(np.abs(r34))
```

```
154 smallr34=np.array(np.where(np.abs(r34)<1)[0])
155 plotscaledabsfits(x34,obs34,lib34[smallr34],Ls34[smallr34],
156                    r34[smallr34],libmins[smallr34],files,lowerunit,[5,10],1.4)
157 print('Best fit for mineral %.0f: ' %lowerunit,files[libmins[ind34]],
158       'r: %.2f' %r34[ind34])
159
160 #print('Best fit for mineral %.0f: ' %lowerunit,files[libmins[ind34]],
161 #'chi2: %.2f' %chi34[ind34])
162 #smallchi34=np.array(np.where(np.abs(chi34)<.5)[0])
163 #plotscaledabsfits(x34,obs34,lib34[smallchi34],Ls34[smallchi34],
164 #                    chi34[smallchi34],libmins[smallchi34],files,lowerunit,
165 #                    [15,30],1.15)
166
167 plt.plot(df[751]['wavelength'],df[751]['reflectance'])
168 plt.plot([1.3792-.0103,1.3792-.0103],[0,1],'--r',label='FWHM')
169 plt.plot([1.3792+.0103,1.3792+.0103],[0,1],'--r')
170 plt.plot([1.3792,1.3792],[0,1],'--k',label='Center $\lambda$')
171 plt.title('Mica (phlogopite)')
172 plt.xlim(1.35,1.45)
173 plt.legend()
174 plt.ylim(0.4,0.65)
175 plt.show()
176
177
178
179 loadDN=np.loadtxt('D26_mean_spectrum.txt',delimiter='\t')
180 loadD26=np.loadtxt('spectrum_d26.txt',delimiter='\t')
181
182
183
184
185 ############### Upper cliff unit: cliff 1
```

```
x7,obs7,N7,lib7=isolatefeature(loadD26[:,0]/1000,np.arange(0,len(loadD26[:,1]))
    ,[1.3,1.5],loadD26[:,1],libmins,df,files,
                                    min_name,upperunit)
k7=np.zeros(len(libmins))
Ls7=[]
r7=np.zeros(len(libmins))
chi7=np.zeros(len(libmins))
for i in range(0,len(libmins)):
    allr=np.zeros(len(coeffs))
    for j in range(0,len(coeffs)):
        allr[j]=scalefeature(lib7[i][:,1],lib7[i][:,0],obs7,coeffs[j],
                                files[libmins[i]],libmins[i],False,False)
    loc=np.argmin(np.abs(allr))
    chi2,r,Ls=scalefeature(lib7[i][:,1],lib7[i][:,0],obs7,coeffs[loc],
                            files[libmins[i]],libmins[i],True,False)
    #print('Coefficient: c= ',coeffs[loc])
    k7[i]=coeffs[loc]
    Ls7.append(Ls)
    r7[i]=r
    chi7[i]=chi2
Ls7=np.array(Ls7)
lib7=np.array(lib7)
ind7=np.argmin(np.abs(r7))
smallr7=np.array(np.where(np.abs(r7)<.07)[0])
plotscaledabsfits(x7,obs7,lib7[smallr7],Ls7[smallr7],
                    r7[smallr7],libmins[smallr7],files,upperunit,[5,10],1.5)
```

```
# -*- coding: utf-8 -*-
"""
Created on Tue Jul 23 12:47:21 2024

@author: Amanda Steckel
"""
```

```
7  import os
8  import os.path # for checking if files exist
9  import shutil # for moving files
10 from pyunpack import Archive
11 from spectral import open_image
12 import numpy as np
13 import matplotlib.pyplot as plt
14 import matplotlib.colors as mcolors
15 from scipy.interpolate import interp1d
16 from scipy.spatial import ConvexHull
17
18 # Identify which pixel is which mineral
19 def find_pixels(path,loc,group,min_name,data_type,threshold,subfol,num_mins):
20     data=[]
21     fit_data=[]
22     b=[]
23     print('start find_pixels function')
24     for i in range (0,num_mins[0]):
25         # check if file exists in folder
26         # Folder is to be used for cliff data only
27         if os.path.isfile(path+subfol+'\\'+min_name[i]+data_type)==False:
28             print('if statement',i)
29             shutil.copyfile(path+'\\'+loc+group+'\\'+min_name[i]+data_type+
30                             r'.gz.hdr',path+subfol+'\\'+min_name[i]+
31                             data_type+r'.hdr')
32             # unzip the .fd file and save in extrated_data directory
33             Archive(path+'\\'+loc+group+'\\'+min_name[i]+
34                     data_type+r'.gz').extractall(path+subfol)
35         print('here',i)
36         fit_data=open_image(path+subfol+'\\'+min_name[i]+data_type+r'.hdr')
37         tmp=np.shape(fit_data)
38         nrows=tmp[0]
39         ncols=tmp[1]
```

```
40          data.append(np.reshape(fit_data[:,:,:],(nrows,ncols)))
41          tmp_ids=np.where(np.reshape(data[i],nrows*ncols)>threshold)
42          ids=np.unravel_index(tmp_ids,data[i].shape)
43          idr=ids[0]
44          idc=ids[1]
45          b.append(np.zeros((nrows,ncols)))
46          b[i][idr,idc]=1
47          fit_data=[]
48      return data,b
49
50  # Make color plot of mineral IDs. Also creates M matrix for plotting
51  def mycliffplot(min_name,num_mins,b,mytitle):
52      nrows,ncols=np.shape(b[0])
53      color_options=np.linspace(.05,.95,num=num_mins[0])
54      scaledb=np.copy(b)
55      sumM=np.zeros((nrows,ncols))
56      # m should be a 2x2 matrix of the data, can be a list
57      for i in range (0,num_mins[0]):
58          scaledb[i]=scaledb[i]*color_options[i]
59          sumM=sumM+scaledb[i]
60      #c[c==0] = np.nan
61      newM=np.copy(scaledb)
62      m=[]
63      for i in range (0,num_mins[0]):
64          m.append(np.rot90(newM[i],k=1,axes=(0,1)))
65      cmap_choice='gist_ncar'
66      rotatedb=np.copy(m)
67      bwnan=[]
68      plt.rcParams.update({'font.size': 22})
69      fig,ax=plt.subplots(figsize=(12,12))
70      for i in range(0,num_mins[0]):
71          bwnan.append(np.copy(rotatedb[i]))
72          bwnan[i]=np.where(bwnan[i]==0,np.nan,rotatedb[i])
```

```
73              plt.imshow(bwnan[i][:,:],cmap=cmap_choice,vmin=0,vmax=1)
74          cbar=plt.colorbar(ticks=color_options,orientation='horizontal')
75          cbar.ax.set_xticklabels(min_name,rotation=90)
76          plt.suptitle(mytitle)
77          ax.axison = False
78          plt.show()
79
80      def disptetracorder(path,loc,min_group,subfol,data_type,threshold,min_name,
81                              datacube,datacube_name):
82          #Import original datacube and determine number of rows, columns, and bands
83          im_cube=open_image(datacube)
84          matrixcube=np.asarray(im_cube[:,:,:])
85          nrows,ncols,bands=np.shape(matrixcube)
86
87          # Collect group minerals
88          num_mins=np.shape(min_name)
89          data,b=find_pixels(path,loc,min_group,min_name,data_type,threshold,
90                                  subfol,num_mins)
91
92
93          # plot group minerals
94          mycliffplot(min_name,num_mins,b,datacube_name+'Mineral Map: '+min_group)
95          return data,b,matrixcube
96
97      def avgspectra(b,bands,matrixcube):
98          tmp=np.shape(b)
99          nrows=tmp[0]
100         ncols=tmp[1]
101
102         cubeR=np.reshape(matrixcube,(nrows*ncols,bands))
103
104         ##### Get average spectra from 1 mineral
105         is_min1=np.reshape(b,(nrows*ncols))
```

```
106     min1Spec=np.zeros((nrows*ncols,bands))
107
108     for i in range (0,nrows*ncols):
109         if (is_min1[i]):
110             min1Spec[i,:]=cubeR[i,:]
111
112     min1Spec[min1Spec==0]=np.nan
113     mean_min1S=np.nanmean(min1Spec,axis=0) #bright pixel:aSpec[365120,:][good]
114     return mean_min1S
115 ###############################################################################
116 def continuum_removal(points,mineral,show):
117     x, y = points.T
118     augmented = np.concatenate([points, [(x[0], np.min(y)-1),
119                                          (x[-1], np.min(y)-1)]], axis=0)
120     hull = ConvexHull(augmented)
121     cont_pts = points[np.sort([v for v in hull.vertices if v < len(points)])]
122     continuum_function = interp1d(*cont_pts.T)
123     yprime = y / continuum_function(x)
124
125     if show:
126         fig, axes = plt.subplots(2, 1, figsize=(10,10),sharex=True)
127         axes[0].plot(x, y, label='Data')
128         axes[0].plot(*cont_pts.T, label='Continuum')
129         axes[0].legend()
130         axes[0].set_title('Identify Continuum from Spectrum')
131         axes[1].plot(x, yprime, '-k',label='Data / Continuum')
132         axes[1].legend()
133         fig.supylabel('Reflectance')
134         axes[1].set_xlabel('Wavelength ($\mu$m)')
135         axes[1].set_title('Normalized Spectrum')
136         #plt.suptitle(mineral)
137     return np.c_[x, yprime]
138
```

```
139 ########## Functions ############################################################
140 def isolatefeature(lam,good,feature,meanS,libmins,df,files,min_name,index):
141     print("For mineral: ",min_name[index], "Number: ", index)
142     # only pass the good wavelengths for lam and meanS vectors
143     left=min(np.where(lam[good]>feature[0])[0])
144     right=max(np.where(lam[good]<feature[1])[0])
145     print("Left absorption feature: ",
146           lam[min(np.where(lam[good]>feature[0])[0])],"microns")
147     print("Right absorption feature: ",
148           lam[max(np.where(lam[good]<feature[1])[0])],"microns")
149 
150     points = np.column_stack((lam[good][left:right],meanS[good][left:right]))
151     # change nan to 0 for continua removal function
152     points[np.where(np.isnan(points))]=0
153     # isolate feature by removing continua from observed data
154     new_points=continuum_removal(points,'PikaIR',False)
155     obs=new_points[:,1]
156     N=np.shape(lam[good][left:right])[0]
157     lib=[]
158     for i in range(0,len(libmins)):
159         libspec=np.interp(lam,df[libmins[i]]['wavelength'],
160                           df[libmins[i]]['reflectance'])
161         libpoints=np.column_stack((lam[good][left:right],
162                                    libspec[good][left:right]))
163         libfeature=continuum_removal(libpoints,files[libmins[i]],False)
164         lib.append(np.copy(libfeature))
165     return lam[good][left:right],obs,N,lib
166 
167 ###############################################################################
168 def scalefeature(s,x,obs,c,mineral,index,toggle,plottoggle):
169     Ls=(s+c)/(1+c)
170     r=np.sum((Ls-obs)**2)
171 
```

```
172     if plottoggle:
173         plt.figure(figsize=(15,10))
174         plt.plot(x,obs,marker='o', linestyle='-',color='k',
175                 label='Tetracorder Feature in PikaIR Data')
176         plt.plot(x,s,marker='o',color='r',linestyle='-',label=mineral)
177         plt.plot(x,Ls,marker='o',color='orange',linestyle='-',
178                 label='Scaled k=%.2f, r=%.2f' %(c,r))
179         plt.title('Scaled Absorption Feature Mineral %.0f' %index)
180         plt.xlabel('Wavelength in $\mu$m')
181         plt.legend()
182         plt.show()
183         print('r: ',r)
184     obs=obs+1 # needed when data is very close to 0 to avoid a divide by 0
185     Lsnew=Ls+1
186     chi2=np.sum((obs-Lsnew)**2/Lsnew)
187     if toggle:
188         #print('chi^2: ',chi2)
189         return chi2,r,Ls
190     else:
191         return r
192
193 ##############################################################################
194 def plotscaledabsfits(x,obs,lib,Ls,chi,libmins,files,index,figshape,vertdist):
195     mycolors=list(mcolors.TABLEAU_COLORS.keys()) #_colors_full_map.values()
196     mylabels=np.ones(len(libmins))
197     mylabels[0]=0
198     plt.figure(figsize=figshape) #
199     plt.plot(x,obs,marker='o', linestyle='-',color='k',
200             label='Tetracorder Absorption Feature')
201     for i in range(0,len(libmins)):
202         plt.plot(lib[i][:,0],Ls[i]+i,marker='o',color=mycolors[i],
203                 linestyle='-',label=files[libmins[i]]+r' r=%.2f' %chi[i])
204         plt.plot(x,obs+i,marker='o', linestyle='-',color='k')
```

```
205             print(files[libmins[i]],chi[i])
206         plt.title('Best Mineral Fits: group %.0f' %index)
207         plt.ylabel('Reflectance: Minerals Offset for Clarity')
208         plt.xlabel('Wavelength in $\mu$m')
209         plt.yticks(ticks=np.arange(len(libmins)),labels=mylabels)
210         plt.legend(loc='upper center',bbox_to_anchor=[.5,vertdist],ncol=1) #ncol=2
211         plt.show()
212 ##############################################################################
```

C.2 Calculate Absorption versus Distance in Water Band

```
1  # -*- coding: utf-8 -*-
2  """
3  Created on Tue Jul 16 11:42:23 2024
4
5  @author: avste
6  """
7  import numpy as np
8  import pandas as pd
9  import matplotlib.pyplot as plt
10
11 path=r'C:\Users\avste\local_doc\TREXcode'
12 datafile=r'Theory data.txt'
13 data = pd.read_csv(path+'\\'+datafile,sep='\t',dtype=float)
14 Cs=data['Cross Section']*100*100 # m2/molecule ATM
15 wav=10000/(data['Wave Number']) #micron
16 kb=1.380649*10**(-23) #J/K = kg m2 s-2 K-1
17 T=300
18
19 RH=.3 # relative humidity
20 vp=.042 #ATM atmospheric pressure at 300K
21
22 Ph2o=RH*vp
```

```
23
24 alpha=(Cs/(kb*T))*(Ph2o**2)
25
26 d1=1 #meters
27 d2=50 #meters
28 d3=3000 #meters
29 tr1=np.exp(-alpha*d1)
30 tr2=np.exp(-alpha*d2)
31 tr3=np.exp(-alpha*d3)
32
33 plt.figure(figsize=(10,6))
34 plt.plot(wav,tr1,color='orange',marker='.',linestyle='-',label='Zo$\ddot{e}$, 1m')
35 plt.plot(wav,tr2,color='cyan',marker='.',linestyle='-',label='PikaIR 50m')
36 plt.plot(wav,tr3,color='black',marker='.',linestyle='-',label='AVIRIS 3000m')
37 plt.ylim(0,1)
38 plt.xlim(1.25,1.5)
39 plt.xlabel('Wavelength $\mu$ m')
40 plt.ylabel ('Transmission %')
41 plt.title('Signal Transmission at Different Distances')
42 plt.legend(loc='upper right',bbox_to_anchor=(1.45, 0.7))
43 plt.show()
44
45 plt.figure(figsize=(10,6))
46 plt.plot(wav,tr1,color='orange',marker='.',linestyle='-',label='Zo$\ddot{e}$, 1m')
47 plt.plot(wav,tr2,color='cyan',marker='.',linestyle='-',label='PikaIR 50m')
48 plt.plot(wav,tr3,color='black',marker='.',linestyle='-',label='AVIRIS 3000m')
49 plt.ylim(0,1)
50 #plt.xlim(1.25,1.5)
51 plt.xlabel('Wavelength $\mu$ m')
52 plt.ylabel ('Transmission %')
53 plt.title('Signal Transmission at Different Distances')
54 plt.legend(loc='upper right',bbox_to_anchor=(1.45, 0.7))
55 plt.show()
```

```
56
57 print(wav[np.where(tr2<.01)[0]])
58 tmp=np.where(tr2>.01)
59 plt.figure(figsize=(10,6))
60 plt.plot(wav,tr1,color='orange',marker='.',linestyle='-',label= '1m') #'Zo$\ddot{e}$
     ,
61 plt.plot(wav,tr2,color='cyan',marker='.',linestyle='-',label='50m') #PikaIR
62 plt.plot(wav[tmp[0]],tr2[tmp[0]],'ob')
63 plt.plot(wav,tr3,color='black',marker='.',linestyle='-',label='3000m') #AVIRIS
64 plt.yscale('log')
65 plt.ylim(10**(-22),1)
66 plt.xlim(1.2,1.6)
67 plt.xlabel('Wavelength $\mu$ m')
68 plt.ylabel ('Transmission %')
69 plt.title('Signal Transmission at Different Distances')
70 plt.legend(loc='upper right',bbox_to_anchor=(1.45, 0.7))
71 plt.show()
```

C.3 1.3, 1.4, 1.5 micron Group Minerals

```
1 # -*- coding: utf-8 -*-
2 """
3 Created on Thu May  2 10:59:24 2024
4
5 @author: avste
6 """
7 import matplotlib
8 import numpy as np
9 import matplotlib.pyplot as plt
10
11 # create plot of feature widths vs. center wavelength
12 #### TODO: Change widths to FWHM
13
```

```
14
15 # Create lists of mineral names that match results file from tetracorder
16 # Group 2 minerals
17 min_name2=[r'sulfate_na82alun100c',r'sulfate_na63alun300c',r'polyhalite',
18            r'zeolite_natrolite',r'hydroxide_gibbsite',r'sulfate_naalun150c',
19            r'sulfate_alun35K65Na.low',r'sulfate_ammonjarosite',r'elbaite',
20            r'borate_pinnoite',r'ulexite',r'rivadavite',
21            r'sulfate_mix_gypsum.trace.dust+debris_WTC01_2',
22            r'sulfate_ammonalunite',r'sulfate_alun66K34Na.low',
23            r'sulfate_naalun300c',r'prehnite',r'zeolite_analcime',
24            r'sulfate_na40alun400c',r'sulfate_kalun150c',r'sulfate_naalun450c',
25            r'sulfate_alun73K27Na.low']
26 #min_name=min_name[::-1] # reverse the order of minerals
27
28 # Group 1.5 minerals
29 min_name15=[r'ohc_1.451_hydroxide_gibbsite',r'ohc_1.455_zeolite_natrolite',
30              r'ohc_1.464_sulfate_bloedite',r'ohc_1.469_sulfate_jarosite_k',
31              r'ohc_1.471_nesisil_datolite',r'ohc_1.471_sulfate_jarosite_k',
32              r'ohc_1.478_sulfate_jarosite_na90c',
33              r'ohc_1.479_sulfate_jarosite_na200c',
34              r'ohc_1.480_phyllo_prehnite',r'vegetation.dry+green',
35              r'vegetation1',r'water.red.algae',r'water+mont0.5gpl',
36              r'water+mont1.67gpl',r'water+mont5.01gpl',r'water+mont16.5gpl']
37
38 min_name14=[r'ohb_1.385_phyllo_nacrite',
39              r'ohb_1.400_phyllo_cookeite',r'ohb_1.406_nesosil_topaz',
40              r'ohb_1.406_tectosil_opal',r'ohb_1.408_mica_paragonite',
41              r'ohb_1.409_phyllo_lepidolite',r'ohb_1.409_smectite_sauconite',
42              r'ohb_1.410_kaolgrp_halloysite',r'ohb_1.410_mica_margarite',
43              r'ohb_1.410_mica_muscovite',r'ohb_1.410_phyllo_chrysocolla',
44              r'ohb_1.411_smectite_montmor_swy',
45              r'ohb_1.413_kaolgrp_kaolinite_pxl',
46              r'ohb_1.413_nesosil_hydrogross',r'ohb_1.414_smectite_hectorite',
```

```
47                  r'ohb_1.416_mica-roscoelite',
48                  r'ohb_1.416_smectite-montmor-saz',r'ohb_1.417_phyllo-palygorsk',
49                  r'ohb_1.418_mica_muscovite',r'ohb_1.418_zeolite_mordonite',
50                  r'ohb_1.419_zeolite-clinpt',r'ohb_1.419_zeolite-stilbite',
51                  r'ohb_1.422_zeolite-heuland',r'ohb_1.423_scapolute-meionite',
52                  r'ohb_1.424_smectite-nontronite',r'ohb_1.424_zeolite-analcime',
53                  r'ohb_1.425_scapolite-mizzonite',r'ohb_1.425_sulfate-alunite',
54                  r'ohb_1.429_sodalite-lazurite',r'ohb_1.431_cyclosil-elbaite',
55                  r'ohb_1.431_zeolite-laumontite',r'ohb_1.432_phyllo-vermiculite',
56                  r'ohb_1.435_tourmaline',r'ohb_1.436_sulfate-eugsterite',
57                  r'ohb_1.438_sulfate-alunite-na',r'ohb_1.440_zeolite-scolecite',
58                  r'ohb_1.447_sulfate-gypsum',r'ohb_1.449_sulfate-schwertm',
59                  r'ohb_1.450_sulfate-copiapite',r'ohb_1.451_hydroxide-gibbsite',
60                  r'ohb_1.455_zeolite-natrolite',
61                  r'ohb_1.4106_kaolin.5+muscov.medhighAl',
62                  r'vegetation.dry+green',r'vegetation1',r'water.red.algae',
63                  r'water+mont0.5gpl',r'water+mont1.67gpl',r'water+mont5.01gpl',
64                  r'water+mont16.5gpl']
65
66  min_name13=[r'oh_1.378_phyllo-ksg-chrysotile',r'oh_1.381_phyllo-ksg-dickite',
67                  r'oh_1.383_amphibole-richterite',r'oh_1.385_phyllo-ksg-nacrite',
68                  r'oh_1.388_phyllo-chlorite',r'oh_1.390_phyllo-ksg-endellite',
69                  r'oh_1.392_amphibole-tremolite',r'oh_1.392_phyllo-ksg-lizardite',
70                  r'oh_1.392_smectite-saponite',r'oh_1.393_phyllo-serpentine',
71                  r'oh_1.393_phyllo-talc',r'oh_1.394_phyllo-pyrophyllite',
72                  r'oh_1.395_phyllo-ksg-antigorite',r'oh_1.396_amphibole-actinolite',
73                  r'oh_1.396_amphibole-uralite',r'oh_1.397_mica-phlogopite',
74                  r'oh_1.398_amphibole-smaragdit',r'oh_1.398_phyllo-clinochlore',
75                  r'oh_1.398-phyllo-kaolinite-wxl',
76                  r'oh_1.400_phyllo-chlorgrp-cookeite',
77                  r'oh_1.401_mica-lepidolite',r'oh_1.406_silica-opal',
78                  r'oh_1.408_mica-paragonite',r'oh_1.409_mica-lepidolite',
79                  r'oh_1.413_phyllo-kaolinite-pxl',r'oh_1.432_phyllo-vermiculite',
```

```
80              r'oh_1.4106_kaolin.5+muscov.medhighAl',r'vegetation.dry+green',
81              r'vegetation1',r'water.red.algae',r'water+mont0.5gpl',
82              r'water+mont1.67gpl',r'water+mont5.01gpl',r'water+mont16.5gpl']
83
84  tet_file=r'cmd.lib.setup.t5.27.c1'
85
86  f15_name=[r'Gibbsite','Zeolite',r'Sulfate',r'Sulfate','Nesosilicate',
87            r'Sulfate','Phyllosilicate']
88  f15_index=[1812,3474,798,2568,1470,2556,2514,2526,4026,7614,7170,6318,6336,
89             6342]
90  f15=np.zeros((16,8))
91  f15[0]=[1.27,1.31,1.335,1.370,1.490,1.520,1.56,1.59]
92  f15[1]=[1.29,1.32,1.350,1.385,1.520,1.555,1.58,1.62]
93  f15[2]=[1.29,1.33,1.365,1.4,1.56,1.595,1.64,1.68]
94  f15[3]=[1.345,1.380,1.400,1.436,1.490,1.520,1.57,1.60]
95  f15[4]=[1.31,1.34,1.365,1.400,1.520,1.555,1.58,1.62]
96  f15[5]=[1.325,1.360,1.390,1.415,1.550,1.585,1.60,1.64]
97  f15[6]=[1.29,1.32,1.350,1.385,1.520,1.555,1.58,1.62]
98  f15[7]=[1.340,1.380,1.408,1.442,1.505,1.54,1.60,1.64]
99  f15[8]=[1.32,1.36,1.385,1.42,1.52,1.555,1.595,1.635]
100 f15[9]=[0.87,0.9,1.063,1.093,1.063,1.093,1.265,1.305]
101 f15[10]=[0.87,0.9,1.063,1.093,1.063,1.093,1.265,1.305]
102 f15[11]=[0.883,0.913,1.055,1.085,1.064,1.094,1.269,1.299]
103 f15[12]=[0.881,0.911,1.052,1.082,1.064,1.094,1.269,1.299]
104 f15[13]=[0.881,0.911,1.055,1.085,1.064,1.094,1.269,1.299]
105
106 f15_f1_widths=[]
107 f15_f1_pos=[]
108 f15_f2_widths=[]
109 f15_f2_pos=[]
110 for i in range(0,np.shape(f15_index)[0]):
111     left_f1=(f15[i,0]+f15[i,1])/2
112     right_f1=(f15[i,2]+f15[i,3])/2
```

```
113         f1_width=right_f1-left_f1
114         f1_wav=(left_f1+right_f1)/2
115
116         f15_f1_widths.append(f1_width)
117         f15_f1_pos.append(f1_wav)
118
119         left_f2=(f15[i,4]+f15[i,5])/2
120         right_f2=(f15[i,6]+f15[i,7])/2
121         f2_width=right_f2-left_f2
122         f2_wav=(left_f2+right_f2)/2
123
124         f15_f2_widths.append(f2_width)
125         f15_f2_pos.append(f2_wav)
126
127 f14_index=[3462,2706,1344,4926,3816,3876,2832,4464,2040,2976,3348,1134,588,672,
128             2310,696,4380,690,3228,3864,3336,3282,1278,4752,2214,3024,3570,414,
129             3162,306,2796,1626,2784,5226,5136,1710,228,4482,1998,4476,1374,1812,
130             3474,5838]
131
132 f14=np.zeros((51,8))
133 f14[0]=[1.26,1.29,1.305,1.345,1.440,1.475,1.49,1.53]
134 f14[1]=[1.25,1.29,1.305,1.340,1.450,1.490,1.51,1.55]
135 f14[2]=[1.28,1.31,1.332,1.365,1.495,1.530,1.54,1.58]
136 f14[3]=[1.27,1.31,1.330,1.365,1.440,1.470,1.49,1.53]
137 f14[4]=[1.26,1.30,1.322,1.360,1.505,1.545,1.56,1.60]
138 f14[5]=[1.30,1.33,1.342,1.375,1.440,1.480,1.50,1.54]
139 f14[6]=[1.27,1.31,1.322,1.360,1.450,1.490,1.50,1.54]
140 f14[7]=[1.30,1.33,1.342,1.370,1.50,1.54,1.56,1.60]
141 f14[8]=[1.26,1.30,1.315,1.350,1.450,1.485,1.51,1.55]
142 f14[9]=[1.30,1.33,1.342,1.377,1.435,1.470,1.49,1.53]
143 f14[10]=[1.342,1.370,1.445,1.475,1.445,1.475,1.48,1.51]
144 f14[11]=[1.30,1.33,1.342,1.370,1.50,1.54,1.56,1.60] # kaolinite
145 f14[12]=[1.30,1.33,1.342,1.370,1.480,1.515,1.53,1.57] # montmor
```

```
146 f14[13]=[1.25,1.29,1.305,1.340,1.45,1.49,1.51,1.55] # kaolinite
147 f14[14]=[1.27,1.31,1.330,1.365,1.490,1.525,1.54,1.58]
148 f14[15]=[1.27,1.31,1.332,1.365,1.510,1.545,1.56,1.60]
149 f14[16]=[1.30,1.33,1.345,1.378,1.458,1.494,1.52,1.56]
150 f14[17]=[1.27,1.31,1.332,1.365,1.520,1.555,1.57,1.61]
151 f14[18]=[1.30,1.33,1.342,1.370,1.520,1.555,1.57,1.61] #mont
152 f14[19]=[1.28,1.32,1.337,1.365,1.510,1.545,1.56,1.60]
153 f14[20]=[1.30,1.33,1.344,1.380,1.455,1.490,1.52,1.56] #mica muscovite
154 f14[21]=[1.26,1.30,1.322,1.360,1.510,1.545,1.56,1.60]
155 f14[22]=[1.25,1.29,1.312,1.35,1.51,1.545,1.57,1.61]
156 f14[23]=[1.25,1.29,1.312,1.35,1.51,1.545,1.57,1.61]
157 f14[24]=[1.25,1.29,1.312,1.35,1.51,1.545,1.57,1.61]
158 f14[25]=[1.30,1.33,1.342,1.378,1.485,1.52,1.55,1.59]
159 f14[26]=[1.30,1.33,1.342,1.370,1.510,1.545,1.57,1.61]
160 f14[27]=[1.342,1.370,1.445,1.475,1.497,1.537,1.55,1.58]
161 f14[28]=[1.30,1.33,1.342,1.378,1.485,1.520,1.55,1.59]
162 f14[29]=[1.342,1.370,1.424,1.456,1.444,1.465,1.46,1.49]  # sulfate
163 f14[30]=[1.30,1.33,1.342,1.370,1.520,1.555,1.57,1.61] #sodalite
164 f14[31]=[1.30,1.33,1.342,1.378,1.515,1.550,1.57,1.61]
165 f14[32]=[1.25,1.29,1.312,1.35,1.53,1.565,1.59,1.63]
166 f14[33]=[1.30,1.33,1.342,1.37,1.54,1.58,1.6,1.65]
167 f14[34]=[1.342,1.37,1.465,1.495,1.465,1.495,1.50,1.53] #tourmaline,
168 f14[35]=[1.30,1.33,1.342,1.376,1.53,1.565,1.59,1.63]
169 f14[36]=[1.342,1.37,1.424,1.456,1.530,1.560,1.57,1.60] #sulfate,
170 f14[37]=[1.30,1.33,1.342,1.370,1.518,1.553,1.57,1.61]
171 f14[38]=[1.30,1.33,1.342,1.378,1.570,1.605,1.63,1.67] #gypsum
172 f14[39]=[1.30,1.33,1.350,1.385,1.590,1.625,1.64,1.68]
173 f14[40]=[1.30,1.33,1.342,1.377,1.580,1.625,1.64,1.68]
174 f14[41]=[1.27,1.31,1.335,1.370,1.490,1.520,1.56,1.59]
175 f14[42]=[1.29,1.32,1.350,1.385,1.520,1.555,1.58,1.62]
176 f14[43]=[1.315,1.342,1.450,1.475,1.315,1.342,1.450,1.475] #1 feature
177
178 f14_f1_widths=[]
```

```
179 f14_f1_pos=[]
180 f14_f2_widths=[]
181 f14_f2_pos=[]
182 for i in range(0,np.shape(f14_index)[0]):
183     left_f1=(f14[i,0]+f14[i,1])/2
184     right_f1=(f14[i,2]+f14[i,3])/2
185     f1_width=right_f1-left_f1
186     f1_wav=(left_f1+right_f1)/2
187 
188     f14_f1_widths.append(f1_width)
189     f14_f1_pos.append(f1_wav)
190 
191     left_f2=(f14[i,4]+f14[i,5])/2
192     right_f2=(f14[i,6]+f14[i,7])/2
193     f2_width=right_f2-left_f2
194     f2_wav=(left_f2+right_f2)/2
195 
196     f14_f2_widths.append(f2_width)
197     f14_f2_pos.append(f2_wav)
198 
199 
200 f13_index=[1146,1518,4338,3462,1086,1632,5142,2904,702,4548,4800,4182,630,36,
201             5202,3918,4596,660,594,780,2820,3816,3876,2832,672,5226,5838]
202 f13=np.zeros((34,8))
203 f13[0]=[1.27,1.3,1.31,1.35,1.424,1.456,1.46,1.49] #phyllo
204 f13[1]=[1.26,1.29,1.305,1.345,1.44,1.475,1.49,1.53] #phyllo
205 f13[2]=[1.28,1.31,1.332,1.362,1.41,1.45,1.46,1.49] #amphabol
206 f13[3]=[1.26,1.29,1.305,1.345,1.44,1.475,1.49,1.53] #phyllo
207 f13[4]=[1.30,1.33,1.342,1.37,1.424,1.456,1.46,1.49] #phyllo
208 f13[5]=[1.26,1.29,1.305,1.345,1.45,1.485,1.5,1.54] #phyllo
209 f13[6]=[1.29,1.32,1.332,1.365,1.41,1.44,1.46,1.49] #amphabol
210 f13[7]=[1.26,1.30,1.315,1.350,1.440,1.475,1.49,1.53] #phyllo
211 f13[8]=[1.26,1.30,1.315,1.350,1.490,1.525,1.54,1.58] #phyllo
```

```
212 f13[9]=[1.27,1.31,1.327,1.360,1.440,1.475,1.49,1.53] #phyllo
213 f13[10]=[1.30,1.33,1.342,1.375,1.430,1.466,1.48,1.51] #phyllo
214 f13[11]=[1.342,1.370,1.424,1.456,1.30,1.33,1.342,1.370] #phyllo
215 f13[12]=[1.30,1.33,1.342,1.375,1.430,1.460,1.47,1.50] #phyllo
216 f13[13]=[1.342,1.370,1.424,1.456,1.30,1.33,1.342,1.370] #amphabol
217 f13[14]=[1.30,1.33,1.342,1.378,1.424,1.456,1.46,1.49] #amphabol
218 f13[15]=[1.28,1.31,1.332,1.362,1.420,1.450,1.46,1.49] #mica
219 f13[16]=[1.30,1.33,1.342,1.370,1.430,1.465,1.48,1.51] #amph
220 f13[17]=[1.29,1.32,1.332,1.375,1.424,1.456,1.47,1.50] #phyllo
221 f13[18]=[1.25,1.29,1.305,1.340,1.450,1.490,1.51,1.55] #phyllo
222 f13[19]=[1.28,1.31,1.332,1.365,1.495,1.530,1.54,1.58]  #phyllo
223 f13[20]=[1.27,1.31,1.322,1.360,1.438,1.475,1.49,1.53]  #mica
224 f13[21]=[1.26,1.30,1.322,1.360,1.505,1.545,1.56,1.60]  #opal
225 f13[22]=[1.30,1.33,1.342,1.375,1.440,1.480,1.50,1.54] #mica
226 f13[23]=[1.27,1.31,1.322,1.360,1.450,1.490,1.50,1.54] #mica
227 f13[24]=[1.25,1.29,1.305,1.340,1.450,1.490,1.51,1.55] #phyllo
228 f13[25]=[1.30,1.33,1.342,1.370,1.540,1.580,1.60,1.65] #phyllo
229 f13[26]=[1.315,1.342,1.450,1.475,1.315,1.342,1.450,1.475] #kaol
230
231 f13_f1_widths=[]
232 f13_f1_pos=[]
233 f13_f2_widths=[]
234 f13_f2_pos=[]
235 for i in range(0,np.shape(f13_index)[0]):
236     left_f1=(f13[i,0]+f13[i,1])/2
237     right_f1=(f13[i,2]+f13[i,3])/2
238     f1_width=right_f1-left_f1
239     f1_wav=(left_f1+right_f1)/2
240
241     f13_f1_widths.append(f1_width)
242     f13_f1_pos.append(f1_wav)
243
244     left_f2=(f13[i,4]+f13[i,5])/2
```

```
245         right_f2=(f13[i,6]+f13[i,7])/2
246         f2_width=right_f2-left_f2
247         f2_wav=(left_f2+right_f2)/2
248
249         f13_f2_widths.append(f2_width)
250         f13_f2_pos.append(f2_wav)
251
252
253 #import matplotlib.colors as mcolors
254 cmap=matplotlib.colormaps['jet']
255 colors=cmap(np.linspace(0,1,np.shape(f14_index)[0]))
256
257
258 sulfate_pos=[f15_f1_pos[2],f15_f1_pos[3],f15_f1_pos[5],f15_f1_pos[6],
259                 f15_f1_pos[7],f15_f2_pos[2],f15_f2_pos[3],f15_f2_pos[5],
260                 f15_f2_pos[6],f15_f2_pos[7],f14_f1_pos[29],f14_f2_pos[29],
261                 f14_f1_pos[35],f14_f2_pos[35],f14_f1_pos[36],f14_f2_pos[36],
262                 f14_f1_pos[39],f14_f2_pos[39],f14_f1_pos[40],f14_f2_pos[40]] #,
263
264 sulfate_widths=[f15_f1_widths[2],f15_f1_widths[3],f15_f1_widths[5],
265                    f15_f1_widths[6],f15_f1_widths[7],f15_f2_widths[2],
266                    f15_f2_widths[3],f15_f2_widths[5],f15_f2_widths[6],
267                    f15_f2_widths[7],f14_f1_widths[29],f14_f2_widths[29],
268                    f14_f1_widths[35],f14_f2_widths[35],f14_f1_widths[36],
269                    f14_f2_widths[36],f14_f1_widths[39],f14_f2_widths[39],
270                    f14_f1_widths[40],f14_f2_widths[40]]
271
272 phyllo_pos=[f15_f1_pos[8],f15_f2_pos[8],f14_f1_pos[0],f14_f2_pos[0],
273                f14_f1_pos[2],f14_f2_pos[2],f14_f1_pos[6],f14_f2_pos[6],
274                f14_f1_pos[7],f14_f2_pos[7],f14_f1_pos[11],f14_f2_pos[11],
275                f14_f1_pos[15],f14_f2_pos[15],f14_f1_pos[17],f14_f2_pos[17],
276                f14_f1_pos[19],f14_f2_pos[19],f14_f1_pos[26],f14_f2_pos[26],
277                f14_f1_pos[33],f14_f2_pos[33],f13_f1_pos[0],f13_f2_pos[0],
```

```
278                 f13_f1_pos[1],f13_f2_pos[1],f13_f1_pos[3],f13_f2_pos[3],
279                 f13_f1_pos[4],f13_f2_pos[4],f13_f1_pos[5],f13_f2_pos[5],
280                 f13_f1_pos[7],f13_f2_pos[7],f13_f1_pos[8],f13_f2_pos[8],
281                 f13_f1_pos[9],f13_f2_pos[9],f13_f1_pos[10],f13_f2_pos[10],
282                 f13_f1_pos[11],f13_f2_pos[11],f13_f1_pos[12],f13_f2_pos[12],
283                 f13_f1_pos[17],f13_f2_pos[17],f13_f1_pos[18],f13_f2_pos[18],
284                 f13_f1_pos[24],f13_f2_pos[24],f13_f1_pos[25],f13_f2_pos[25]]
285
286 phyllo_widths=[f15_f1_widths[8],f15_f2_widths[8],f14_f1_widths[0],
287                     f14_f2_widths[0],
288                     f14_f1_widths[2],f14_f2_widths[2],f14_f1_widths[6],
289                     f14_f2_widths[6],
290                     f14_f1_widths[7],f14_f2_widths[7],f14_f1_widths[11],
291                     f14_f2_widths[11],
292                     f14_f1_widths[15],f14_f2_widths[15],f14_f1_widths[17],
293                     f14_f2_widths[17],
294                     f14_f1_widths[19],f14_f2_widths[19],f14_f1_widths[26],
295                     f14_f2_widths[26],
296                     f14_f1_widths[33],f14_f2_widths[33],f13_f1_widths[0],
297                     f13_f2_widths[0],
298                     f13_f1_widths[1],f13_f2_widths[1],f13_f1_widths[3],
299                     f13_f2_widths[3],
300                     f13_f1_widths[4],f13_f2_widths[4],f13_f1_widths[5],
301                     f13_f2_widths[5],
302                     f13_f1_widths[7],f13_f2_widths[7],f13_f1_widths[8],
303                     f13_f2_widths[8],
304                     f13_f1_widths[9],f13_f2_widths[9],f13_f1_widths[10],
305                     f13_f2_widths[10],
306                     f13_f1_widths[11],f13_f2_widths[11],f13_f1_widths[12],
307                     f13_f2_widths[12],
308                     f13_f1_widths[17],f13_f2_widths[17],f13_f1_widths[18],
309                     f13_f2_widths[18],
310                     f13_f1_widths[24],f13_f2_widths[24],f13_f1_widths[25],
```

```
311                 f13_f2_widths[25]]
312
313 mica_pos=[f14_f1_pos[5],f14_f2_pos[5],f14_f1_pos[9],f14_f2_pos[9],
314           f14_f1_pos[16],f14_f2_pos[16],f14_f1_pos[20],f14_f2_pos[20],
315           f13_f1_pos[15],f13_f2_pos[15],f13_f1_pos[22],f13_f2_pos[22],
316           f13_f1_pos[23],f13_f2_pos[23]]
317
318 mica_widths=[f14_f1_widths[5],f14_f2_widths[5],f14_f1_widths[9],
319              f14_f2_widths[9],
320              f14_f1_widths[16],f14_f2_widths[16],f14_f1_widths[20],
321              f14_f2_widths[20],
322              f13_f1_widths[15],f13_f2_widths[15],f13_f1_widths[22],
323              f13_f2_widths[22],
324              f13_f1_widths[23],f13_f2_widths[23]]
325
326 zeolite_pos=[f15_f1_pos[1],f15_f2_pos[1],f14_f1_pos[21],f14_f2_pos[21],
327              f14_f1_pos[22],f14_f2_pos[22],f14_f1_pos[23],f14_f2_pos[23],
328              f14_f1_pos[24],f14_f2_pos[24],f14_f1_pos[27],f14_f2_pos[27],
329              f14_f1_pos[32],f14_f2_pos[32],f14_f1_pos[37],f14_f2_pos[37],
330              f14_f1_pos[42],f14_f2_pos[42]]
331
332 zeolite_widths=[f15_f1_widths[1],f15_f2_widths[1],f14_f1_widths[21],
333                 f14_f2_widths[21],
334                 f14_f1_widths[22],f14_f2_widths[22],f14_f1_widths[23],
335                 f14_f2_widths[23],
336                 f14_f1_widths[24],f14_f2_widths[24],f14_f1_widths[27],
337                 f14_f2_widths[27],
338                 f14_f1_widths[32],f14_f2_widths[32],f14_f1_widths[37],
339                 f14_f2_widths[37],
340                 f14_f1_widths[42],f14_f2_widths[42]]
341
342 amph_pos=[f13_f1_pos[2],f13_f2_pos[2],f13_f1_pos[6],f13_f2_pos[6],
343           f13_f1_pos[13],f13_f2_pos[13],f13_f1_pos[14],f13_f2_pos[14],
```

```
344             f13_f1_pos[16],f13_f2_pos[16]]
345
346 amph_widths=[f13_f1_widths[2],f13_f2_widths[2],f13_f1_widths[6],
347                 f13_f2_widths[6],
348                 f13_f1_widths[13],f13_f2_widths[13],f13_f1_widths[14],
349                 f13_f2_widths[14],
350                 f13_f1_widths[16],f13_f2_widths[16]]
351
352
353 plt.figure()
354 ax = plt.subplot(111)
355 plt.plot(sulfate_pos,sulfate_widths,'o',color='r',label='Sulfate')
356 plt.plot([f15_f1_pos[4],f15_f2_pos[4],f14_f1_pos[3],f14_f2_pos[3],
357             f14_f1_pos[14],f14_f2_pos[14]],
358            [f15_f1_widths[4],f15_f2_widths[4],f14_f1_widths[3],f14_f2_widths[3],
359             f14_f1_widths[14],f14_f2_widths[14]],
360            'o',color='mediumblue',label='Neosilicate')
361 plt.plot(phyllo_pos,phyllo_widths,'o',color='k',label='Phyllosilicate')
362 plt.plot([f15_f1_pos[0],f15_f2_pos[0],f14_f1_pos[41],f14_f2_pos[41]],
363            [f15_f1_widths[0],f15_f2_widths[0],f14_f1_widths[41],
364             f14_f2_widths[41]],
365            'o',color='m',label='Gibbsite')
366 plt.plot(zeolite_pos,zeolite_widths,'o',color='y',label='Zeolite')
367 plt.plot([f15_f1_pos[9],f15_f1_pos[10],f15_f2_pos[9],f15_f2_pos[10]],
368            [f15_f1_widths[9],f15_f1_widths[10],f15_f2_widths[9],
369             f15_f2_widths[10]],
370            'o',color='yellowgreen',label='Vegetation')
371 plt.plot([f15_f1_pos[11],f15_f1_pos[12],f15_f1_pos[13],f15_f2_pos[11],
372             f15_f2_pos[12],f15_f2_pos[13]],
373            [f15_f1_widths[11],f15_f1_widths[12],f15_f1_widths[13],
374             f15_f2_widths[11],f15_f2_widths[12],f15_f2_widths[13]],
375            'o',color='lightblue',label='Water')
376 plt.plot([f14_f1_pos[4],f14_f2_pos[4],f13_f1_pos[21],f13_f2_pos[21]],
```

```
377             [f14_f1_widths[4],f14_f2_widths[4],f13_f1_pos[21],f13_f2_pos[21]],
378             'o',color='orange',label='Opal')
379 plt.plot(amph_pos,amph_widths,'o',color='yellow',label='Amphibole')
380 plt.plot([f14_f1_pos[25],f14_f2_pos[25],f14_f1_pos[28],f14_f2_pos[28]],
381             [f14_f1_widths[25],f14_f2_widths[25],f14_f1_widths[28],
382              f14_f2_widths[28]],
383             'o',color='c',label='Scapolute')
384 plt.plot([f14_f1_pos[30],f14_f2_pos[30]],[f14_f1_widths[30],f14_f2_widths[30]],
385             'o',color='purple',label='Sodalite')
386 plt.plot([f14_f1_pos[31],f14_f2_pos[31]],[f14_f1_widths[31],f14_f2_widths[31]],
387             'o',color='grey',label='Elbaite')
388 plt.plot([f14_f1_pos[34],f14_f2_pos[34]],[f14_f1_widths[34],f14_f2_widths[34]],
389             'o',color='k',label='Tourmaline')
390 plt.plot(mica_pos,mica_widths,'o',color='darkgreen',label='Mica')
391 plt.plot([f14_f1_pos[1],f14_f2_pos[1],f14_f1_pos[13],f14_f2_pos[13],
392              f14_f1_pos[43],f14_f2_pos[43],f13_f1_pos[26],f13_f2_pos[26]],
393             [f14_f1_widths[1],f14_f2_widths[1],f14_f1_widths[13],
394              f14_f2_widths[13],f14_f1_widths[43],f14_f2_widths[43],
395              f13_f1_widths[26],f13_f2_widths[26]],
396             'D',color='deeppink',label='Kaolinite')
397 plt.plot([f14_f1_pos[8],f14_f2_pos[8]],[f14_f1_widths[8],f14_f2_widths[8]],
398             'D',color='deepskyblue',label='Halloysite')
399 plt.plot([f14_f1_pos[12],f14_f2_pos[12],f14_f1_pos[18],f14_f2_pos[18]],
400             [f14_f1_widths[12],f14_f2_widths[12],f14_f1_widths[18],
401              f14_f2_widths[18]],
402             'D',color='blueviolet',label='Montmorillonite')
403 plt.plot([f14_f1_pos[38],f14_f2_pos[38]],
404             [f14_f1_widths[38],f14_f2_widths[38]],
405             'D',color='m',label='Gypsum')
406 plt.title('1.3,1.4,1.5 Micron Group')
407 plt.xlabel('Wavelength $\mu$m')
408 plt.xlim(1.25,1.65)
409 plt.ylim(0,0.2)
```

```
410 plt.ylabel('Feature Width $\mu$m')
411 ax.legend(loc='center left', bbox_to_anchor=(1, 0.5))
412 plt.show()
413
414 ####### Indexes from minerals in the python created df database
415 minlist13=np.array([1,2,4,6,8,97,98,99,101,103,105,107,194,195,197,199,200,
416                     201,203,205,206,208,210,217,218,219,222,223,226,228,230,
417                     233,235,237,258,260,263,287,290,291,313,501,503,505,507,
418                     510,512,516,517,518,519,520,521,522,524,525,527,529,531,
419                     532,546,548,550,553,558,559,561,563,669,731,732,734,742,
420                     749,751,753,754,756,793,796,798,799,825,843,844,859,860,
421                     868,904,905,907,909,911,912,966,968,976,980,981,982,983])
422
423 minlist14=np.array([33,35,37,40,46,47,49,51,58,67,239,241,215,258,260,263,265,
424                     308,310,312,
425          330,348,350,380,382,383,384,385,386,389,392,394,395,397,399,400,427,
426          429,444,501,503,505,507,510,512,516,517,518,519,520,521,522,524,525,
427          527,529,531,532,540,542,546,548,550,553,576,603,605,607,609,584,585,
428          633,635,614,615,617,619,621,622,623,625,626,628,630,632,637,638,639,
429          642,644,646,648,650,652,654,656,658,660,662,664,666,667,669,671,673,
430          675,687,688,690,692,694,731,732,734,740,741,742,832,846,848,849,892,
431          894,930,932,934,936,938,940,944,946,948,949,951,953,955,956,958,960,
432          962,964,980,981,982,983])
433
434 minlist15=np.array([138,281,283,348,350,480,482,484,486,489,492,493,495,496,
435                     671,673,675,769,771])
436
437 minlist2=np.array([33,35,37,40,46,47,49,51,58,67,239,241,215,258,260,263,265,
438                    308,310,312,
439          330,348,350,380,382,383,384,385,386,389,392,394,395,397,399,400,427,
440          429,444,501,503])
```

Appendix D

Tetracorder Snippets

D.1 Group 1.3 micron Introduction

```
\####### begin group 13 ###### 1.3-1.4 micron OH narrow  ############
\#
\#      smectite mineral group
\# Aliettite          Ca0.2Mg6((Si,Al)8O20)(OH)4    4H2O
\# Beidellite         (Na,Ca0.5)0.3Al2((Si,Al)4O10)(OH)2    nH2O
\# Ferrosaponite     Ca0.3(Fe2+,Mg,Fe3+)3((Si,Al)4O10)(OH)2    4H2O
\# Hectorite         Na0.3(Mg,Li)3(Si4O10)(F,OH)2
\# Montmorillonite  (Na,Ca)0.33(Al,Mg)2(Si4O10)(OH)2    nH2O
\# Nontronite        Na0.3Fe2((Si,Al)4O10)(OH)2    nH2O
\# Pimelite          Ni3Si4O10(OH)2 4H2O
\# Saliotite         (Li,Na)Al3(AlSi3O10)(OH)5
\# Saponite          Ca0.25(Mg,Fe)3((Si,Al)4O10)(OH)2    nH2O
\# Sauconite         Na0.3Zn3((Si,Al)4O10)(OH)2    4H2O
\# Stevensite        (Ca,Na)xMg3-x(Si4O10)(OH)2
\# Swinefordite      Li(Al,Li,Mg)4((Si,Al)4O10)2(OH,F)4    nH2O
\# Volkonskoite      Ca0.3(Cr,Mg,Fe)2((Si,Al)4O10)(OH)2    4H2O
\# Yakhontovite      (Ca,Na)0.5(Cu,Fe,Mg)2(Si4O10)(OH)2    3H2O
```

```
\# Zincsilite        Zn3(Si4O10)(OH)2    4H2O
\#
\# Contents (A) means added  (center and widths based on CRISM 2015
\# ksg = kaolinite-serpentine group
\#                                                    center (um)
   width (um)
\# A y3918  Phlogopite GDS20 fine fr s06crj3a=b        1.3792
         0.0206        Phyllosilicate  mica group
\# A y4338  Richterite NMNH150800 HCl s06crj3a=b       1.3833
         0.0264        Inosilicate     amphibole group
\# A y1146  Chrysotile HS323.1B s06crj3a=a             1.3876
         0.0217        Phyllosilicate  kaolinite-serpentine group
\# A y1518  Dickite NMNH46967 s06crj3a=a               1.3816 1.4150
    0.0172 0.0162 Phyllosilicate  kaolinite-serpentine group
\# A y1086  chlorite SMR-13.c 45-60um s06crj3a=a       1.388
          0.0183        Phyllosilicate  chlorite group
\# A y3462  Nacrite GDS88 s06crj3a=c           doublet 1.39   1.4148
       0.0515     Phyllosilicate  kaolinite-serpentine group
\# A y1632  Endellite GDS16 s06crj3a=b                 1.3898
         0.0536        Phyllosilicate  kaolinite-serpentine group
   doublet
\# A y5142  Tremolite HS18.3 s06crj3a=c                1.3915
         0.0165        Inosilicate     amphibole group
\# A y4452  Saponite SapCa-1.AcB s06crj3a=b            1.3915
         0.0534        Phyllosilicate  smectite
   assymetry < 0.9
```

```
\# A y2904  Lizardite NMNHR4687.c 70 s06crj3a=a        1.3925
          0.0267        Phyllosilicate  kaolinite-serpentine group
\# A y4548  Serpentine HS8.3B s06crj3a=c  1.395 um     1.393
           0.0289        Phyllosilicate  serpentine group
\# A y4800  Talc GDS23 74-250um fr s06crj3a=a          1.393
           0.0161        Phyllosilicate  Pyrophyllite-Talc Group
\# A y4182  Pyrophyllite PSY1A <850um s06mm09c=aaa     1.3943
          0.0154        Phyllosilicate  Pyrophyllite-Talc Group
\# A y 630  Antigorite NMNH96917.c 120um s06crj3a=b    1.395
           0.0313        Phyllosilicate  kaolinite-serpentine group
\# A y  36  Actinolite HS116.3B s06crj3a=b             1.396
           0.0166        Inosilicate     amphibole group
\# A y1176  Clinochlore GDS158 Flagst s06crj3a=b       1.3981
          0.0236        Phyllosilicate  chlorite gropup
\# A y5202  Uralite HS345.3B s06crj3a=b                1.396
           0.0164        Inosilicate     amphibole group
\# A y4596  Smaragdite HS290.3B Amphibol s06crj3a=b    1.398
           0.0292        Inosilicate     amphibole group
\# A y2706  Kaolinite KGa-1 (wxl) s06crj3a=b           1.3982
          0.042         Phyllosilicate  kaolinite-serpentine group
   doublet
\# A y1344  Cookeite CAr-1.b 60-104um s06crj3a=b       1.4001
          0.0325        Phyllosilicate  chlorite gropup
\# A y2820  Lepidolite HS167.3B s06crj3a=b             1.4005
          0.0294        Phyllosilicate  mica group
\# A y3816  Opal TM8896 (Hyalite) s06crj3a=a           1.4065
          0.0398        Tectosilicate   silica      SiO.nH2O
```

```
\# A y3876  Paragonite GDS109 s06crj3a=a                1.4076
          0.0310        Phyllosilicate  mica group
\# A y2832  Lepidolite NMNH105538 s06crj3a=b            1.4089
          0.0380        Phyllosilicate  mica group
\# A y5838  Kaol_Wxl+0.5Musc_Ruby AMX12 s06fs00a=a      1.4106
          9,934         Phyllosilicate
\### y2724  Kaolinite KGa-2 (pxl) s06crj3a=b            1.4127
          0.0379                        does not go short enough for
   curved continuum
\# A y2718  Kaolinite KGa-2 (pxl) s06crj3a=b            1.4127
          0.0379        Phyllosilicate  kaolinite-serpentine group
   doublet
\# A y5226  Vermiculite GDS13 Llano s06crj3a=a          1.390  1.432
    0.0178 0.1333 Phyllosilicate                  doublet
\# A y5226  Vermiculite GDS13 Llano s06crj3a=a          1.431
           0.0548        Phyllosilicate   doublet, see previous line
\#
```

D.2 Group 1.4 micron Introduction

```
\###################### begin group 14 ###### 1.4-micron region OH
   ################
\# Contents (A) means added  (center and widths based on CRISM 2015)
\#  * means also in group 13
\#                                                  center (um)
   width (um)
\#*A y3462  Nacrite GDS88 s06crj3a=c           doublet 1.39   1.4148
```

```
       0.0515     Phyllosilicate  Kaolinite-Serpentine group
   doublet
\#*A y2706  Kaolinite KGa-1 (wxl) s06crj3a=b           1.3982
          0.042         Phyllosilicate  Kaolinite-Serpentine group
   doublet
\#*A y1344  Cookeite CAr-1.b 60-104um s06crj3a=b       1.4001
          0.0325        Phyllosilicate  Chlorite group
\#   y4008  Portlandite GDS525 Ca(OH)2 s06crj3a=a      1.405  1.5136
    0.0154 0.0717
\# A y4926  Topaz Cameron_Cone_#42 s06crj3a=b          1.406
           0.0152        Nesosilicate
\#*A y3816  Opal TM8896 (Hyalite) s06crj3a=a           1.4065
          0.0398        Tectosilicate
\#*A y3876  Paragonite GDS109 s06crj3a=a               1.4076
          0.0310        Phyllosilicate  mica group
\#*A y2832  Lepidolite NMNH105538 s06crj3a=b           1.4089
          0.0380        Phyllosilicate  mica group‘
\#   y4872  Thuringite SMR-15.b 80um s06crj3a=a        1.408
           0.0210        Phyllosilicate
\# A y4464  Sauconite GDS135 s06crj3a=b                1.4093
          0.0582        Phyllosilicate  smectite
\# A y1134  Chrysocolla HS297.3B s06crj3a=b            1.4097
          0.0701        Phyllosilicate
\# A y2040  Halloysite NMNH106237 s06crj3a=a          1.4098
          0.0555        Phyllosilicate  Kaolinite-Serpentine group
   doublet
\# A y2976  Margarite GDS106 s06crj3a=c                1.410
```

```
          0.0202        Phyllosilicate  mica group
\# A y5838  Kaol_Wxl+0.5Musc_Ruby AMX12                1.4106
          9,934         Phyllosilicate
\# A y3348  Muscovite GDS113 Ruby s06mm09c=b           1.4101
          0.0289        Phyllosilicate  mica group
\# A y3270  Montmorillonite SWy-1 s06crj3a=b           1.4113
          0.0413        Phyllosilicate  smectite
\### y2724  Kaolinite KGa-2 (pxl) s06crj3a=b           1.4127
          0.0379                      does not go short enough for
   curved continuum
\#*A y2718  Kaolinite KGa-2 (pxl) s06crj3a=b           1.4127
          0.0379        Phyllosilicate  Kaolinite-Serpentine group
   doublet
\# A y2310  Hydrogrossular NMNH120555 s06crj3a=b       1.4134
          0.0628        Nesosilicate    (Garnet group)  merged
   doublet
\#   y 846  buddingtonite NHB2301 s06crj3a=b           1.414  1.563
    0.0286 0.057  Tectosilicate  Feldspar group
\# A y2064  Hectorite SHCa-1.Ac-B s06crj3a=b           1.4141
          0.0793        Phyllosilicate  smectite Montmorillonite
   group   triplet as one
\# A y4506  Sepiolite SepNev-1.AcB s06crj3a=a          1.4156
          0.1002        Phyllosilicate           broad complex
\# A y4380  Roscoelite EN124 s06crj3a=b                1.4158
          0.0381        Phyllosilicate  mica group
\# A y2448  Illite IL101 (2M2) s06crj3a=b              1.416
          0.0323        Phyllosilicate  mica group
```

```
\# A y3228  Montmorillonite SAz-1 s06crj3a=b          1.4163
          0.0803        Phyllosilicate  smectite
\# A y3864  Palygorskite CM46a Attapulg s06crj3a=b    1.4166
          0.0576        Phyllosilicate
\# A y3336  Muscovite GDS111 Guatemal s06crj3a=a      1.4176
          0.0300        Phyllosilicate  mica group
\# A y3282  Mordenite GDS18 s06crj3a=b                1.4178
          0.0655        Tectosilicate   Zeolite Group
\# A y4752  Stilbite HS482.3B Zeolite s06crj3a=b      1.419
           0.0905        Tectosilicate   Zeolite Group
\# A y1278  Clinoptilolite GDS152 Zeolit s06crj3a=b   1.4193
          0.0781        Tectosilicate   Zeolite Group
\# A y2214  Heulandite GDS3 s06crj3a=a                1.4217
          0.0863        Tectosilicate   Zeolite Group  broad doublet
\# A y3024  Meionite WS700.HLsp s06crj3a=b            1.4228
          0.0357        Tectosilicate   scapolite group
\# A y3570  Nontronite NG-1.b <2um fr s06crj3a=b      1.4237
          0.0559        Phyllosilicate  smectite  Montmorillonite
   group
\# A y3162  Mizzonite NMNH113775-1 Scap s06crj3a=b    1.4246
          0.0340        Tectosilicate   scapolite group
\#   y4914  Tincalconite GDS142 s06crj3a=a            1.427  1.47
     0.0918        borate           doublet
\# A y 306  Alunite HS295 s06crj3a=a                  1.428  1.477
    0.0171 0.0232 sulfate
\# A y2796  Lazurite HS418.3B s06crj3a=b              1.4289
          0.0937        Tectosilicate   Sodalite group
```

```
\# A y2784  Laumontite GDS5 Zeolite s06crj3a=b          1.431
          0.0908        Tectosilicate   Zeolite Group
\# A y1626  Elbaite NMNH94217-1.c <74 s06crj3a=b        1.4311 1.4752
    0.0230 0.0277 Cyclosilicate   Tourmaline group      like alunite
    doublet
\#   y5190  Ulexite HS441.3B s06crj3a=a                 1.433
          0.112         borate
\# A y5136  Tourmaline HS282.2B s06mm09c=ccc            1.435
          0.0402        Cyclosilicate   Tourmaline group
\# A y 228  Alunite AL706 Na_ s06crj3a=b               1.438  1.495
   0.0207 0.0244 sulfate
\#   y3978  Pinnoite NMNH123943 s06crj3a=a              1.4380
         0.0311        borate
\# A y 414  Analcime GDS1 Zeolite s06crj3a=a            1.424
          0.0432        Tectosilicate   Zeolite Group
\# A y1710  Eugsterite GDS140 Syn s06crj3a=b            1.4356
         0.0738        sulfate                        broader
\# A y4482  Scolecite GDS7 Zeolite s06crj3a=b          1.4403
         0.0810        Tectosilicate   Zeolite Group   doublet
\#   y4368  Rivadavite NMNH170164 Amph s06crj3a=a       1.4406
         0.0807        borate
\# A y1998  Gypsum SU2202 s06crj3a=a                    1.4470
         0.0525        sulfate             triplet, do this boudlet
    as one
\# A y4476  Schwertmannite BZ93-1 s06crj3a=b           1.4490
         0.1061        sulfate             broad
\# A y1374  Copiapite GDS21 s06crj3a=b                 1.4502
```

```
          0.0600        sulfate
\#*A y5226  Vermiculite GDS13 Llano s06crj3a=a          1.390  1.432
    0.0178 0.1333 Phyllosilicate   doublet
\#*A y5226  Vermiculite GDS13 Llano s06crj3a=a          1.431
           0.0548        Phyllosilicate   doublet, see previous line
\# A y3474  Natrolite HS169.3B Zeolite s06crj3a=b       1.4552
          0.0749        phyllosilicate  zeolite
\# A y1812  Gibbsite HS423.3B s06crj3a=b                1.4509 1.5496
    0.0773 0.0669  hydroxide              broader
\#
\#
\# future:
\#                                                    center (um)
   width (um)
\#   y5298  Zoisite HS347.3B s06crj3a=b
\#   y5310  Zunyite GDS-241B <150um s06crj3a=?          1.409
           0.0255 triplet 1
\#           "                    "                    1.479
           0.0213 triplet 2
\#           "                    "                    1.557
           0.0463 triplet 3
\##############################################
```

D.3 Group 1.5 micron Introduction

```
\###################### begin group 15 ###### 1.45-1.5 micron OH
   ##################
```

```
\# Contents (A) means added  (center and widths based on CRISM 2015)
\#  * means also in group 14
\#                                                    center (um)
   width (um)
\#*A y1812  Gibbsite HS423.3B s06crj3a=b                1.4509 1.5496
    0.0773 0.0669  hydroxide               broader
\#*A y3474  Natrolite HS169.3B Zeolite s06crj3a=b       1.4552
          0.0749          phyllosilicate  zeolite
\# A y 798  Bloedite GDS147 s06crj3a=a                  1.464
           0.094           sulfate
\# A y2568  Jarosite GDS99 K 200C Syn s06crj3a=a        1.469
           0.0199          sulfate                 narrower
\# A y2556  Jarosite GDS98 K 90C Syn s06crj3a=a         1.4711
          0.0753          sulfate                 broad
\# A y1470  Datolite HS442.3B s06crj3a=b                1.4713
          0.0311          Nesosilicate
\# A y2514  Jarosite GDS100 Na,Sy 90C s06crj3a=a        1.478
           0.0991          sulfate                 broad
\# A y2526  Jarosite GDS101 Na,Sy 200C s06crj3a=a       1.4787
          0.0247          sulfate                 narrower
\# A y4026  Prehnite GDS613.a <60um s06crj3a=aa_        1.4798
          0.0255          Phyllosilicate
\#
\# future:
\#                                                    center (um)
   width (um)
\# A y1626  Elbaite NMNH94217-1.c <74 s06crj3a=b        1.4311 1.4752
```

```
    0.0230 0.0277 Cyclosilicate   Tourmaline group      like alunite
    doublet
\#   y5310  Zunyite GDS-241B <150um s06crj3a=?         1.409
           0.0255 triplet 1
\#           "␣␣␣␣␣␣␣␣␣␣␣␣␣␣␣␣␣"                     1.479
           0.0213 triplet 2
\#           "␣␣␣␣␣␣␣␣␣␣␣␣␣␣␣␣␣"                     1.557
           0.0463 triplet 3
```

Minerals identified in Rover VNIR Instrument at D26

```
 \##########################################
group 1
use= yes           \# yes or no,     if no,    skip this entry.
udata: reflectance
convolve: no
preratio: none
preprocess: none
algorithm: tricorder-primary
ID=nanohematite.BR34b2

define library records
  a SMALL:  [splib06]  3468 d          \# file ID, rec no.    1 to
     2171 channels
  a MEDIUM: [splib06]  xxxx d          \# file ID, rec no. 2172 to
     4852 channels
  a LARGE:  [splib06]  xxxx d          \# file ID, rec no.
     larger_chans_future
```

```
endlibraryrecords
\#=-=-=-=-=-=-=-=-=-=-=-=- TITLE=Nanohematite BR93-34B2       W1R1BbS
[DELETPTS]
Fe3+ nanohematite  BR34B2    \# output title

define features
   f1a DLw 0.4400  0.4550  0.6117  0.6315 ct [CTHRESH4] rct/lct> 0.9
       1.1
   f2a OLw 0.7650  0.7950  1.1770  1.2070 ct [CTHRESH4] rct/lct> 0.4
       0.6
\# Notes:
\#       Feat:  1  has a weight of
\#       Feat:  2  has a weight of
\#       rct/lct> 0.5 added 10/20/00 BWR
endfeatures

define constraints
   constraint: FD-FIT>[GLBLFDFIT] DEPTH-FIT>[GLBLDPFIT]
   constraint: FITALL>[GLBLFITALL]
endconstraint

define output
   output=fit depth fd
   fe3+\_hematite.nano.BR34b2         \# Output base file name  was
      nanohematite.BR34b2
   8 DN 255 = 0.5000
   compress= zip
```

```
endoutput


define actions
   action: sound1
   action: none
endaction
\############################
\############################
group 2
use= yes           \# yes or no,     if no,    skip this entry.
udata: reflectance
convolve: no
preratio: none
preprocess: none
algorithm: tricorder-primary
ID=calcite+0.5Ca-mont


define library records
   a SMALL:  [splib06]  5526 d         \# file ID, rec no.    1 to
      2171 channels
   a MEDIUM: [splib06]  xxxx d         \# file ID, rec no. 2172 to
      4852 channels
   a LARGE:  [splib06]  xxxx d         \# file ID, rec no.
      larger_chans_future
endlibraryrecords
\#=-=-=-=-=-=-=-=-=-=-=- TITLE=Calcite+.50Ca-Mont AMX6      W1R1Bb
[DELETPTS]
```

```
calcite + 50% Ca-mont areal      \# output title

define features
   f1a DLw 2.245   2.275   2.376   2.406  ct [CTHRESH4] r*bd> [RBD23
      ]
   f2a DLw 2.165   2.195   2.248   2.278  ct [CTHRESH4] r*bd> [RBD22
      ]
\# Notes:
endfeatures

define constraints
   constraint: FD-FIT>[GLBLFDFIT] DEPTH-FIT>[GLBLDPFITg2]
   constraint: FITALL>[GLBLFITALL]
endconstraint

define output
   output=fit depth fd
   calcite+0.5Ca-mont          \# Output base file name
   8 DN 255 = 0.5000
   compress= zip
endoutput

define actions
   action: sound1
   action: none
endaction
\##########################
```

Minerals Identified in Contact ASD Spectra

```
    \########################
group 1
use= yes           \# yes or no,     if no,    skip this entry.
udata: reflectance
convolve: no
preratio: none
preprocess: none
algorithm: tricorder-primary
ID=siderite1

define library records
  a SMALL:  [splib06]  4560 d          \# file ID, rec no.    1 to
     2171 channels
  a MEDIUM: [splib06]  xxxx d          \# file ID, rec no. 2172 to
     4852 channels
  a LARGE:  [splib06]  xxxx d          \# file ID, rec no.
     larger_chans_future
endlibraryrecords
\#=-=-=-=-=-=-=-=-=-=-=- TITLE=Siderite HS271.3B            W1R1Ba
[DELETPTS]
Fe2+ generic, ref= siderite HS271.3B                \# output title

define features
   f1a DLw 2.1980  2.2280  2.3860  2.4160 ct [CTHRESH4]
   f2a WLw 0.756   0.785   1.675   1.705  ct [CTHRESH4]
```

```
\# Notes:
\#        Feat:  1  has a weight of 0.042
\#        Feat:  2  has a weight of 0.958
\#   added 1/7/2000
\# May 7, 2012: a 2.3-um feature with Fe2+
\# dominates as siderite.  For example, on Mars, pyroxene+olivine
\# make the Fe2+, then any 2.3 feature dominates the results
\# due to the strong response of the Fe2+.
\# solution: make the Fe2+ band a weak band  - RNC
\# Weak bands must be present, but area is set to zero.
endfeatures

define constraints
   constraint: FD-FIT>[GLBLFDFIT] DEPTH-FIT>[GLBLDPFITg2]
   constraint: FITALL>[GLBLFITALL]
endconstraint

define output
   output=fit depth fd
   fe2+generic_carbonate_siderite1                    \# Output base
      file name  was siderite1
   8 DN 255 = 0.5000
   compress= zip
endoutput

define actions
   action: sound1
```

```
   action: none
endaction
\##########################
```